공학박사 학위논문

Studies on Synthesis and Optoelectronic Properties of Supramolecules Consisting of Amphiphilic Cyano-Stilbene Derivatives

양친매성 사이아노 스틸벤 기반 초분자체의 합성과 광전자 특성에 관한 연구

2021 년 2 월

서울대학교 대학원

재료공학부

이 현 준

Studies on Synthesis and Optoelectronic Properties of Supramolecules Consisting of Amphiphilic Cyano-Stilbene Derivatives

A THESIS SUBMITTED IN PARTIAL FULFILLMENT OF
THE REQUIREMENTS FOR THE DEGREE OF
DOCTOR OF PHILOSOPHY
IN ENGINEERING AT THE GRADUATE SCHOOL OF
SEOUL NATIONAL UNIVERSITY

FEBRUARY 2021

By
Hyun-Jun Lee

Supervisor
Prof. Soo Young Park

Studies on Synthesis and Optoelectronic Properties of Supramolecules Consisting of Amphiphilic Cyano-Stilbene Derivatives

양친매성 사이아노 스틸벤 기반
초분자체의 합성과 광전자특성에 관한 연구

지도 교수 박 수 영

이 논문을 공학박사 학위논문으로 제출함

2020 년 12 월

서울대학교 대학원

재료공학부

이 현 준

이현준의 공학박사 학위논문을 인준함

2020 년 12 월

위 원 장 남 기 태 (인)

부위원장 박 수 영 (인)

위 원 장 호 원 (인)

위 원 황 동 렬 (인)

위 원 권 지 언 (인)

Abstract

Studies on Synthesis and Optoelectronic Properties of Supramolecules Consisting of Amphiphilic Cyano-Stilbene Derivatives

Hyun-Jun Lee

Department of Materials Science and Engineering

The Graduate School

Seoul National University

Water is the origin of life and the most abundant resource on Earth's surface. Making functional materials which is operative in water has an important meaning as it can be applied to the fields of bio science and energy. Many organisms in nature already have functional materials in their organelles that perform complex life activities in water. Plants produce oxygen and starch through photosynthesis. Proteins of animals form organelles through self-assembly in the collection fluid, and carry out mass transport entry and transmission of electrical signals. A lot of research has been conducted to make a material as efficient as living organells by mimicking this principle of operation. Among them, organic materials are particularly noteworthy because they can impart various properties through molecular design and are easy to apply in vivo. Among the various categories of organic materials, supramolecule can easily form a structure in water through self-assembly of building blocks. Its characteristics are also easily tuned

by the design of the unit molecule. Recently, supramolecules with size of nanometer scale are being actively applied in life science fields or catalyst fields. Previously, research on water-soluble supramolecules was biased toward making a regular structure. However, in recent years, in addition to this, many new supramolecules having interesting optoelectronic properties have been reported. Using the excitation state of these supramolecules, attempts to apply them to various fields such as chemical reactions, catalysts, bio-imaging, and biosensors have been reported. In this thesis, the structure and physical properties of supramolecular systems formed from conjugated organic molecules were analyzed and applied as a water-soluble two-dimensional fluorephores and hydrogen evolution photocatalysts. Conjugated organic molecules having a pyridinium cation end group as building blocks for making a water-soluble supramolecules were designed and synthesized.

In Chapter 2, a two-dimensional supramolecular body having a high fluorescence efficiency of 60% and regular pores in a honeycomb shape was synthesized. The newly designed and synthesized host-guest complex of molecule 1 and cucurbit[8]uril is a two-dimensional structure that is thermally stable, has a size of over 500 nm and a thickness of 1.7 nm, but exhibits high fluorescence efficiency.

Molecule 1 also forms supramolecules with size of about 10 nm in aqueous solution through a hydrophobic/hydrophilic balance. This supramolecule has a short excited state lifetime of about 1 ns. In Chapter 3, a highly efficient hydrogen reduction photocatalytic system was implemented using molecule 1. In order to overcome the

short excited lifetime of about 1 ns, iodide was added to enhance intersystem crossing via heavy atom effect. As a result, the photocatalytic performance was enhanced over 500 times by utilizing a triplet excited state with a relatively long excited state. In addition, in order to compensate for the insufficient visible light absorption of Molecule 1, a commercial dye was added. Molecule 1 has cationic character, so it can interact with an anion commercial dye effectively. Iodide was also added to the ionic complex to utilize triplet excited state, and this supramolecular system finally showed hydrogen production performance comparable to the state of the art performance reported in metal oxide semiconductors.

In Chapter 4, the effect of external halogen ion addition was further studied. In addition, molecule 2 with good visible light absorption was designed and synthesized. In the case of molecule 2, the singlet excited state lifetime was rather reduced to about 0.1 ns, but the performance was greatly improved by the addition of halogen ions. In this system, the performance change due to the addition of halogen was carefully studied, and it was confirmed that the performance was also increased by the addition of chloride. From this, we implemented a supramolecular system that stably performs hydrogen reduction photocatalytic reaction more than 15,000 times for 4 days under simulated sunlight irradiation without additional halogen ions in seawater.

Keyword: fluorescence, two dimensional supramolecule, hydrogen evolution, photocatalyst, triplet excited state, heavy atom effect, supramolecule.

Student Number: 2015-30189

Contents

List of Tables

List of Schemes

List of Figures

Chapter 1. Introduction

1.1. Excited state of molecules

Molecular excitation and deactivation are closely related to important driving mechanisms of organic photovoltaics (OPVs), organic light-emitting diodes (OLEDs), and artificial photosynthesis.[1-2] The excitation path of a molecule in the ground state and decay path of an excited molecule is well described in a Jablonski diagram (Scheme 1-1). Under certain conditions that satisfy the Franck-Condon principle, the absorption of light by molecules occurs very quickly. ($\sim 10^{-15}$ S)[3-4] Excitation of a molecule is an electronic transition derived from absorption of a photon with energy corresponding to the energy difference between two different electronic states. Deactivation of an excited state follows either radiative decay or non-radiative decay path. Some excited molecules release thermal energy along with a non-radiative decay path. Vibrational relaxation and internal conversion are non-radiative decay paths. Other excited molecules emit photons along with radiative decay path. In general, the transition between the two states occurs only when the spin states are the same according to the selection rule. A spin state of a ground state is singlet, it is thus conserved during excitation. A resultant singlet excited state also emits a photon through the spin allowed transition. In this case, this transition is specifically referred to as fluorescence. Spin-forbidden transition is relatively slower than spin allowed

transition.[3] Non-radiative decay from an excited singlet to an excited triplet state is denoted as intersystem crossing (ISC), whereas radiative decay from an excited triplet state to a ground state is denoted as phosphorescence. In nature, phosphorescence is less commonly observed than fluorescence, but heavy atoms promote ISC by spin-orbit coupling. The relationship between radiative decay and non-radiative decay can be calculated with the following equations.

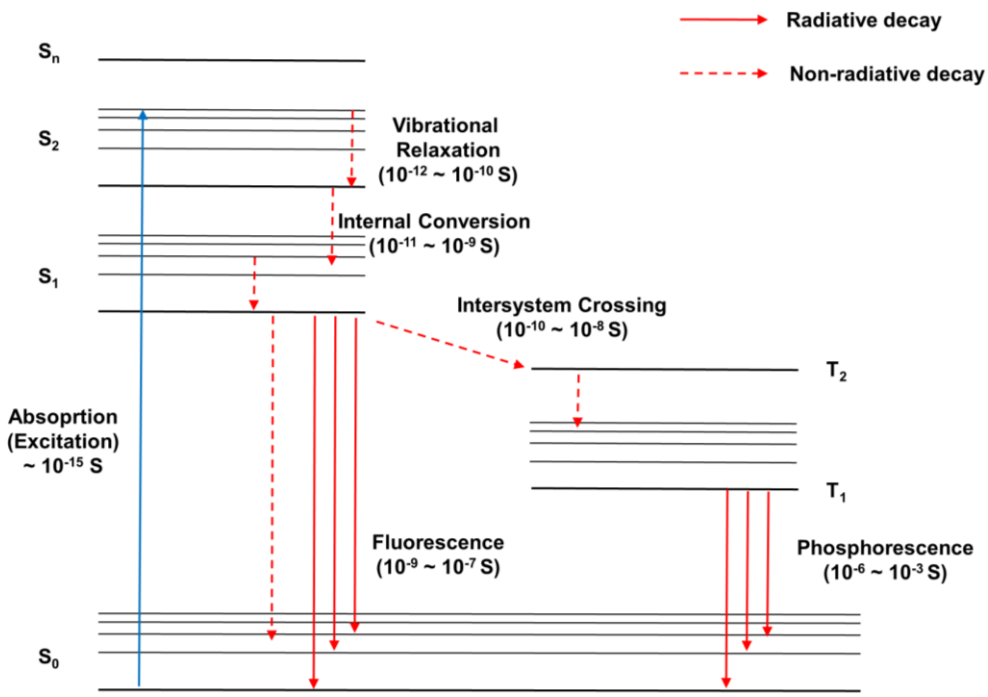

Scheme 1-1. Jablonski diagram of excited state of a molecule. S_n denotes singlet excited state, whereas T_n denotes triplet excited state.

$$\Phi_F = \frac{number\ of\ emitted\ photons}{number\ of\ absorbed\ photons} = \frac{k_r^S}{k_r^S + k_{nr}^S} \quad (1\text{-}1)$$

Quantum yield of fluorescence (Φ_F) is defined as the number of emitted photons over the number of absorbed photons. It is also represented by the rate constant of radiative decay (k_r^S) and non-radiative decay (k_{nr}^S).

$$\tau_S = \frac{1}{k_r^S + k_{nr}^S} \quad (1\text{-}2)$$

Thus, the lifetime of singlet excited state (τ_S) is also expressed in terms of k_r^S and k_{nr}^S.

$$k_r^S = \frac{\Phi_F}{\tau_S} \quad (1\text{-}3)$$

$$k_{nr}^S = \frac{(1 - \Phi_F)}{\tau_S} \quad (1\text{-}4)$$

Φ_F and τ_S can be obtained via experimental data. k_r^S and k_{nr}^S are calculated from equations 1-3 and 1-4.

In the case of systems where the ISC is not negligible, such as phosphorescent phosphors, the triplet excited state must also be considered. Quantum yield of ISC

(Φ_{ISC}) and phosphorescence (Φ_P) are expressed as follows.

$$\Phi_{ISC} = \frac{k_{ISC}}{k_r^S + k_{nr}^S} = k_{ISC}\tau_S \quad (1\text{-}5)$$

$$\Phi_P = \frac{k_r^T}{k_r^T + k_{nr}^T}\Phi_{ISC} \quad (1\text{-}6)$$

Where, k_{ISC}, k_r^T, and k_{nr}^T denotes the rate constant of ISC, radiative decay of triplet excited state and non-radiative decay, respectively.

As such, after being excited, the molecule returns to the ground state through various processes. However, electrons and holes generated after being excited interact with each other. As a result, an electron-hole pair so-called exciton is formed. Exciton's binding energy is expressed as follows.

$$E_b^{ex} = -\frac{\mu_{e,h}^*}{m_e\ \varepsilon^2} Ry(H)$$

Where, μ, m_e, ε, and Ry(H) denote reduced mass, electron mass, dielectric constant of the medium, binding energy of electron in hydrogen atom, respectively.

As in the above equation, the binding energy of exciton is inversely proportional to the dielectric constant of the substance. Therefore, organic semiconductor materials with

relatively small dielectric constants have greater exciton binding energy than inorganic semiconductor materials. The exciton binding energy of organic semiconductors is 0.1~0.3 eV, which is greater than the thermal energy (kT), so it is very stable. This is also an important issue in organic photovoltaic.

When we use opto-electrical materials for specific applications, most of them utilize these excited states. We design a molecule with an excited deactivation path that fits the purpose, and change the surrounding chemical environment to pursue excited state engineering.

1.2. Self-assembled amphiphilic molecules in water

Supramolecules can be described as "chemistry beyond the molecule",[5] implying assembled molecules by a secondary bonding. Secondary bonds are generally made by Van der Waals, pi-donor-acceptor, hydrogen bonding, hydrophobic/hydrophilic interaction, ion-pairing, and coordinated bond. Since these intermolecular forces are relatively weaker than covalent bonding and reversible,[6-7] they are easily controlled by external stimuli. Indeed, many natural substances, including organisms in our body, consisting of supramolecules. Mimicking natural species, many efforts have been made to manipulate and adjust practical supramolecular systems.[8-9] Various types of supramolecules are applied as membranes,[10] fluorophores,[11-12] energy transfer

materials[13-14], and electron-transfer materials.[15-19] Among them, supramolecules that can be implemented in water, especially, are attracting high attention because of their bio-applicability.[20-21]

Table 1-1. Strength of different types of intra- or intermolecular forces.[2-3]

Type of bonding	Bonding strength (kJ/mol)
Van der Waals	1-5
Pi-donor-acceptor	7-20
Hydrogen bonding	10-20
Hydrophobic/hydrophilic interaction	12-15
Ion-pairing	12-20
Coordinate bond	40-120
Covalent bond	150-1000

Amphiphilic organic molecules are good building blocks for supramolecular systems that are operative in an aqueous solution.[22-24] Amphiphilic molecules usually have hydrophobic cores and hydrophilic tails. They assemble into supramolecules by a balance between hydrophobic/hydrophilic interaction or ionic interaction in water.[24]

Recently, amphiphilic molecules are being studied as building blocks not only to make structures but also to make various functional supramolecules in water.[11-13, 15-16, 18-19]

1.2.1. Host (cucurbituril8) – guest (amphiphilic organic molecules) complex

Host-guest chemistry is being actively explored as a method of preparing a supramolecule. Host and Guest can be regarded as a lock and a key. A host usually recognizes and encloses guest materials while they mixed. The force for organizing host-guest complexes is non-covalent bonding such as hydrogen bonding, ionic interaction, and hydrophobic/-philic interaction. Since the complex becomes more thermodynamically stable upon binding, the forward reaction is favored after mixing. However, since it is a reversible reaction due to the nature of secondary bonding, it is easy to adjust the structure or properties according to external stimuli. Therefore, host-guest chemistry is being applied in various fields.[25-27] Various host materials have been introduced, and among them, macrocycle materials are speculated as hosts that can compose supramolecules in aqueous solutions.[26] Crown ether, cyclodextrin, calixarene, cucurbituril, and pillararene have been reported as effective macrocyclic hosts.[25-27]

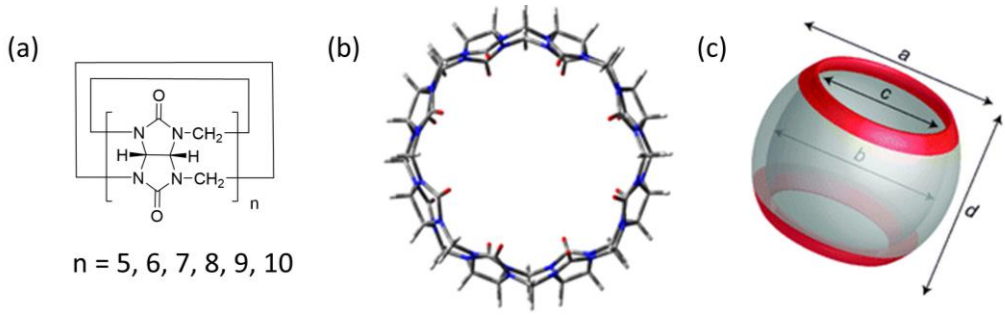

Figure 1-1. (a) Chemical structure of Cucurbit[n]urils (b) X-ray structure of Cucurbit[n]urils. (blue: nitrogen, red: oxygen, grey: carbon, white: hydrogen) (c) schematic view of Cucurbit[n]urils[28-29]

Table 1-2. Parameters of Cucurbit[n]urils.[28-29]

Species	Outer diameter (a)	Inner cavity (b)	Inner cavity (c)	Height (d)
CB5	13.1 Å	4.4 Å	2.4 Å	9.1 Å
CB6	14.4 Å	5.8 Å	3.9 Å	9.1 Å
CB7	16 Å	7.3 Å	5.4 Å	9.1 Å
CB8	17.5 Å	8.8 Å	6.9 Å	9.1 Å
CB9	19.0 Å	10.3 Å	8.6 Å	9.1 Å
CB10	20.0 Å	11.7 Å	10.0 Å	9.1 Å

In particular, cucurbiturils are macrocycle hosts that have attracted much attention recently. Cucubiturils are consisting of repeating glycoluril unit. The cavity of

cucurbituril is hydrophobic, consequently, it is compatible with hydrophobic guests.[30] Cucubiturils also have a carbonyl group draw cation through ion-dipole interaction.[31] Therefore, they specifically recognize and bind with cations in water. In particular, it is known as binding energy between cucurbiturils and amphiphilic cation guests is strong.[32] In addition, they are soluble in water and have low toxicity, so they are frequently applied as biomaterials.[33-35] As illustrated in fig 1-1, cavity size is varied with the number of glycoluril repeating units. Cucurbit[5]uril and cucurbit[6]uril have cavity sizes which are adequate for gas molecule adsorption.[36] On the other hand, cucurbit[7]uril has a cavity size suitable for one aromatic ring moiety and cucurbit[8]uril two aromatic rings.[36-37] In particular, cucurbit[7]uril and cucurbit[8]uril are used as fluorescent sensors, drug delivery materials, and bio-sensors combining with functional aromatic guests.[38-41]

1.2.2. Two dimensional supramolecular system

Two-dimensional (2D) biomaterials with regular pores have a large surface area and special functionality such as molecular recognition.[42-43] A membrane within a cell is a representative two-dimensional supramolecular system in nature.[44] The membrane composed of amphiphilic phospholipids is flexible and can form a three-dimensional structure along the cell wall if necessary. These 2D biomaterials play a sophisticated

role in maintaining life by selectively controlling mass transport in vivo.[44] Efforts to artificially synthesize two-dimensional supramolecular materials by bio-mimics continued.[45] Artificial membranes that control the transfer of molecules with a large surface area have been reported.[46-48] In addition, a system capable of reversible implementation of two-dimensional and three-dimensional structures by external stimuli has also been reported.[49-50] In terms of materials, it is particularly noteworthy that the study implemented a two-dimensional supramolecular using lateral amphiphilic molecules and cucurbit[8]uril.[51-52] This is because the cucurbit[8]uril based 2D supramolecular system is operative in an aqueous medium. Recently, cucurbit[8]uril based two-dimensional materials with fluorescence have also been reported, showing the possibility of being applied to bio-sensor and bio-imaging.[53-54] However, it remains a task to implement a two-dimensional supramolecular system that is structurally stable and highly fluorescent.

1.3. Photocatalytic hydrogen evolution

Artificial photosynthesis is a technology that can make a useful product using sunlight, an infinite energy source.[55-56] Realizing artificial leaf by mimic natural photosynthesis must control a series of complicated processes starting from light irradiation. Advanced strategies related to light absorption, charge separation, charge transfer, catalytic site,

etc. are required to develop high-performance artificial leaves. Depending on what kind of product or process you focus on, artificial photosynthesis is also related to technologies such as photo-reforming[57] and photo-redox catalysis.[58] Of these, photocatalytic hydrogen evolution has been studied for over 40 years as a means to create clean energy, hydrogen gas.[59] Since it was discovered that semiconducting materials such as metal oxides can reduce proton by Uv light in water, related materials have made great progress.[60-63] Recently, materials with a photon to hydrogen conversion yield of 100% have been reported.[64] The principle of the photocatalytic hydrogen evolution system can be largely divided into two. The first is a direct water-splitting method that breaks water into hydrogen and oxygen gas.[59, 65-66] This method is considered an ideal hydrogen production method, but it has to overcome some tasks. A kinetical and thermodynamical balance between hydrogen production, which is a two-electron reduction reaction, and oxygen production, which is four-electron oxidation, must be achieved, and an efficient water oxidation catalyst must be developed.[65, 67] The second method is half-reaction using sacrificial electron donors.[60] This method requires an additional sacrificial reagent and has a disadvantage in that the rate of hydrogen production varies depending on the concentration of the sacrificial reagent.[68] However, a sacrificial reagent can photo-reform biomaterials into useful new materials, and only high-purity hydrogen gas is made without oxygen.[57, 69-70] Moreover, a large number of hydrogen reduction catalysts that have excellent performance have already been reported.[71] Because of these advantages, studies on the half-reaction are also being

actively conducted.

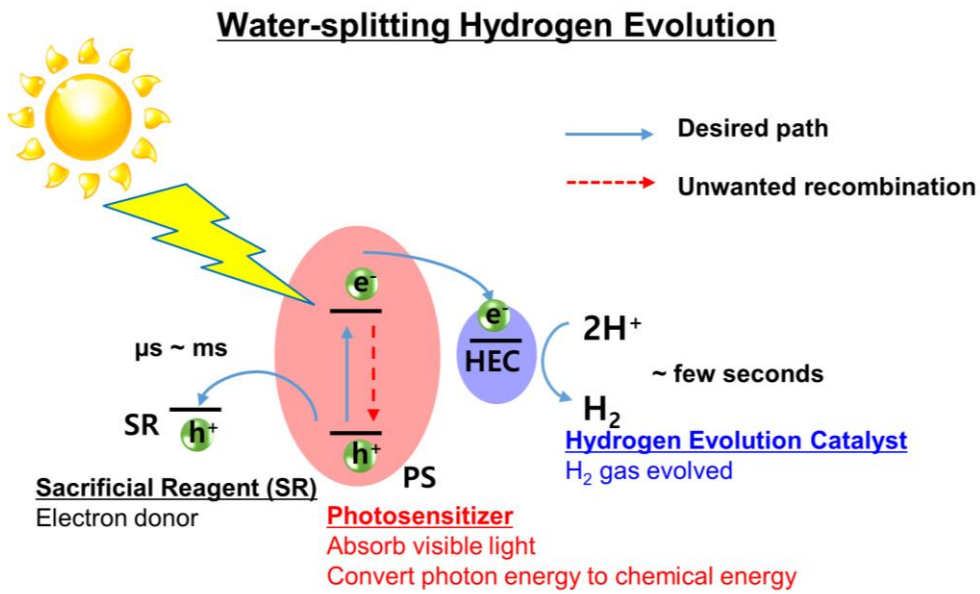

Scheme 1-2. Schematic view of half reaction of photocatalytic hydrogen evolution

As illustrated in scheme 1-2, a half-reaction of photocatalytic hydrogen evolution is triggered by light absorption by a photosensitizer. After light absorption, an exciton should be separated into an electron and a hole. Subsequently, the hole is reduced by a sacrificial electron donor, and the electron moves towards a catalytic site and reduces a proton.[72] For the sake of efficient hydrogen reduction, unwanted pathways should be restricted. Generally, the electron transfer rate between sacrificial reagent and photosensitizer is in the order of microseconds to milliseconds.[72] Therefore, it is

important to maintain a stable excited or charge-separated state for this time. In the case of an organic material-based system, it is particularly important to suppress recombination due to the high binding energy of exciton.[73]

1.3.1. Carbon based systems for hydrogen evolution

Compared to inorganic materials, organic conjugated molecules have the advantage of being able to easily control the absorption wavelength, absorbance, solubility, and energy level through appropriate molecular design and synthetic chemistry. Therefore, research has been actively conducted to apply an organic photocatalyst to photocatalytic hydrogen production. One of the most reported material to date is graphitic carbon nitride (g-CN). Bulk g-CN is able to absorb visible light and generally exhibit a hydrogen evolution rate (HER) of about 100 μmol/g·h.[74] However, g-CN has some disadvantages. First, it needs a calcination process at high temperatures. Second, it has limited visible light absorption. To be more specific, when the light source is limited light with a wavelength longer than 450 nm from a Xenon lamp, HER decreases to one-eighth, and no hydrogen production is made by using light with a longer wavelength than 600 nm. Therefore, researchers are trying to increase g-CN's intrinsic performance by modifying its synthetic process recently. For instance, Wang's group increased the HER of g-CN by more than 5 times by dividing the bulk g-CN into

nano-layers to widen the specific surface area, but the manufacturing process becomes more difficult due to the high-temperature oxidation process.[75]

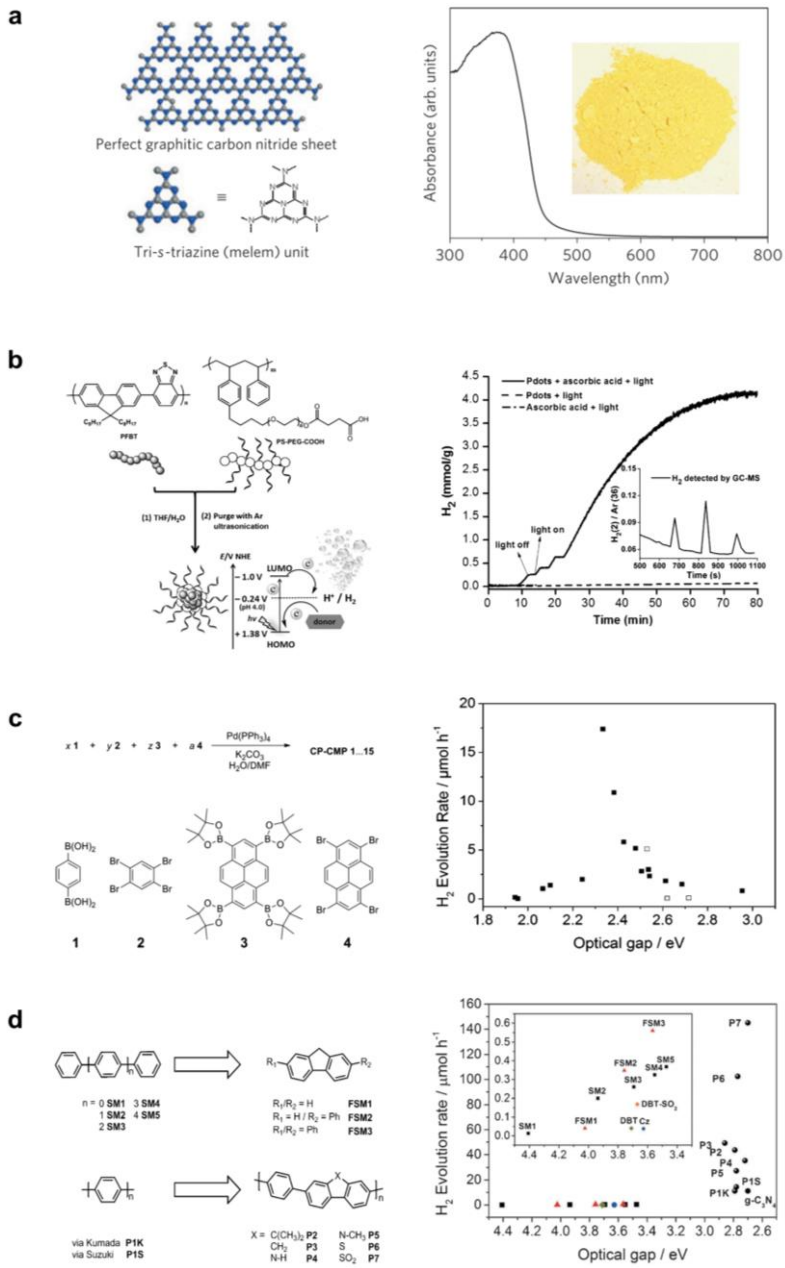

Figure 1-2. (a) chemical structure and Uv-vis absorption spectrum of g-CN.[76] (b) schematic view and hydrogen evolution graph of polymer dot photocatalytic system.[77]

(c) synthetic route and optical band gap versus hydrogen evolution rate of cross-linked polymeric photocatalytic system.[78] (d) synthetic route and optical band gap versus hydrogen evolution rate of linear polymeric photocatalytic system.[79]

On the other hand, π-conjugated polymer materials are also frequently reported as hydrogen evolution photocatalysts.[77, 80-85] As mentioned above, in the case of organic materials, there is a disadvantage in that exciton binding energy is strong, but many efforts have been made to overcome this.[73] As in the case of OPV, an attempt to make a donor-acceptor polymer pair in water is a representative example.[86] Remarkably, some polymer-based materials showing a high HER of several mmol/g·h or more have been reported. However, most of these studies remain in the early stages. Although many polymeric materials have been introduced, a deep study of the structure-property relationship has not been conducted. For instance, Cooper's group synthesized various types of conjugated polymers to analyze the properties of photocatalysts for hydrogen production, but the relationship between their absorption area, absorbance, energy level, and hydrogen production performance was not clearly established.[78-79] Furthermore, there are suspicions that metal catalyst residues used in polymer synthesis affect hydrogen production.[87-88]

Intrinsically, g-CN or polymer materials have common disadvantages that 1) synthesis is difficult, 2) it is difficult to control physical properties, 3) reproducibility is relatively low due to their synthetic route, and 4) compatibility to water is relatively low. As a

result, the experimental conditions are usually limited. For example, the H. Tian group of Uppsala University in Sweden achieved 8 mmol/g.h of HER, the highest performance among organic photocatalysts, using commercial PFBT polymers containing fluorene and benzothiadiazole. However, the dispersion stability of the polymer in an aqueous solution is very low, so it is essential to use a large amount of dispersant, and it can only be operated at a low concentration of 16.8 μg/mL, so the total hydrogen production was only 67.2 nmol/mL.[85, 89]

1.3.2. Supramolecular photocatalytic systems for hydrogen evolution

Materials such as polymer dots prepared by a top-down method have limitations as incompatibility to water.[90] However, supramolecules manufactured with a bottom-up approach can acquire a sufficient solubility in water according to the building block design.[90-91] In particular, amphiphilic aromatic molecules are good building blocks capable of forming supramolecules in an aqueous solution. Besides, the optoelectrical characteristics of the materials can be easily controlled through molecular design. Because of these advantages, supramolecular photocatalytic hydrogen evolution systems are also being actively explored.[19, 90-93] However, self-assembled molecules also have high exciton binding energy, a fatal drawback of organic materials as

photocatalytic system. Because of this, unwanted recombination occurs and it is difficult to increase photocatalytic performance. To overcome high exciton binding energy, many researchers in this field have tried to implement delocalized exciton in supramolecular photocatalytic systems. The solubility was precisely controlled through molecular design or the external chemical environment was changed to induce pi-conjugated building blocks to assemble close to perfect H-bonding in an aqueous solution.[19, 94-95] However, the performance has not yet reached the practical level, so a new strategy is needed to solve the high exciton binding energy.

1.3.3. Supramolecular photocatalytic systems for hydrogen evolution

1.4. Outline of thesis

In this thesis, supramolecular systems with various functions in an aqueous solution are reported. To implement a supramolecular system capable of operating in an aqueous solution, the molecular design followed strategies as shown in Figure 1-3. The pyridinium end group provides solubility in water and cationic characteristic on the supramolecule and acts as a strong electron accepting group. The aromatic core has hydrophobicity and acts as an electron donor.

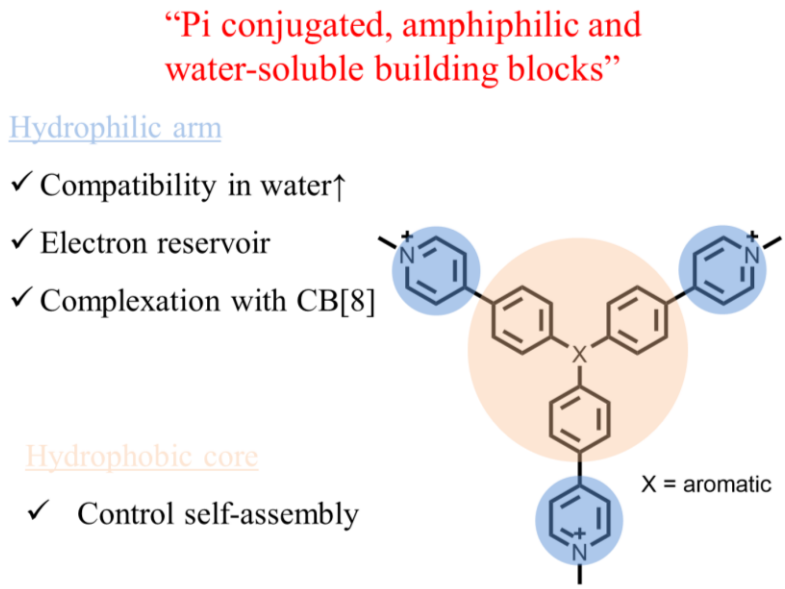

Figure 1-3. Strategies of molecule design in this thesis.

Water-soluble two dimensional (2D) materials showing high fluorescence efficiency are attracting attention because they can be used as bio-imaging and sensors. In chapter 2, a remarkably fluorescent (Φ_F = 0.60) and completely water-soluble ~ 1 μm sized 2D supramolecular organic framework (2D SOF) is reported. This exceptionally high fluorescence quantum yield in this system is ascribed to restriction of non-radiative decay path. I designed and synthesized trilateral molecule 1 with pyridinium arm. Binding energy between cucurbit[8]uril and pyridinium in water is quiet high so that they can make stable SOF. The vibration of molecule 1, the guest material, is

significantly reduced by forming a host-guest structure. Not only such molecular design novelty, this chapter significantly includes the first full elucidation of photophysical behavior of fluorescent 2D SOF which so far has been elusive in the literature.

Another important issue on water-compatible optoelectronic materials is photocatalytic hydrogen evolution. In chapter 3, highly efficient (HER rate = 400 mmol/g·h, TOF = 687 h^{-1}) and stable (TON = 27,000 for 84 hours) self-assembled molecules (SMs) with pt co-catalyst for photocatalytic hydrogen evolution is reported. To implement exceptionally high hydrogen evolution performance under visible light irradiation in pure water, I adapted molecular design concepts such as the amphiphilic molecule, ionic complex, and nano-aggregation. Molecule 1 self-assembled in water into 10 nm sized nanoparticles. The supramolecule has not enough visible light absorption and excited-state lifetime to be applied as a photocatalytic system. I elaborated its performance by adding commercial red dye and external heavy atoms. As a result, I successfully demonstrated SM exhibiting comparable performance with state-of-the-art metal oxide semiconductor-based photocatalyst by manipulating its triplet excited state. Through more advanced molecular design and excited state engineering, I have made a material that can be operative in more environmentally-friendly circumstances. In chapter 4, another supramolecular photocatalytic hydrogen evolution system is reported. Molecule 2 was developed for better visible light absorption. Although molecule 2 has a shorter singlet excited state lifetime than molecule 1, triplet excited

state could be utilized by adding heavy atoms. This result suggests that seawater with high chloride contents can be used in my system. As a result, the supramolecule consisting of molecule 2 exhibited stable and efficient hydrogen evolution performance (TON ~ 15,000 for 4 days) under 1 sun condition and in seawater.

1.5. References

[1] Cardinale, G., *Optoelectronics: introductory theory and experiments*. Cengage Learning: 2003.

[2] Hu, W.; Bai, F.; Gong, X.; Zhan, X.; Fu, H.; Bjornholm, T., *Organic optoelectronics*. John Wiley & Sons: 2012.

[3] Turro, N. J., *Modern molecular photochemistry*. University science books: 1991.

[4] Braslavsky, S. E., Glossary of terms used in photochemistry, (IUPAC Recommendations 2006). *Pure Appl. Chem.* **2007,** *79*, 293-465.

[5] Lehn, J.-M., *Angew. Chem. Int. Ed.* **1988,** *27*, 89-112.

[6] Friese, V. A.; Kurth, D. G., *Curr. Opin. Colloid Interface Sci.* **2009,** *14*, 81-93.

[7] Whitesides, G. M.; Grzybowski, B., *Science* **2002,** *295*, 2418-2421.

[8] Lehn, J.-M., *Science* **2002,** *295*, 2400-2403.

[9] Lehn, J.-M., *Angew. Chem. Inter. Ed.* **1990,** *29*, 1304-1319.

[10] Kimizuka, N.; Kawasaki, T.; Kunitake, T., *J. Am. Chem. Soc.* **1993,** *115*, 4387-4388.

[11] Lee, E.-C.; Kim, H.-J.; Park, S. Y., *Chem. Asian J.* **2019,** *14*, 1457-1461.

[12] Kim, H.-J.; Lee, H. J.; Chung, J. W.; Whang, D. R.; Park, S. Y., *Adv. Opt. Mater.* **2019,** *7*, 1801348.

[13] Kim, H.-J.; Nandajan, P. C.; Gierschner, J.; Park, S. Y., *Adv. Funct. Mater.* **2018,** *28*, 1705141.

[14] Tian, J.; Zhou, T. Y.; Zhang, S. C.; Aloni, S.; Altoe, M. V.; Xie, S. H.; Wang, H.; Zhang, D. W.; Zhao, X.; Liu, Y.; Li, Z. T., *Nat. Commun.* **2014,** *5*, 5574.

[15] Lee, H.-J.; Kim, H.-J.; Lee, E.-C.; Kim, J.; Park, S. Y., *Chem. Asian J.* **2018,** *13*, 390-394.

[16] Lee, H.-J.; Kim, J.; Abudulimu, A.; Cabanillas-Gonzalez, J.; Nandajan, P. C.; Gierschner, J.; Lüer, L.; Park, S. Y., *J. Phys. Chem. C* **2020,** *124*, 6971-6978.

[17] Tian, J.; Xu, Z. Y.; Zhang, D. W.; Wang, H.; Xie, S. H.; Xu, D. W.; Ren, Y. H.; Wang, H.; Liu, Y.; Li, Z. T., *Nat. Commun.* **2016,** *7*, 11580.

[18] Yang, X. Y.; Hu, Z. C.; Yin, Q. W.; Shu, C.; Jiang, X. F.; Zhang, J.; Wang, X. H.; Jiang, J. X.; Huang, F.; Cao, Y., *Adv. Funct. Mater.* **2019,** *29*, 1808156.

[19] Weingarten, A. S.; Kazantsev, R. V.; Palmer, L. C.; McClendon, M.; Koltonow, A. R.; Samuel, A. P.; Kiebala, D. J.; Wasielewski, M. R.; Stupp, S. I., *Nat. Chem.* **2014,** *6*, 964-70.

[20] Kaeser, A.; Schenning, A. P. H. J., *Adv. Mater.* **2010,** *22*, 2985-2997.

[21] Ringsdorf, H.; Schlarb, B.; Venzmer, J., *Angew. Chem. Int. Ed.* **1988,** *27*, 113-158.

[22] Cui, H.; Webber, M. J.; Stupp, S. I., *J. Pept. Sci.* **2010,** *94*, 1-18.

[23] Kim, Y.; Li, W.; Shin, S.; Lee, M., *Acc. Chem. Res.* **2013,** *46*, 2888-2897.

[24] Israelachvili, J. N.; Mitchell, D. J.; Ninham, B. W., *Journal of the Chemical Society, Faraday Transactions 2: Molecular and Chemical Physics* **1976,** *72*, 1525-1568.

[25] Szejtli, J., *Chem. Rev.* **1998,** *98*, 1743-1754.

[26] Yu, G.; Jie, K.; Huang, F., *Chem. Rev.* **2015,** *115*, 7240-7303.

[27] Pedersen, C. J., *J. Am. Chem. Soc.* **1967,** *89*, 2495-2496.

[28] Assaf, K. I.; Nau, W. M., *Chem. Soc. Rev.* **2015,** *44*, 394-418.

[29] Masson, E.; Ling, X.; Joseph, R.; Kyeremeh-Mensah, L.; Lu, X., *Rsc Adv.* **2012,** *2*, 1213-1247.

[30] Lee, J. W.; Samal, S.; Selvapalam, N.; Kim, H.-J.; Kim, K., *Acc. Chem. Res.* **2003,** *36*, 621-630.

[31] Lagona, J.; Mukhopadhyay, P.; Chakrabarti, S.; Isaacs, L., *Angew. Chem. Int. Ed.* **2005,** *44*, 4844-4870.

[32] Appel, E. A.; del Barrio, J.; Loh, X. J.; Scherman, O. A., *Chem. Soc. Rev.* **2012,** *41*, 6195-6214.

[33] Jiao, D.; Geng, J.; Loh, X. J.; Das, D.; Lee, T.-C.; Scherman, O. A., *Angew. Chem. Int. Ed.* **2012,** *51*, 9633-9637.

[34] Zhang, X.; Xu, X.; Li, S.; Wang, L.-H.; Zhang, J.; Wang, R., *Sci. Rep.* **2018,** *8*, 8819.

[35] Uzunova, V. D.; Cullinane, C.; Brix, K.; Nau, W. M.; Day, A. I., *Org. Biomol. Chem.* **2010,** *8*, 2037-2042.

[36] Barrow, S. J.; Kasera, S.; Rowland, M. J.; del Barrio, J.; Scherman, O. A., *Chem. Rev.* **2015,** *115*, 12320-12406.

[37] Jeon, Y. J.; Bharadwaj, P. K.; Choi, S.; Lee, J. W.; Kim, K., *Angew. Chem. Int. Ed.* **2002,** *41*, 4474-4476.

[38] Ma, D.; Hettiarachchi, G.; Nguyen, D.; Zhang, B.; Wittenberg, J. B.; Zavalij, P. Y.; Briken, V.; Isaacs, L., *Nat. Chem.* **2012,** *4*, 503-510.

[39] Hennig, A.; Bakirci, H.; Nau, W. M., *Nat. Methods* **2007,** *4*, 629-632.

[40] Ni, X.-L.; Chen, S.; Yang, Y.; Tao, Z., *J. Am. Chem. Soc.* **2016,** *138*, 6177-6183.

[41] Barooah, N.; Mohanty, J.; Bhasikuttan, A. C., *Chem. Commun.* **2015,** *51*, 13225-13228.

[42] Lehn, J.-M., *Eur. Rev.* **2009,** *17* (2), 263-280.

[43] Petkau-Milroy, K.; Brunsveld, L., *Org. biomol. chem.* **2013,** *11*, 219-232.

[44] Alberts, B.; Johnson, A.; Lewis, J.; Morgan, D.; Raff, M.; Keith Roberts, P. W., Molecular biology of the cell. **2018**.

[45] Kim, T.; Park, J. Y.; Hwang, J.; Seo, G.; Kim, Y., *Adv. Mater.* **2020**, 2002405.

[46] Chen, Z.; Yam, V. W.-W., *Angew. Chem. Int. Ed.* **2020,** *59*, 4840-4845.

[47] Chen, Z.; Chan, A. K.-W.; Wong, V. C.-H.; Yam, V. W.-W., *J. Am. Chem. Soc.* **2019,** *141*, 11204-11211.

[48] Yue, L.; Wang, S.; Zhou, D.; Zhang, H.; Li, B.; Wu, L., *Nat. commun.* **2016,** *7*, 1-10.

[49] Kim, Y.; Lee, M., *Chem. Eur. J.* **2015,** *21*, 5736-5740.

[50] Lee, E.; Kim, J. K.; Lee, M., *Angew. Chem.* **2009,** *121*, 3711-3714.

[51] Zhang, K. D.; Tian, J.; Hanifi, D.; Zhang, Y.; Sue, A. C.; Zhou, T. Y.; Zhang, L.; Zhao, X.; Liu, Y.; Li, Z. T., *J. Am. Chem. Soc.* **2013,** *135*, 17913-8.

[52] Liu, Y.; Yang, H.; Wang, Z.; Zhang, X., *Chem. Asian J.* **2013,** *8*, 1626-32.

[53] Xu, S. Q.; Zhang, X.; Nie, C. B.; Pang, Z. F.; Xu, X. N.; Zhao, X., *Chem. Commun.* **2015,** *51*, 16417-20.

[54] Zhang, Y.; Zhan, T. G.; Zhou, T. Y.; Qi, Q. Y.; Xu, X. N.; Zhao, X., *Chem. Commun.* **2016,** *52*, 7588-91.

[55] Reisner, E., *Angew. Chem. Int. Ed.* **2019,** *58*, 3656-3657.

[56] Wasielewski, M. R., *Chem. Rev.* **1992,** *92*, 435-461.

[57] Achilleos, D. S.; Yang, W.; Kasap, H.; Savateev, A.; Markushyna, Y.; Durrant, J. R.; Reisner, E., *Angew. Chem. Int. Ed.* **2020,** *59*, 18184-18188.

[58] Narayanam, J. M.; Stephenson, C. R., *Chem. Soc. Rev.* **2011,** *40*, 102-113.

[59] Graetzel, M., *Acc. Chem. Res.* **1981,** *14*, 376-384.

[60] Maeda, K.; Teramura, K.; Lu, D.; Takata, T.; Saito, N.; Inoue, Y.; Domen, K., *Nature* **2006,** *440*, 295-295.

[61] Wang, Q.; Hisatomi, T.; Katayama, M.; Takata, T.; Minegishi, T.; Kudo, A.; Yamada, T.; Domen, K., *Faraday Discuss.* **2017,** *197*, 491-504.

[62] Wang, Q.; Hisatomi, T.; Jia, Q.; Tokudome, H.; Zhong, M.; Wang, C.; Pan, Z.; Takata, T.; Nakabayashi, M.; Shibata, N., *Nat. mat.* **2016,** *15*, 611-615.

[63] Wang, Q.; Hisatomi, T.; Suzuki, Y.; Pan, Z.; Seo, J.; Katayama, M.; Minegishi, T.; Nishiyama, H.; Takata, T.; Seki, K., *J. Am. Chem. Soc.* **2017,** *139*, 1675-1683.

[64] Takata, T.; Jiang, J.; Sakata, Y.; Nakabayashi, M.; Shibata, N.; Nandal, V.; Seki, K.; Hisatomi, T.; Domen, K., *Nature* **2020,** *581*, 411-414.

[65] Wang, Z.; Li, C.; Domen, K., *Chem. Soc. Rev.* **2019,** *48*, 2109-2125.

[66] Tachibana, Y.; Vayssieres, L.; Durrant, J. R., *Nat. Photonics* **2012,** *6*, 511.

[67] Dau, H.; Limberg, C.; Reier, T.; Risch, M.; Roggan, S.; Strasser, P., *ChemCatChem* **2010,** *2*, 724-761.

[68] Pellegrin, Y.; Odobel, F., *C. R. Chim.* **2017,** *20*, 283-295.

[69] Lhermitte, C. R.; Sivula, K., *ACS Catal.* **2019,** *9*, 2007-2017.

[70] Wakerley, D. W.; Kuehnel, M. F.; Orchard, K. L.; Ly, K. H.; Rosser, T. E.; Reisner, E., *Nat. Energy* **2017,** *2*, 17021.

[71] Miller, D. S.; Bard, A. J.; McLendon, G.; Ferguson, J., *J. Am. Chem. Soc.* **1981,** *103*, 5336-5341.

[72] Willkomm, J.; Orchard, K. L.; Reynal, A.; Pastor, E.; Durrant, J. R.; Reisner, E., *Chem. Soc. Rev.* **2016,** *45*, 9-23.

[73] Kosco, J.; Moruzzi, F.; Willner, B.; McCulloch, I., *Adv. Energy Mater.* **2020,** *10*, 2001935.

[74] Baranoff, E.; Nakatsu, F.; Kamikawa, Y.; Liu, H. B.; Moriyama, M.; Kumazawa, K.; Yoshizawa, M.; Fujita, M.; Kato, T. In *A lyotropic liquid-crystalline molecular nano-cage*, 55th SPSJ Annual Meeting, Nagoya, Nagoya, 2006; p 688.

[75] Niu, P.; Zhang, L.; Liu, G.; Cheng, H.-M., *Adv. Funct. Mater.* **2012,** *22*, 4763-4770.

[76] Wang, X.; Maeda, K.; Thomas, A.; Takanabe, K.; Xin, G.; Carlsson, J. M.; Domen, K.; Antonietti, M., *Nat. Mater.* **2009,** *8*, 76-80.

[77] Wang, L.; Fernandez-Teran, R.; Zhang, L.; Fernandes, D. L.; Tian, L.; Chen, H.; Tian, H., *Angew. Chem. Int. Ed.* **2016,** *55*, 12306-10.

[78] Sprick, R. S.; Jiang, J.-X.; Bonillo, B.; Ren, S.; Ratvijitvech, T.; Guiglion, P.; Zwijnenburg, M. A.; Adams, D. J.; Cooper, A. I., *J. Am. Chem. Soc.* **2015,** *137*, 3265-3270.

[79] Sprick, R. S.; Bonillo, B.; Clowes, R.; Guiglion, P.; Brownbill, N. J.; Slater, B. J.; Blanc, F.; Zwijnenburg, M. A.; Adams, D. J.; Cooper, A. I., *Angew. Chem. Int. Ed.* **2016,** *55*, 1792-1796.

[80] Woods, D. J.; Sprick, R. S.; Smith, C. L.; Cowan, A. J.; Cooper, A. I., *Adv. Energy Mater.* **2017,** *7*), 1700479.

[81] Sprick, R. S.; Bonillo, B.; Clowes, R.; Guiglion, P.; Brownbill, N. J.; Slater, B. J.; Blanc, F.; Zwijnenburg, M. A.; Adams, D. J.; Cooper, A. I., *Angew. Chem. Int. Ed.* **2016,** *55*, 1792-6.

[82] Yang, C.; Ma, B. C.; Zhang, L.; Lin, S.; Ghasimi, S.; Landfester, K.; Zhang, K. A.; Wang, X., *Angew. Chem. Int. Ed.* **2016,** *55*, 9202-6.

[83] Zhang, G.; Lan, Z. A.; Wang, X., *Angew. Chem. Int. Ed.* **2016,** *55*, 15712-15727.

[84] Zhang, G.; Li, G.; Lan, Z. A.; Lin, L.; Savateev, A.; Heil, T.; Zafeiratos, S.; Wang, X.; Antonietti, M., *Angew. Chem. Int. Ed.* **2017,** *56*, 13445-13449.

[85] Pati, P. B.; Damas, G.; Tian, L.; Fernandes, D. L. A.; Zhang, L.; Pehlivan, I. B.; Edvinsson, T.; Araujo, C. M.; Tian, H. N., *Energy Environ. Sci.* **2017,** *10*, 1372-1376.

[86] Yang, H.; Li, X.; Sprick, R. S.; Cooper, A. I., *Chem. Commun.* **2020,** *56*, 6790-6793.

[87] Kosco, J.; Sachs, M.; Godin, R.; Kirkus, M.; Francas, L.; Bidwell, M.; Qureshi, M.; Anjum, D.; Durrant, J. R.; McCulloch, I., *Adv. Energy Mater.* **2018,** *8*, 1802181.

[88] Sachs, M.; Cha, H.; Kosco, J.; Aitchison, C. M.; Francàs, L.; Corby, S.; Chiang, C.-L.; Wilson, A. A.; Godin, R.; Fahey-Williams, A.; Cooper, A. I.; Sprick, R. S.; McCulloch, I.; Durrant, J. R., *J. Am. Chem. Soc.* **2020,** *142*, 14574-14587.

[89] Wang, L.; Fernández-Terán, R.; Zhang, L.; Fernandes, D. L. A.; Tian, L.; Chen, H.; Tian, H., *Angew. Chem. Int. Ed.* **2016,** *55*, 12306-12310.

[90] Bai, Y.; Hu, Z.; Jiang, J.-X.; Huang, F., *Chem. Asian J.* **2020,** *15*, 1780-1790.

[91] Dumele, O.; Chen, J.; Passarelli, J. V.; Stupp, S. I., *Adv. Mater.* **2020,** *32*, 1907247.

[92] McDowall, D.; Greeves, B. J.; Clowes, R.; McAulay, K.; Fuentes-Caparrós, A. M.; Thomson, L.; Khunti, N.; Cowieson, N.; Nolan, M. C.; Wallace, M.; Cooper, A. I.; Draper, E. R.; Cowan, A. J.; Adams, D. J., *Adv. Energy Mater.* **2020**, 2002469.

[93] Tian, J.; Zhang, Y.; Du, L.; He, Y.; Jin, X.-H.; Pearce, S.; Eloi, J.-C.; Harniman, R. L.; Alibhai, D.; Ye, R.; Phillips, D. L.; Manners, I., *Nat. Chem.* **2020,** *12*, 1150-1156.

[94] Weingarten, A. S.; Kazantsev, R. V.; Palmer, L. C.; Fairfield, D. J.; Koltonow, A. R.; Stupp, S. I., *J. Am. Chem. Soc.* **2015,** *137*, 15241-6.

[95] Hestand, N. J.; Kazantsev, R. V.; Weingarten, A. S.; Palmer, L. C.; Stupp, S. I.; Spano, F. C., *J. Am. Chem. Soc.* **2016,** *138*, 11762-11774.

Chapter 2.

Highly Luminescent and Water-Soluble Two-Dimensional Supramolecular Organic Framework Self-Assembled from a Cyanostilbene-Based Trilateral Molecule and Cucurbit[8]uril

2.1. Introduction

Recently, host-guest reaction between cucurbit[8]uril (CB[8]) and aromatic cations has been extensively explored[1-11] as a viable strategy for synthesizing water-soluble organic structures. CB[8]-based one-dimensional (1D) supramolecular polymers,[1,2,12-14] two-dimensional (2D) supramolecular organic frameworks (SOFs),[15-19] and three-dimensional (3D) SOFs[20,21] have received much attention because of their diverse potential applications. Among them, 2D SOFs are attracting more attention, because they form well-ordered single-layer structures in water by easy fabrication. Since the 2D SOFs are fabricated by the bottom-up self-assembly of CB[8] and planar multilateral guest molecules, their characteristics can be precisely tailored by designing and employing appropriate guest molecules. For practical application of 2D SOFs to biosensors or bio-imaging for example, high fluorescence quantum yields (Φ_F) and well-defined 2D structure formation are essential. Hence, innovative design of multi-

lateral planar guest molecules for highly luminescent 2D SOFs are requested to overcome the prevalent 'concentration fluorescent quenching' effect commonly observed in the π–conjugated organic materials. So far, two different multi-lateral guest molecules forming turn-on fluorescent 2D SOFs with CB[8] hosts, *i.e.* triphenylamine[16] and tetraphenylethylene[17]-based multi-lateral guest molecules, have been reported. While the formation of 2D SOFs was successfully demonstrated for these guest molecules, size of 2D SOFs was rather small (< 100 nm) and their fluorescing behavior is quite elusive without reporting any quantitative measurements of Φ_F and/or fluorescent lifetime (τ_F). Therefore, I aimed at developing novel multi-lateral guest molecule for large-size 2D SOF with practically remarkable level of high Φ_F in this work together with the complete elucidation of its photophysical properties.

With strong self-assembling behavior and enhanced fluorescence emission in the solid state, cyanostilbene derivatives have long been explored as unique building blocks for highly luminescent crystals and supramolecules.[22-24] In particular, water-soluble cationic cyanostilbene derivative **2** (Scheme 2-1) was very recently demonstrated to form exceptionally stable ($K \sim 10^9$) complexes with CB[8] to generate 1D supramolecular polymer (SP) with very high Φ_F of 0.91 attributed to the J-aggregation of bilateral cyanostilbene chromophores in the cavity of CB[8] (Note that **2** is completely non-emissive ($\Phi_F \sim 0$) in water before complexation with CB[8] according to the general 'floppy molecule' characteristics of cyanostilbene chromophore).[25] Therefore, in the present work, trilateral cationic cyanostilbene molecule **1** is rationally

designed as the most eligible water-soluble guest molecule for highly fluorescent 2D SOF.

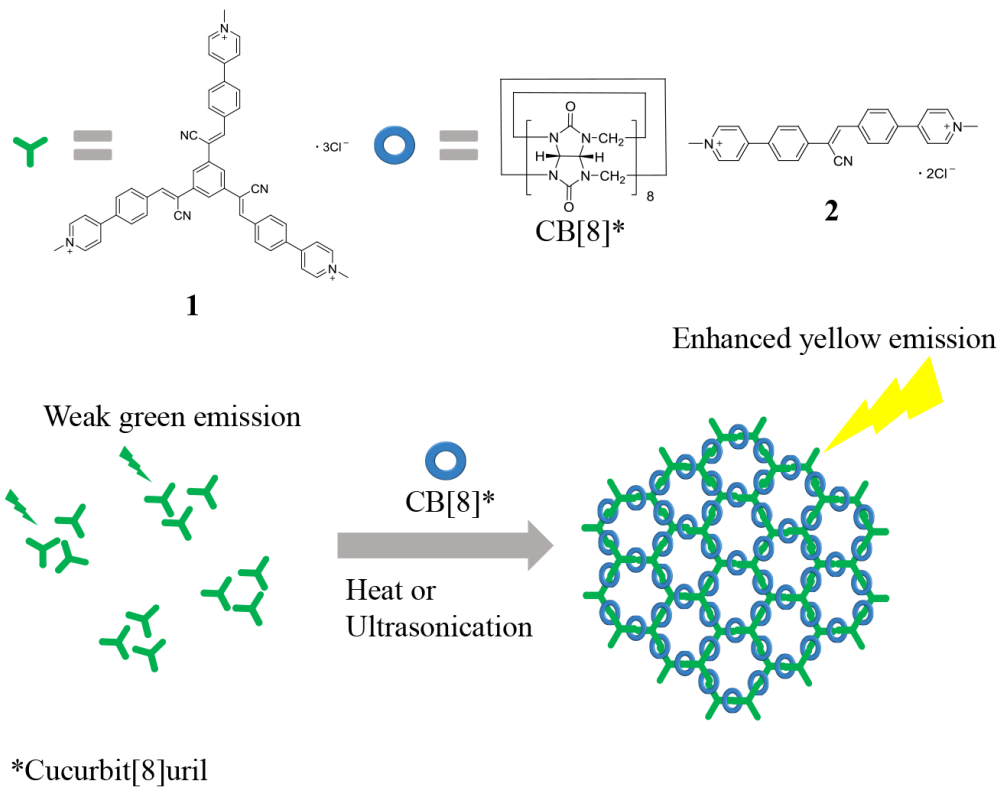

Scheme 2-1. Structures of cationic cyanostilbenes (1 and 2), cucur-bit[8]uril(CB[8]), and 2D SOF.

2.2. Experimental Section

Materials: All chemicals were purchased from Sigma-Aldrich, Acros, and Alfa Aesar, and used without further purification. Thin layer chromatography (TLC) plates (silica gel 254, Merck Co.) were used to monitor reactions, spots were visualized by hand held UV lamp at 254 or 365 nm. Column chromatography was conducted to separate crude compounds by using silica gel 60G (particle size 5-40 μm, Merck Co.).

Synthesis of Tri(cyanomethyl)benzene (2): Tri(cyanomethyl)benzene was synthesized according to the literature procedure.[26] Sodium cyanide (3.3 g, 67.2 mmol) was dispersed in 50 ml DMSO at 40 °C. 1,3,5-tri(bromomethyl)benzene (4 g, 11.2 mmol) was dissolved in 15 ml DMSO and the solution was dropped slowly during 1.5 h. The mixture was stirred at 40 °C for 15 h. The solution was cooled to room temperature and poured into 200 ml of ice water. Then it was extracted with diethyl ether and dichloromethane. The combined organic layer was washed with brine and water, dried using $MgSO_4$, and was evaporated.

Pale yellow solid, Yield: 1.7 g (77 %). ^{1}H NMR (300 MHz, $CDCl_3$) δ 3.80 (s, 6H), 7.31 (s, 3H)

Synthesis of 4-(4-Fomylphenyl)pyridine (5): 4-bromobenzaldehyde (5 g, 27.2 mmol) was dissolved in 40 ml toluene, and a 50ml aqueous solution of 4-pyridineboronic acid

(4 g, 32.6 mmol) and K_2CO_3 (14 g, 101 mmol) was added, then 40 ml isopropyl alcohol was added finally. The mixture was stirred at 80 °C and degassed by using N_2 bubbles for 30 mins. Tetrakis(triphenylphosphine)palladium(0) (0.89 g, 0.8 mmol) was dissolved in 20 ml toluene, degassed by using N_2 bubbles for 30 mins, then it was added to the mixture dropwise. The mixture was stirred overnight at 80 °C at N_2 atmosphere. The mixture was cooled to room temperature, poured into water (200 ml) and extracted with ethyl acetate (200 ml) three times. The combined organic layer was dried over MgSO4 and evaporated. The crude product was purified by using column chromatography (elunt, hexane : ethyl acetate = 5 : 5, v/v) to give a white crystalline product.

White solid, Yield: 4.9 g (98 %). ^{1}H NMR (300 MHz, $CDCl_3$) δ 7.54 (dd, J = 4.5, 1.6 Hz, 2H), 7.80 (d, J = 8.2 Hz, 2H), 8.01 (d, J = 8.3 Hz, 2H), 8.73 (dd, J = 4.5, 1.6 Hz, 2H), 10.10 (s, 1H)

Synthesis of (6): Tri(cyanomethyl)benzene (0.7 g, 3.59 mmol) and 4-(4-Fomylphenyl)pyridine (2.17g, 11.8 mmol) were dissolved in 18 ml THF, 18 ml tert-Butyl alcohol was added, and the solution was degassed by using N2 bubbles for 30 mins at 50 °C. Then, 0.54 ml of 1M tetrabutylammonium hydroxide solution in methanol was added slowly, and the solution was stirred further 20 mins at 50 °C, at N2 atmosphere. The solution was cooled to room temperature, and poured into cold methanol (100 ml). The crude product was filtered and the residue was washed with

methanol thoroughly to give pale yellow product.

Pale yellow solid, Yield: 1.6 g (65 %). ^{1}H NMR (300 MHz, $CDCl_3$) δ 7.57 (d, J = 4.7 Hz, 6H), 7.76 (s, 3H), 7.81 (d, J = 7.9 Hz, 6H), 8.02 (s, 3H), 8.10 (d, J = 8.0 Hz, 6H), 8.73 (d, J = 4.5 Hz, 6H)

Synthesis of (7): 6 (1 g, 1.45 mmol) was dissolved in 60 ml DMF, and iodomethane (6.17 g, 43.5 mmol) was added dropwise. The solution was further stirred overnight in room temperature. After that, the solution was poured into 100 ml dichloromethane, filtered, and the residue washed with dichloromethane thoroughly to give red product.

Red solid, Yield: 1.6 g (100 %). ^{1}H NMR (300 MHz, DMSO) δ 4.37 (S, 9H), 8.2 ~ 8.38 (m, 15H), 8.46 (s, 3H), 8.60 (d, J = 6.8 Hz, 6H), 9.08 (d, J = 6.5 Hz, 6H)

Synthesis of molecule 1 (8): 7 (1.4 g, 1.25 mmol) was dissolved in 30 ml DMSO, and a 20 ml MeOH solution of Tetrabutylammonium chloride (5g, 18 mmol) was added dropwise. The solution was further stirred for 2 days, poured into 150 ml toluene. Pale yellow solid was collected by filtration and washed with toluene to give the product.

Pale yellow solid, Yield: 1 g (95 %). ^{1}H NMR (300 MHz, MeOD) δ 4.43 (S, 9H), 8.14 ~ 8.38 (m, 18H), 8.49 (d, J = 6.9 Hz, 6H), 8.94 (d, J = 6.9 Hz, 6H). MS (ESI) (calcd m/z for $C_{51}H_{39}N_6^{3+}$ 245.44; found, 245.5) m/z: 278.2, 277.9, 277.5, 256.2, 247,9, 245.7, 245.5, 242.4, 240.6, 222.5

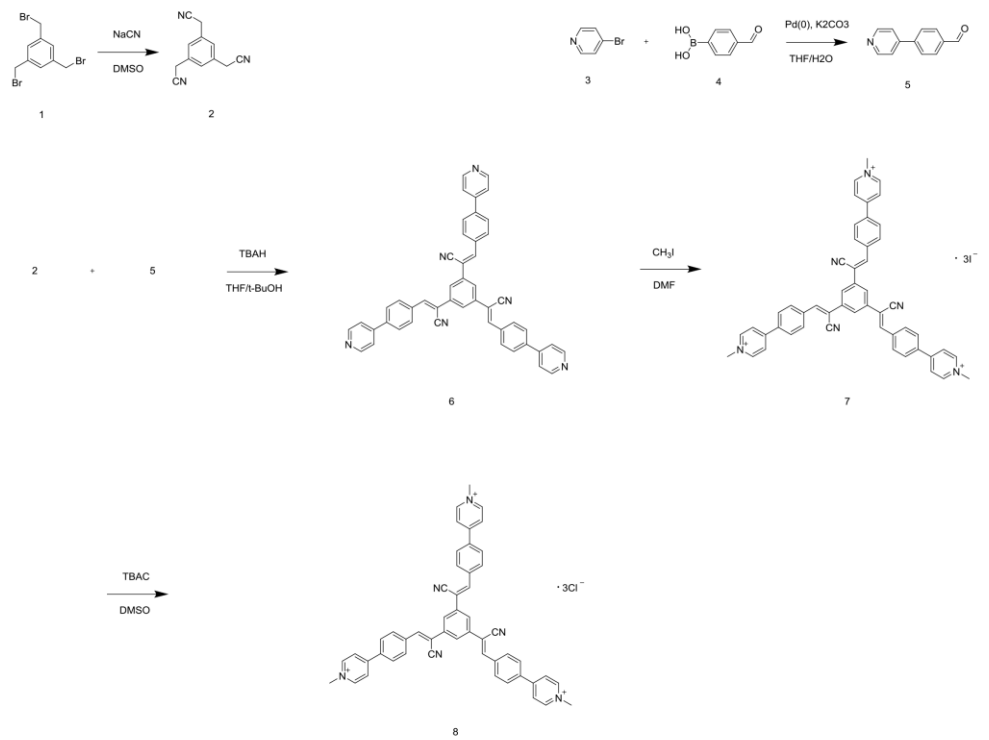

Scheme 2-2. Synthetic route of **1**.

Measurements: ^{1}H NMR spectra were measured by a Bruker AVANCE-300 NMR spectrometer. Mass spectrometry (MS) spectrum was measured by a Thermo Finnigan, LTQ. UV/Vis absorption spectra were recorded on a Shimazu, UV-1650 PC spectrometer. Fluorescence emission spectra were collected on a Photo Technology International, Felix32 QM-40 and a Varian, Cary Eclipse Fluorescence spectrophotometer. Temperature dependent FL spectra were collected by using a single

cell Peltier accessory. The absolute photoluminescence quantum yield (PLQY, Φ_F) were acquired on an integrating sphere (Lasphere Co., 600 diameter). Time-resolved fluorescence lifetime were acquired by the time-correlated single photon counting (TCSPC) technique on a FluoTime200 spectrometer (PicoQuant) equipped with a PicoHarp300 TCSPC board (PicoQuant) and a PMA182 photomultiplier (PicoQuant). a 375 nm picoseconds pulsed diode laser (PicoQuant, LDH375) driven by a PDL800-D driver (PicoQuant) with fwhm ~70 ps was used as an excitation source. Fluorescent lifetimes were calculated by using a Fluofit softwater (PicoQuant) with the IRF. Dynamic Light Scattering (DLS) experiments were performed on an Otsuka Electronics, DLS-7000. Solution state small angle x-ray scattering (SAXS) spectra recorded on a Bruker D8 Discover by using Cu Kα radiation. Atomic force microscopy (AFM) images were acquired on a Herzogenrath, Nanostation Ⅱ. Field emission scanning electron microscope (FE-SEM) images were acquired on a ZEISS, MERLIN Compact. The AFM and SEM samples were prepared by dropping a droplet of each aqueous solution on a UV ozone plasma treated SiO_2 substrate (oxide thickness 300 nm, 1 cm x 1 cm) and drying them. Transmission electron microscope (TEM) images were acquired on a JEOL, JEM-2100F and JEM-ARM200F. The TEM samples were prepared by dropping a droplet of each aqueous solution on a copper grid and drying them. Confocal laser scanning microscopy (CLSM) images were acquired on a Leica, SP8 X, and 405 nm diode laser was used as an excitation source.

Calculation: Semi-empirical calculations were performed by PM5 method in CAChe Worksystem Pro (version 7.5.0). Detailed conditions were followed as reported in previous studies on chromophore-CB[n], host-guest complex.[27-29] For a simple calculation, a 2-functional model compound was selected instead of **1**. To calculate large molecular complex, keyword MOZYME was used, and the continuum solvation model 'COSMO' was selected to mimic aqueous solution conditions.

2.3. Results and Discussion

1 was synthesized by the Knoevenagel reaction of 1,3,5-benzenetriacetonitrile with 4-(pyridine-4-yl)benzaldehyde and was fully identified as shown in Scheme 2-2. Since **1** comprises an N-methylpyridinium cation and is stabilized by a counter chloride ion, it is apparently dissolved in water and reacts with CB[8] hosts. While **2** is molecularly soluble in water and thus is completely non-emissive,[25] however, **1** formed nanosized structures in aqueous solution with moderate fluorescence emission due to the larger hydrophobic portion in **1** than that in **2**. In fact, structures of ~10 nm diameter were observed by dynamic light scattering (DLS) measurements (Figure 2-1a).

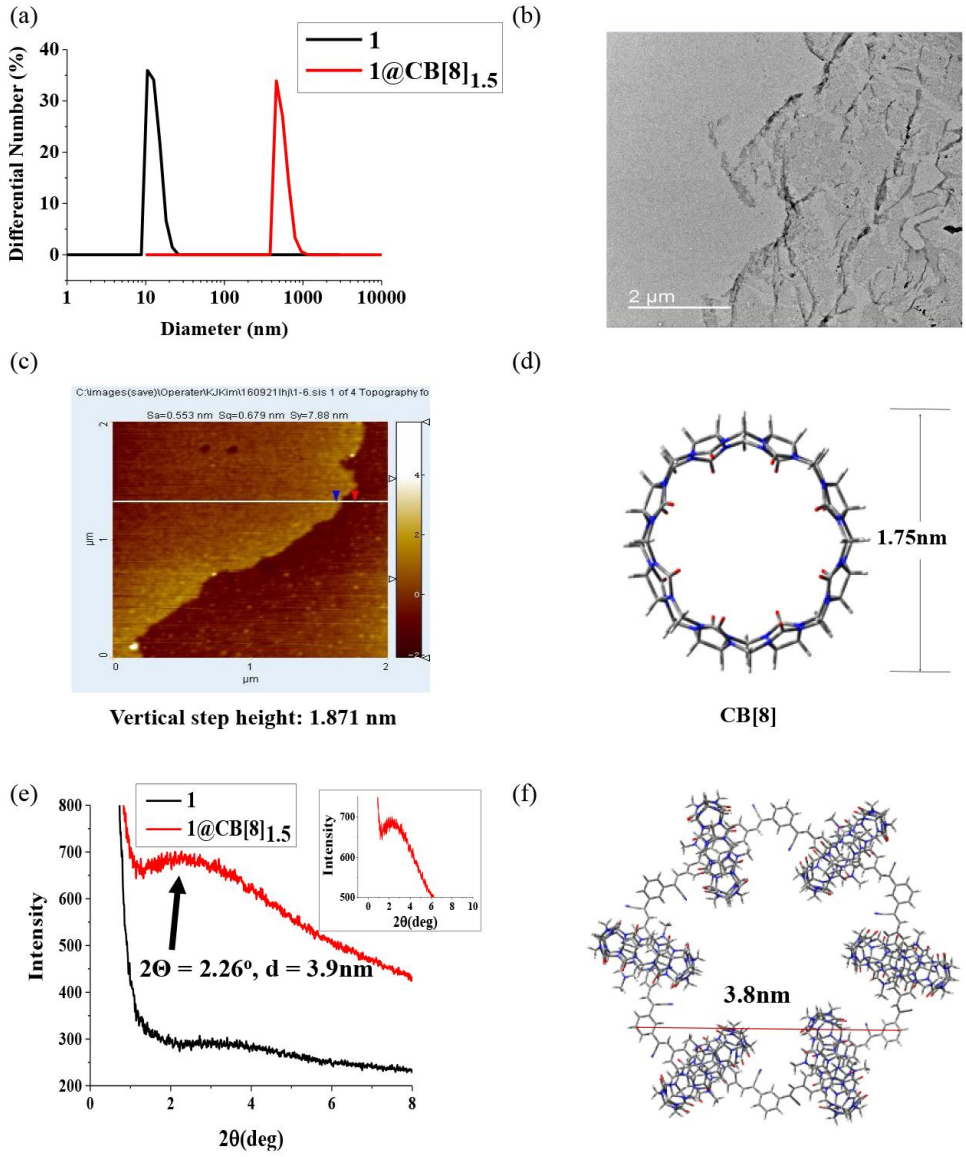

Figure 2-1. Self-assembled structures of 1 and the 2D SOF. (a) dynamic light scattering data of the nanoparticles of 1 and the 2D SOF made from 1 mM aqueous solution of 1 and CB[8]. (b) TEM image of the 2D SOF made from the 0.1 mM aqueous solution of 1 and CB[8]. (c) AFM image (2 μm x 2 μm) of the 2D SOF film

created via drop casting. (d) Molecular structure of CB[8] and its outer ring diameter. (e) Solution SAXS spectra of the 0.01 mM 1 aqueous solution and the 2D SOF in water made from 0.01 mM aqueous solution of 1 and 0.5 mM aqueous solution of CB[8] (inset: enlarged spectrum of the scattered X-rays from the 2D SOF aqueous solution). (f) Calculated optimal structure of the model honeycomb unit and its size in water by PM5 (hydrogen atoms are omitted for clarity).

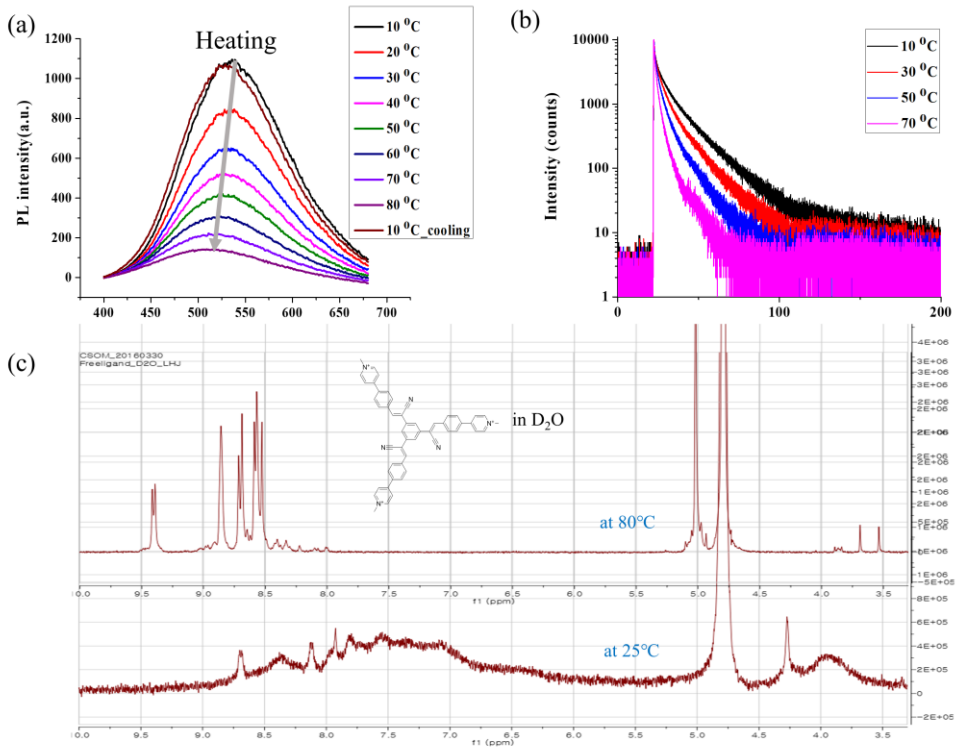

Figure 2-2. Temperature dependent characteristics of **1** (a) Fluorescence spectrum (b) fluorescent decay profiles (c) Temperature dependent NMR spectrum

Since the formation of nanoparticles rely on weak intermolecular interactions between molecules **1**, the self-assembly interactions could be easily broken by moderate

external stimuli. Consequently, their Φ_F and τ_F values decreased with increasing temperature (Tables 2-1 and 2-2). The nanoparticles of **1** in water exhibited a relatively strong excimer emission (λ_{em} = 536 nm, Φ_F = 0.10) at 10 °C. However, they became weakly emissive (λ_{em} = 526 nm, Φ_F = 0.01) at 50 °C and was almost non-emissive at 70 °C (Table 2-2; Figure 2-2a). On the other hand, the fluorescence intensity remained invariant when cooled down from 10 °C (Figure 2-2). Additionally, at the same temperature range of 10 ~ 70 °C, the average τ_F also decreased from 3.71 to 0.98 ns in time-correlated single photon counting (TCSPC) measurements (Figure 2-2b, Table 2-2). While the ^{1}H-NMR peaks of **1** were blurred and broad at 25 °C, they became sharp and clear at 80 °C (Figure 2-2a and b). All these experimental results comprehensively support that the emissive nanoparticles of **1** are reversibly disassembled upon heating and reassembled upon cooling, respectively.

Moreover, I could effectively break the self-assembly interactions of **1** by ultrasonication and/or complexation with CB[8] as well. Very uniquely, 2D SOF formation process from nanoparticles of **1** and CB[8] could be monitored by real-time fluorescence titration experiment. Photoluminescence spectra were repeatedly recorded while 1 mM CB[8] aqueous solution was added dropwise in varying portions to 0.01 mM aqueous solution of **1** under ultrasonication as shown in Figure 2-3a. With increasing amount of CB[8] addition, fluorescence intensity was gradually enhanced with its emission peak red shifted, which however became saturated when the **1**:CB[8] molar concentration reached a theoretical stoichiometric ratio of 2:3 for 2D SOF.

This observation clearly evidences the formation of 2D SOF. In addition, the evolution of the UV-vis absorption peak shown in Figure 2-3b also evidences the 2:3 stoichiometric point and further suggests the J-type stacking of luminescent units in 2D SOF based on the red-shifted absorption. Further evidence of 2D SOF formation was found in the aromatic peaks of the ^{1}H-NMR spectrum (δ 7.6 ~ 8.0 m, 8.1 s, 8.6 d) which disappeared after the 2:3 molar ratio was reached during titration as shown in Figure 2-4. Practically, the precise stoichiometry of 2:3 could be determined from a Job plot derived from fluorescence intensity at 585 nm as shown in Figure 2-5. It was thus unambiguously proven that the nanoparticles of **1** was disassembled and transformed to the stable 2D SOF upon the addition of CB[8] under ultrasonication (Scheme 2-1).

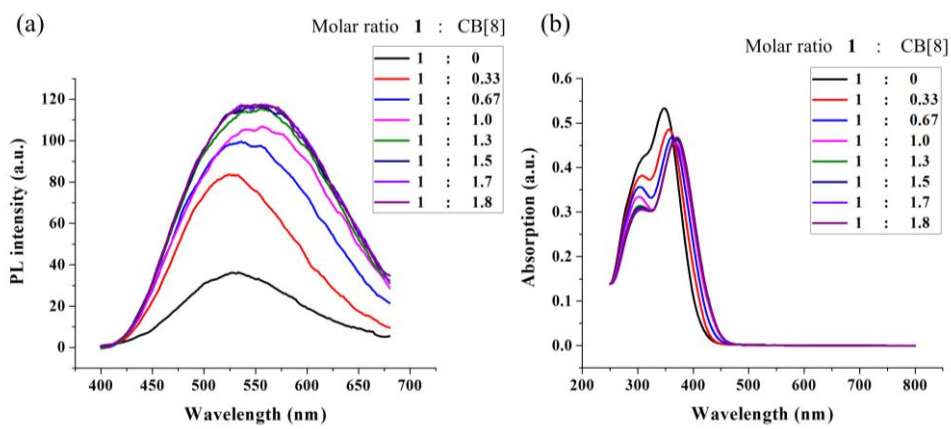

Figure 2-3. (a) Fluorescence spectrum change and (b) UV-Vis spectrum change for different **1**:CB[8] ratios in the titration of 0.5 mM aqueous solution of CB[8] with 0.01 mM aqueous solution of **1**.

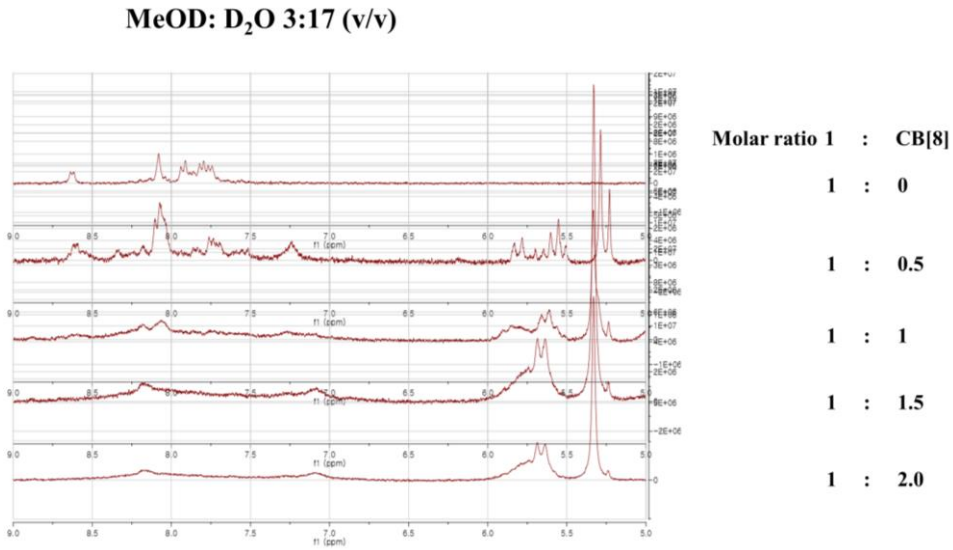

Figure 2-4. NMR titration result.

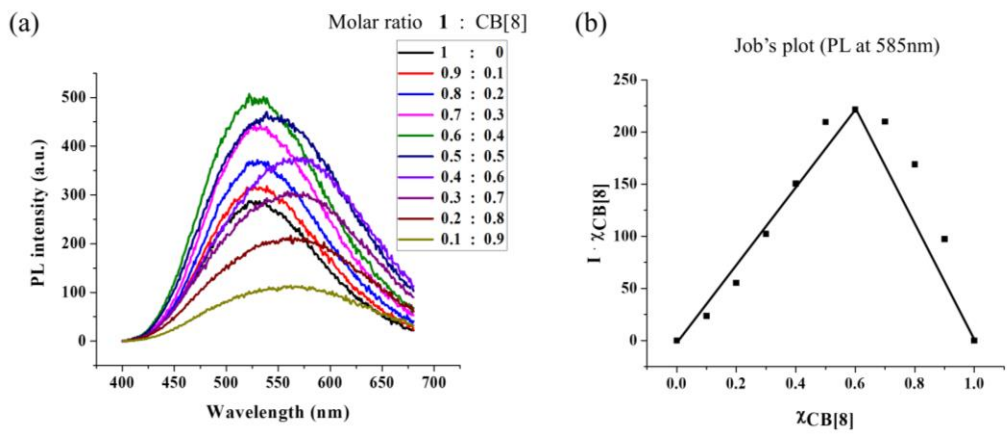

Figure 2-5. Job's plot derived from fluorescence intensity at 585 nm, I: intensity at 585 nm of mixture solution of 1 and CB[8], $\chi_{CB[8]}$: molar fraction of CB[8] in a mixture.

Formation of 2D SOF was directly observed by its morphological and structural

evolution. In DLS measurements, the size of the 2D SOF made from 1 mM aqueous solution of **1** increased close to 1 μm with its average diameter of 548 nm (Figure 2-1a). Structural features of 2D SOF dry-films were also investigated by electron microscopy. A film was simply created by drop casting the 2D SOF water solution on a copper grid. This was subsequently analyzed by transmission electron microscopy (TEM) that displayed single-layer structures with large diameters ≤ 10 μm (Figures 1b). When 2D SOF film cast on a SiO2 substrate was measured by atomic force microscopy (AFM), it was found that the film had a very flat surface with a roughness smaller than 0.2 nm. The actual thickness of the 2D SOF film was evaluated by AFM depth profile data as ~1.87 nm (see Figures 2-1c). Since the outer ring diameter of CB[8] is ~1.75 nm[15], this film is assigned as the single 2D SOF layer.

The lateral regularities of the 2D SOF in water were examined by solution small-angle X-ray scattering (SAXS) measurements. For nanoparticles of **1** in water, the peak was too weak and broad to be assigned and analyzed (Figure 2-1e). However, for the 2D SOF in water, the peak could be assigned as $2\theta = 2.26°$ with the spacing calculated as 3.9 nm (Figure 2-1e). This value is consistent with the size of each honeycomb repeating unit shown in the calculated nanoporous 2D SOF model (Figure 2-1f). Here the computational calculation was conducted similar to the previously reported method used for other CB[8] based host-guest system.[15,16,19,30-32]

Table 2-1. Optical characteristics of 1, the nanoparticles of **1** and the 2D SOF.

Species	λ_{em}[a] [nm]	τ_f[b] [ns]	k_r[c]/k_{nr}[d] [10^7 S^{-1}]	Φ_F[e]
Monomer (**1** at 70 °C)	520	0.98	-	<0.01
Nanoparticle (**1** at 25 °C)	535	2.25	2.22 / 42.2	0.05
2D SOF	585	19.7	3.05 / 2.03	0.60

[a]Excited at 350 nm, peak intensity; [b]amplitude averaged fluorescent lifetime; [c]rate constant of radiative decay and [d]non radiative decay; [e] absolute photoluminescence quantum yield (excited at 350 nm).

Table 2-2. Temperature dependent fluorescent lifetime and photoluminescence quantum yield of 1 in water (0.01 mM).

Temperature	λ_{em}[a]	τ_f[b] [ns]	τ_a (amplitudes a_i) [ns]	Φ_F[c]
10 ˚C	536	3.71	19 (0.10) / 6.0 (0.23) / 0.60 (0.67)	0.10
30 ˚C	532	2.14	15 (0.05) / 4.4 (0.22) / 0.54 (0.73)	0.04
50 ˚C	526	2.00	14 (0.04) / 3.6 (0.30) / 0.58 (0.66)	0.01
70 ˚C	511	0.98	7.0 (0.04) / 1.9 (0.28) / 0.30 (0.69)	<0.01

a. Excited at 350nm, peak intensity

b. Amplitude averaged fluorescent lifetime

c. Excited at 350 nm, absolute PLQY

Since the formation of CB[8]-based 2D SOF was unambiguously clarified as shown above, I now turn to the unique state-dependent fluorescence behavior of **1** in more detail. Since **1** is self-assembled into nanoparticles at 25 °C, its characteristics do not

represent those of monomer **1**. Instead, the characteristics measured at 70 °C should represent those of isolated monomer **1**. Strikingly different fluorescence characteristics were observed from the monomer-like state to the nanoparticles of **1**, and eventually to the 2D SOF. While monomer **1** was almost non-emissive ($\Phi_F \sim 0$), the nanoparticles of **1** in water displayed relatively weak green emissions ($\Phi_F = 0.05$) peaked at 532 nm, and the 2D SOF in water exhibited far enhanced yellow emissions ($\Phi_F = 0.60$) peaked at 585 nm (Table 2-1, Figure 2-6). Moreover, τ_F values for three different samples (monomer, nanoparticle, and 2D-SOF) were precisely measured by TCSPC measurements. All samples showed multi-exponential decay (see Figure 2-6 and Table 2-2 for detailed information), and their average τ_F were calculated as listed in Table 2-1. It is noted that τ_F was increased from 0.98 ns in monomer **1** to 2.25 ns in the nanoparticles of **1**, and eventually to 19.7 ns in the 2D SOF (Table 2-1, Figure 2-6). To understand the mechanism of fluorescence enhancement in 2D-SOF, the rate constants of radiative (k_r) and non-radiative decay (k_{nr}) of the nanoparticles of **1** and 2D SOF were calculated from their average τ_F and Φ_F values. Compared to the nanoparticles of **1**, 2D SOF displayed a 1.5 times increase in k_r most likely attributed to the J-stacking in it. On the other hand, k_{nr} of the 2D SOF was reduced to ~1/20 of nanoparticles **1**, indicating that the non-radiative decay path was significantly restricted through rigidification imposed by the interwoven structure of 2D SOF. Consequently, radiative decay became much faster than non-radiative decay in the 2D SOF to render its Φ_F highly enhanced up to 0.60.

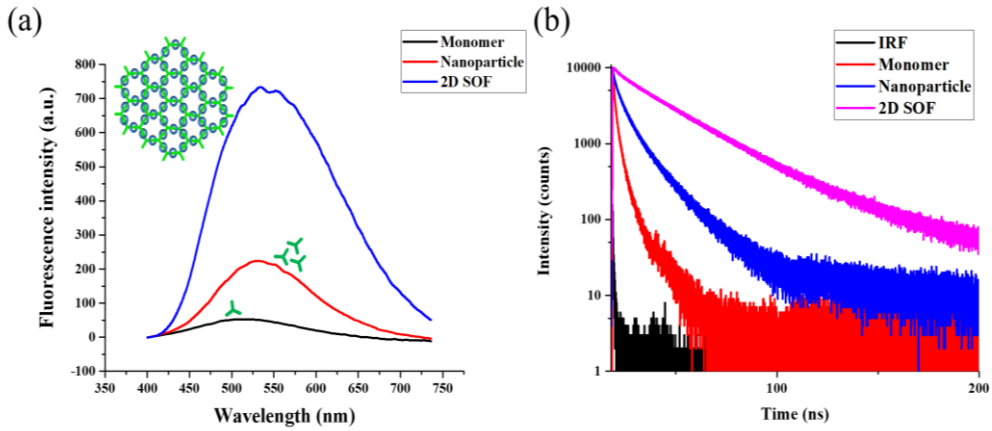

Figure 2-6. (a) Fluorescence spectra and fluorescence decay spectra of **1** monomer (0.01 mM **1** aqueous solution at 70 ºC), the nanoparticles of **1** (0.01 mM **1** aqueous solution at 25 ºC), and the 2D SOF in water made from the 0.01 mM **1** aqueous solution and the 0.5 mM aqueous solution of CB[8] (for (a) excited at 350 nm, for (b) excited by 375 nm LASER).

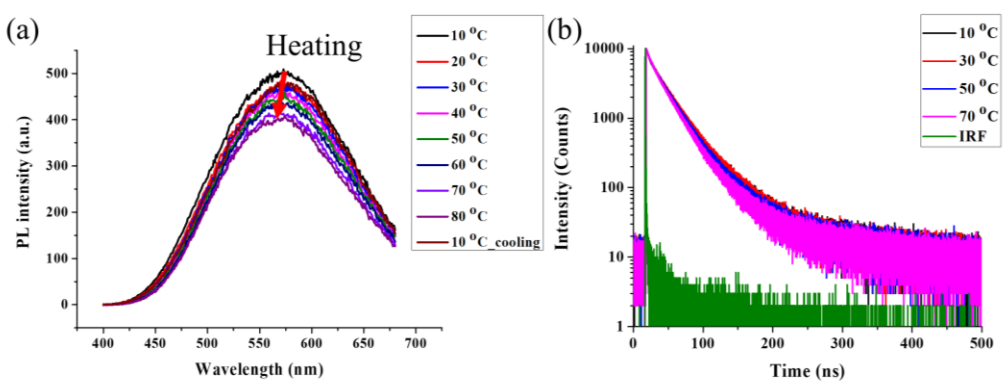

Figure 2-7. The temperature dependent (a) fluorescence spectra and (b) fluorescence decay specta of the 2D SOF (for (a) excited at 350 nm, for (b) excited by 375 nm LASER).

As mentioned above, rigidification is one of the major mechanisms that can explain the enhanced Φ_F in 2D SOF. Considering the principle of CB[8]-based supramolecular formation, this strong rigidity of the 2D SOF was mainly attributed to the strong binding interaction between **1** and CB[8]. The remarkably strong interactions between **1** and CB[8] in 2D SOF were also demonstrated by temperature-dependent fluorescence measurements. In contrast to the complete fluorescence quenching of nanoparticles of **1** upon heating from 25 °C to 70 °C, only a 13% decrease in Φ_F was observed for 2D SOF case (Table 2-2, from Φ_F = 0.63 to Φ_F = 0.55). Additionally, the τ_F of 2D SOF in water remained almost identical (Table 2-2, Figure 2-7, from $\tau_{f,\ average}$ = 20.5 ns to $\tau_{f,\ average}$ = 19.3 ns). Therefore, it is to be mentioned that 2D SOF is so stable as to maintain its high Φ_F even at elevated temperatures because of the relatively strong binding between **1** and CB[8].

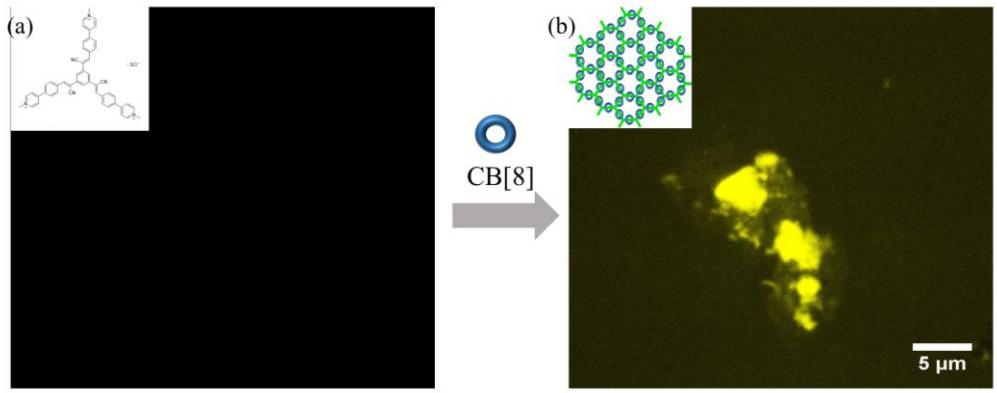

Figure 2-8. Conforcal laser scanning microscopy images for (a) **1** and (b) the 2D SOF in aqueous solution.

Because of its strong fluorescence intensity in water and/or in film, the 2D SOF could be clearly imaged by confocal laser scanning microscopy (CLSM, Figure 2-8), when a drop of 2D SOF in water was placed on a glass slide at 25 ° C. Under 405 nm illumination, highly emissive structures (≤ 5 μm) were observed suggesting its possible use as bio-imaging or sensing material.

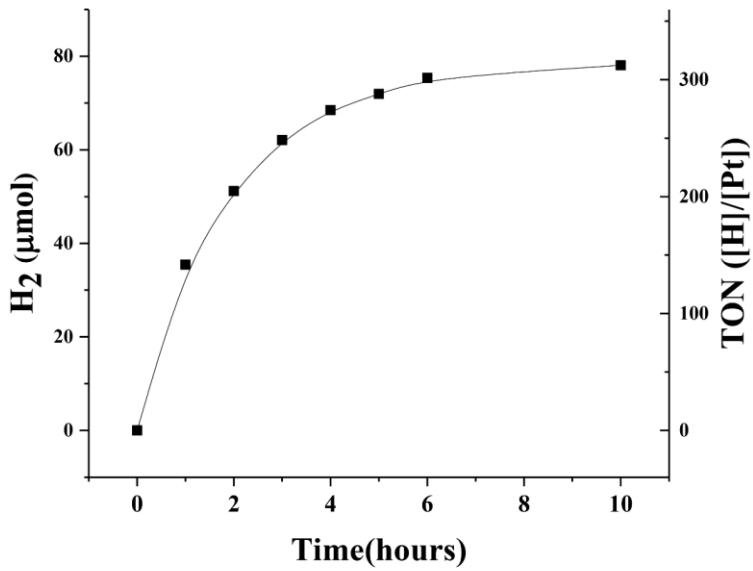

Figure 2-9. H_2 evolution curve for using the supramolecular photosensitizer. TON=n(H)/n(catalyst).

Since it has advantages like 1) relatively long exciton lifetime, 2) large surface area, and 3) good compatibility in water, we decided to explore the possible use of 2D SOF as a supramolecular photosensitizer for visible light driven H_2 evolution in water. Especially, the development of effective photosensitizer working in pure water has been an important issue in photocatalytic H_2 evolution.[33-36] To harvest visible light more effectively, an anionic red dye 2′ ,4′ ,5′ ,7′ -tetraiodofluorescein disodium salt, namely erythrosin B was used with the 2D SOF as a co-photosensitizer. Because of the cationic character of their guest molecules, nano-porous 2D SOFs based of CB[8]

could effectively interact with anions by forming weak acid-base pairs.[20] The 2D SOF made from 0.65 μmol of 1 and 0.975 μmol of CB[8] with 0.65 μmol of erythrosin B was used as a supramolecular photosensitizer, 0.5 μmol of colloidal Pt as a catalyst, and 2 mmol of ascorbic acid as a sacrificial reagent.

2.4. Conclusions

In conclusion, I successfully fabricated a water-soluble highly fluorescent 2D SOF by a host-guest reaction between CB[8] and novel water-soluble trilateral molecule **1**. The novel trilateral molecule **1** exhibited state-dependent structural and fluorescent properties. Three different states of **1** in water could be reversibly interconverted including non-emissive monomer, moderately emissive nanoparticle (average diameter = 12.9 nm, Φ_F = 0.05), and a molecularly thin and honeycomb-shaped highly emissive 2D SOF (average diameter = 548 nm, Φ_F = 0.60).

2.5. References

[1] del Barrio, J.; Horton, P. N.; Lairez, D.; Lloyd, G. O.; Toprakcioglu, C.; Scherman, O. A. *J. Am. Chem. Soc.* **2013**, 135, 11760.

[2] Huang, Z.; Yang, L.; Liu, Y.; Wang, Z.; Scherman, O. A.; Zhang, X. *Angew. Chem. Int. Ed.* **2014**, 53, 5351.

[3] Kim, K.; Selvapalam, N.; Ko, Y. H.; Park, K. M.; Kim, D.; Kim, J. *Chem. Soc. Rev.* **2007**, 36, 267.

[4] Ko, Y. H.; Kim, E.; Hwang, I.; Kim, K. *Chem. Commun.* **2007**, 1305.

[5] Lee, J. W.; Samal, S.; Selvapalam, N.; Kim, H.-J.; Kim, K. *Acc. Chem. Res.* **2003**, 36, 621.

[6] Lagona, J.; Mukhopadhyay, P.; Chakrabarti, S.; Isaacs, L. *Angew. Chem. Int. Ed.* **2005**, 44, 4844.

[7] Nau, W. M. *Nat. Chem.* **2010**, 2, 248.

[8] Bhasikuttan, A. C.; Pal, H.; Mohanty, J. *Chem. Commun.* **2011**, 47, 9959.

[9] Liu, Y.; Yang, H.; Wang, Z.; Zhang, X. *Chem. Asian J.* **2013**, 8, 1626.

[10] Isaacs, L. *Acc. Chem. Res.* **2014**, 47, 2052.

[11] Ma, X.; Zhao, Y. *Chem. Rev.* **2015**, 115, 7794.

[12] Yang, H.; Liu, Y.; Liu, K.; Yang, L.; Wang, Z.; Zhang, X. *Langmuir* **2013**, 29, 12909.

[13] Lin, F.; Zhan, T.-G.; Zhou, T.-Y.; Zhang, K.-D.; Li, G.-Y.; Wu, J.; Zhao, X. *Chem. Commun.* **2014**, 50, 7982.

[14] Ni, X.-L.; Chen, S.; Yang, Y.; Tao, Z. *J. Am. Chem. Soc.* **2016**, 138, 6177.

[15] Zhang, K.-D.; Tian, J.; Hanifi, D.; Zhang, Y.; Sue, A. C.-H.; Zhou, T.-Y.; Zhang, L.; Zhao, X.; Liu, Y.; Li, Z.-T. *J. Am. Chem. Soc.* **2013**, 135, 17913.

[16] Zhang, L.; Zhou, T.-Y.; Tian, J.; Wang, H.; Zhang, D.-W.; Zhao, X.; Liu, Y.; Li, Z.-T. *Polym. Chem.* **2014**, 5, 4715.

[17] Pfeffermann, M.; Dong, R.; Graf, R.; Zajaczkowski, W.; Gorelik, T.; Pisula, W.; Narita, A.; Müllen, K.; Feng, X. *J. Am. Chem. Soc.* **2015**, 137, 14525.

[18] Zhang, X.; Nie, C.-B.; Zhou, T.-Y.; Qi, Q.-Y.; Fu, J.; Wang, X.-Z.; Dai, L.; Chen, Y.; Zhao, X. *Polym. Chem.* **2015**, 6, 1923.

[19] Zhou, T.-Y.; Qi, Q.-Y.; Zhao, Q.-L.; Fu, J.; Liu, Y.; Ma, Z.; Zhao, X. *Polym. Chem.* **2015**, 6, 3018.

[20] Tian, J.; Zhou, T.-Y.; Zhang, S.-C.; Aloni, S.; Altoe, M. V.; Xie, S.-H.; Wang, H.; Zhang, D.-W.; Zhao, X.; Liu, Y.; Li, Z.-T. *Nat. Commun.* **2014**, 5.

[21] Tian, J.; Xu, Z.-Y.; Zhang, D.-W.; Wang, H.; Xie, S.-H.; Xu, D.-W.; Ren, Y.-H.; Wang, H.; Liu, Y.; Li, Z.-T. *Nat. Commun.* **2016**, 7.

[22] An, B.-K.; Kwon, S.-K.; Jung, S.-D.; Park, S. Y. *J. Am. Chem. Soc.* **2002**, 124, 14410.

[23] An, B.-K.; Gierschner, J.; Park, S. Y. *Acc. Chem. Res.* **2011**, 45, 544.

[24] Gierschner, J.; Park, S. Y. *J. Mater. Chem. C* **2013**, 1, 5818.

[25] Kim, H.-J.; Whang, D. R.; Gierschner, J.; Park, S. Y. *Angew. Chem. Int. Ed.* **2016**, 55, 15915.

[26] Ling, Y.; Wang, W.; Kaifer, A. E. *Chem. Commun.* **2007**, 6, 610.

[27] Mohanty, J.; Dutta Choudhury, S.; Upadhyaya, H. P.; Bhasikuttan, A. C.; Pal, H. *Chem. Eur. J.* **2009**, 15, 5215.

[28] Barooah, N.; Mohanty, J.; Bhasikuttan, A. C. *Chem. Commun.* **2015**, 51, 13225.

[29] Langer, P.; Anders, Joachim T. Eur. J. Org. Chem. 2002, 2002, 686.

[30] Ling, Y.; Wang, W.; Kaifer, A. E. *Chem. Commun.* **2007**, 610.

[31] Mohanty, J.; Dutta Choudhury, S.; Upadhyaya, H. P.; Bhasikuttan, A. C.; Pal, H. *Chem. Eur. J.* **2009**, 15, 5215.

[32] Barooah, N.; Mohanty, J.; Bhasikuttan, A. C. *Chem. Commun.* **2015**, 51, 13225.

[33] Wang, F.; Wang, W. G.; Wang, X. J.; Wang, H. Y.; Tung, C. H.; Wu, L. Z. *Angew. Chem. Int. Ed.* **2011**, 50, 3193-3197.

[34] Wang, F.; Liang, W. J.; Jian, J. X.; Li, C. B.; Chen, B.; Tung, C. H.; Wu, L. Z. *Angew. Chem. Int. Ed.* **2013**, 52, 8134-8138.

[35] Wu, L. Z.; Chen, B.; Li, Z. J.; Tung, C. H. *Acc. Chem. Res.* **2014**, 47, 2177-2185.

[36] Wu, P. Y.; Jiang, M.; Li, Y.; Liu, Y. H.; Wang, J. *J. Mater. Chem. A* **2017**, 5, 7833-7838.

Chapter 3.

Self-assembled amphiphilic molecules for highly efficient photocatalytic hydrogen evolution from water

3.1. Introduction

Photocatalytic hydrogen evolution from water has been actively explored as a sustainable and pollution-free clean energy source.[1-8] In particular, platinum decorated metal oxide semiconductors like titanium dioxide have been extensively studied for a long time.[9] However, they still suffer from problems like low compatibility in water and low intrinsic visible light absorption. Therefore, harvesting visible light is the essential demand for photocatalytic systems. In order to increase visible light absorption, wide band-gap metal oxide materials have to use photosensitizers. Recently, Eisenberg could accomplish remarkable hydrogen evolution reaction (HER) performance of platinized TiO_2 nanoparticle through this strategy; turnover number (TON) of 70,000 per photosensitizer for 40 hours.[10] More importantly, they demonstrated the significance of excited state engineering of the metal complex photosensitizer in the hydrogen evolution reaction. In this context, I set my challenge to develop a high HER organic semiconductor system which hopefully outperforms the

metal oxide system by exploiting the diversity of molecular structural design and excited state engineering. Ideal materials for photocatalytic hydrogen evolution should meet the following requirements. They should secure (1) sufficiently long excited state lifetime to satisfy the thermodynamic and kinetic conditions for an efficient photoredox process, and (2) adequate frontier molecular orbital (MO) energies. They should have (3) good compatibility in water, (4) forming nanoparticles with large surface area to provide efficient catalytic activity, and (5) good visible light absorption. Moreover, they should be (6) inexpensive, easy to synthesize and process. So far, there has been no single material that meets all these requirements thoroughly, even though many efforts have been dedicated to find such ideal materials.

Organic semiconductors are principally very good candidates with respect to diversity in design, low cost, good visible light absorption, but improvement is needed for sufficient surface area, excited state lifetime and compatibility in water. Until now, organic photocatalysts such as conjugated polymers[11-15] covalent organic frameworks (COF),[16-18] cucurbit[8]uril based supramolecular organic frameworks (SOF), [19-20] graphitic carbon nitrides (g-CN),[21-23] or non-polymeric photocatalysts[24-25] were mainly reported. Unfortunately, however, their HER performance is far short of the state-of-the-art oxide-based photocatalysts shown above (HER ~ 16.3 mmol/g·h for COF with Pt co-catalyst,[18] TON_{Pt} ~ 300 during 10 hours for SOF with Pt co-catalyst[20]). Among many other reasons for low HER performance in organic/polymeric systems reported so far, I came to notice that the excited state lifetimes have not been appropriately

considered in the design of organic HER photocatalysts. In order to upgrade the performance of small molecule based organic photocatalysts to the state-of-the-art level, I decided to carry out comprehensive studies correlating molecular design to mechanistic studies, particularly focusing on the comprehensive excited state engineering including both singlet and triplet states.

Herein, I devised a novel highly efficient self-assembled amphiphilic molecular system for water splitting in pure water, which is easy to fabricate and flexible enough to control the intrinsic photophysical requirements such as the light absorption and frontier MO levels. The original system I demonstrate in this work consists of ionic organic nanoparticles bearing Pt co-catalyst grown on their surfaces. As a significant result, I demonstrate that this novel photocatalyst system shows a huge increase in HER performance by inducing fast intersystem crossing(ISC) to the triplet excited state. The photoinduced redox process of the system was fully investigated and rationalized by combining ultrafast transient absorption spectroscopy and (time-dependent) density functional theory, (TD)DFT, calculations. For the nano-sized self-assembled molecules of this work incorporating a Pt co-catalyst, impressively high HER rate (400 mmol/g·h) and $TON_{SM1:E}$ of 27,000 (TON_{Pt} ~ 54,000) were recorded in aqueous solution, exhibiting almost comparable performance level with the state-of-the-art metal oxide semiconductor based photocatalysts.[10]

3.2. Experimental Section

Materials:

Molecule **1** was synthesized according to the reported method.[20] Since palladium catalyst was used in its synthetic route, I analyze amount of the metal in the final product through ICP-AES. Not much palladium catalyst was found than detection limit. All other chemicals were purchased from Sigma-Aldrich, Acros and Alfa Aesar, and used without further purification.

Methods – General:

UV-Vis absorption spectra were measured using a Shimazu, UV-1650 PC spectrometer. Dynamic Light Scattering (DLS) measurements were performed on an Otsuka Electronics, DLS-7000. Transmission electron microscope (TEM) images were recorded on a JEOL, JEM-2100F and JEM-3010 and FEI, Tecnai F20. The TEM samples were prepared by dropping a droplet of each aqueous solution on a copper grid and drying in ambient condition. The cyclic voltammetry experiments were conducted using a Princeton Applied Research Potentiostat/Galvanostat Model 273A (Princeton Applied Research) equipped with a three electrode cell assemble including an ITO-coated glass working electrode, a platinum wire counter electrode, and a silver wire quasi-reference electrode. The HOMO level was calculated using the onset oxidation

potential (E_{ox}), and ferrocene ($E_{Fc/Fc+}$) reference was used for calibration. (E_{HOMO} = -[E_{ox} –$E_{Fc/Fc+}$ + 4.8] eV). The LUMO level was calculated from the electrochemically measured HOMO level and the band gap derived from UV-Vis absorption edge. (E_{LUMO} = E_{HOMO} + Eg) ICP-AES was conducted using Perkin-Elmer, OPTIMA 4300DV.

Methods - Hydrogen Evolution Experiment:

All samples were prepared in 13 mL of aqueous solution, and the samples were stirred by a magnetic stirrer. All measurements were conducted at room temperature. A 300W Xe lamp with a 400 nm long pass filter to eliminate ultraviolet light and water jacket to eliminate infrared light was used as a light source. The intensity of the light irradiated at the center of samples was maintained as 300 mW/cm^2. The detailed method for each sample is described below.

A. Self-assembled molecules **1** (**SM1**)

The Sample for photocatalytic hydrogen evolution were prepared by adding 0.65 ml of 1 mM aqueous solution of molecule **1** into 0.97 M 12.35 ml of aqueous solution of L-ascorbic acid. Before mixing pH of ascorbic acid solution was adjusted as 4 by adding 2N NaOH(aq) solution. Total 13 mL of aqueous solution (final molar concentration of ascorbic acid ~ 0.92 M) was added into a 40 mL air-tight vial equipped with a teflon septum. The sample in the light-shielded vial was bubbled for 15 min by Ar with 1% CH_4 as internal standard. Then the vial was irradiated with a 300 W Xe lamp with a

400 nm cutoff filter to eliminate ultraviolet light. The gas (200 μL) in the headspace above the sample was extracted using a Hamilton Lurelock-type syringe then injected into a gas chromatography (Agilent 7890A) equipped with metal packed GC column (60/80 molecular sieve 5A support). The amount of hydrogen evolved was calculated with the integrated area of hydrogen signal calibrated by the integrated area of CH_4 signal.

B. **SM1** with iodide (**SM1/I**)

The measurement was carried out under the same conditions as a (**SM1**) except that sodium iodide was added (0.15 M in final sample).

C. **SM1** without iodide with platinum

The sample was prepared according to the same procedures as a (**SM1**) except that 0.5 ml of 1 mM K_2PtCl_4 aqueous solution was added. Volume of final sample was 13 ml. The sample was added into a 40 mL air-tight vial equipped with a teflon septum. It was continuously purged by 5 sccm of Ar. When TOF was measured every 30 minutes of visible light irradiation, the gas flew into a column of GC for few seconds and the amount of H_2 evolved within the gas during that time was calculated by thermal conductivity detector (TCD). The exact amount of hydrogen was determined by the calibration value which was obtained by measuring calibration gas (0.1 mol% of H_2 in Ar). TOF at t = 0 min was calculated by extrapolating TOF at t = 30 mins and TOF at t = 60 mins. The amount of hydrogen evolved (or TON) vs. time curve was drawn by

integrating the H_2 evolution rate (or TOF) vs. time curve, $TON_{Pt} = n(H_2)/n(Pt)$ or $TON_{\mathbf{1}} = n(H_2)/n(\mathbf{1})$

D. **SM1** with iodide (**SM1/I**) and platinum

The sample was prepared according to the same procedures as B (**SM1** with iodide) except that 0.5 ml of 1 mM K_2PtCl_4 aqueous solution was added. Volume of final sample was 13 ml. For the H_2 evolution measurement, the same method as C was used for this sample.

E. Self-assembled ionic complex (**SM1:E**)

0.65 ml of 1 mM aqueous solution of molecule **1** and 0.65 ml of 1 mM aqueous solution of erythrosine B (**E**) was added into 11.7 ml of ascorbic acid aqueous solution. Final solution has 0.92 M of L-ascorbic acid, 13 ml of volume. Its pH was adjusted as 4. For the H_2 evolution measurement, the same method as A was used for this sample.

F. **SM1:E** with iodide (**SM1:E/I**)

One sample was prepared according to the same procedures as e except that sodium iodide was added (0.15 M in final sample). This sample showed fast HER (13 μmol/g·h) in early stage, but it was saturated soon. The other sample was prepared by adding 0.65 ml of 1 mM aqueous solution of molecule **1** and 0.65 ml of 1 mM aqueous solution of **E** into 11.7 ml aqueous solution which had 1 ml of triethanolamine in it. Before mixing, its pH was adjusted as 7 by adding 1.8 N HCl (aq) solution. The latter sample showed stable activity, and reached to $TON_{\mathbf{1}} \sim 0.5$. For the H_2 evolution measurements, the

same method as A was used for these samples.

G. **SM1:E** without iodide with platinum

The sample was prepared according to the same procedures as E except that 0.5 ml of 1 mM K_2PtCl_4 aqueous solution was added. Volume of final sample was 13 ml. For H_2 evolution measurement, the same method as C was used for this samples.

H. **SM1:E** with iodide (**SM1:E/I**) and platinum

The sample was prepared according to the same procedures as E except that 0.5 ml of 1 mM K_2PtCl_4 aqueous solution and sodium iodide (molar concentration in final solution ~ 0.15 M) was added. Volume of final sample was 13 ml. For H_2 evolution measurement, the same method as C was used for this samples.

Methods – Transient Absorption Spectroscopy. Optical pulses centered at 775 nm were generated from a Ti:sapphire laser (Clark-MXR, CPA2101) driven at 1 kHz repetition rate by a regenerative amplifier, and split into two parts. One fraction was focused on a rotating calcium fluoride plate to obtain a femtosecond white light continuum (320 – 720 nm), which I used as the probe beam. One part of the probe beam was focused onto the sample with a spherical mirror. After passing through the sample, the probe beam was focused onto the slit of a prism spectrometer (Entwicklungsbüro Stresing GmbH), which consisted of a dual channel Charge-coupled Device (CCD) array (2 × 512 pixels, Silicon, Hamamatsu Photonics Inc.). The other part of the probe beam was used as a reference to reduce laser fluctuation

induced noise. The second part of the fundamental 775 nm pulses was sent to a dual stage non-collinear optical parametric amplifier (NOPA, Horiba Jobin Yvon GmbH) operated without compression stage to obtain tunable pump pulses of about 120 fs duration, from 490 – 710 nm, modulated at 500 Hz. Pump and probe beams were focused onto the sample (about 300 and 200 □m spot size, respectively). Intensities of both pump and probe beams were controlled via neutral density filters. The polarization of the pump and probe pulses was at magic angle with respect to each other. Data acquisition and the global and target analysis of transient absorption spectra (for details see below) was done by custom built Python software, using open source libraries (numpy, scipy, pyserial, matplotlib, pyQt, among others).

Methods – Computational Details. Quantum chemistry calculations were performed by (TD)DFT, using the B3LYP functional; the 6-311G* basis set (LANL2DZ basis set for iodide) was utilized in all cases, as defined in the Gaussian program package. All optimizations and single point calculations for the tri-cation of molecule **1** (point group C_3) and the di-anion of Eryothrosin B (**E**; symmetry point group C_s) were carried out in water by employing the polarizable continuum model (PCM). The calculations for **E** included optimizations of S_0, S_1, T_1, D^+_0, D^-_0 where the stability of the open form vs. the close form was compared for all states; single point calculations were done for S_1 and T_1 states at the S_0 geometry, as well as D^+_0 at S_1, D^+_0 at T_1, and S_1 at D^-_0; For **1** it included the geometry optimizations of S_0 and D^-_0, and the single point calculation D^-_0

at S_0.

3.3. Results and Discussion

3.3.1. Self-assembled molecules 1 (SM1)

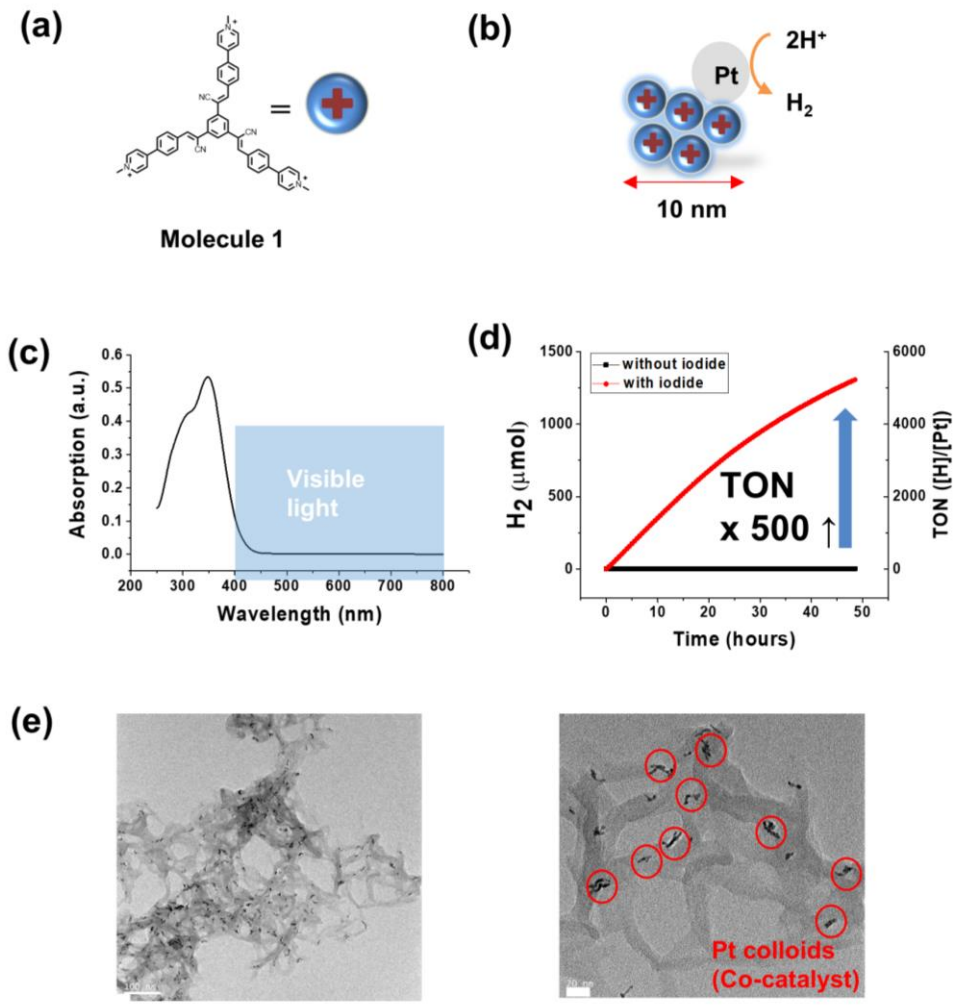

Figure 3-1. Self-assembled molecules 1 (SM1). (a) Molecular structure of 1. (b) Schematic view of SM1. (c) UV-Vis absorption spectrum of SM1 (10 μM aqueous solution of 1). (d) Hydrogen evolution graph of SM1 (prepared from 0.5 μmol of K_2PtCl_4, 0.65 μmol of 1 and 12 mmol of L-ascorbic acid, black: without iodide, red: with 0.15 M of NaI). (e) TEM images of SM1 with external iodide and Pt co-catalyst after 20 hours of photocatalytic reaction. (size of each scale bar is 100 nm, 10 nm respectively).

In the previous work I had demonstrated that the trilateral cationic cyanostilbene structure (molecule **1**; Figure 3-1a) is suitable for HER application in host-guest complexation systems with CB[8] (TON_{Pt} ~ 300 during 10 hours for SOF with Pt co-catalyst).[20] Hence, in the current work, I decided to explore the self-assembled nanostructure of molecule **1** alone in pure water, aiming at improved HER efficiency and stability. It was expected that such an ionic chromophore with well-balanced hydrophobic core should form very stable nano-sized self-assemblies in pure water.[20, 26] Moreover, the charged surface of the nanoparticle was expected to allow complexation with other ionic dyes,[19, 27] providing absorption in the visible range. Finally, I hypothesized that the use of heavy atom counter ions should enhance triplet formation, providing long-lived excited states needed for the photocatalytic cycle.[28-31]

Molecule **1**, synthesized according to the method reported previously,[20] is a trilateral cationic cyanostilbene molecule amphiphilic, bearing hydrophilic pyridinium cationic arms with chloride anions and a hydrophobic core (Figure 3-1a). Due to the delicate

balance of its hydrophobic/-philic moieties it has good water compatibility, and at the same time, it easily forms self-assembled structures of ca. 10 nm sized nanoparticles in aqueous solution[20] (hereafter called SM**1**; see Figure 3-1b). Therefore, SM**1** provides an ideal catalytic reaction site for water splitting hydrogen evolution without any additional bottom-up (polymerization / calcination) or top-down (dispersant treatment / exfoliation) manufacturing processes.

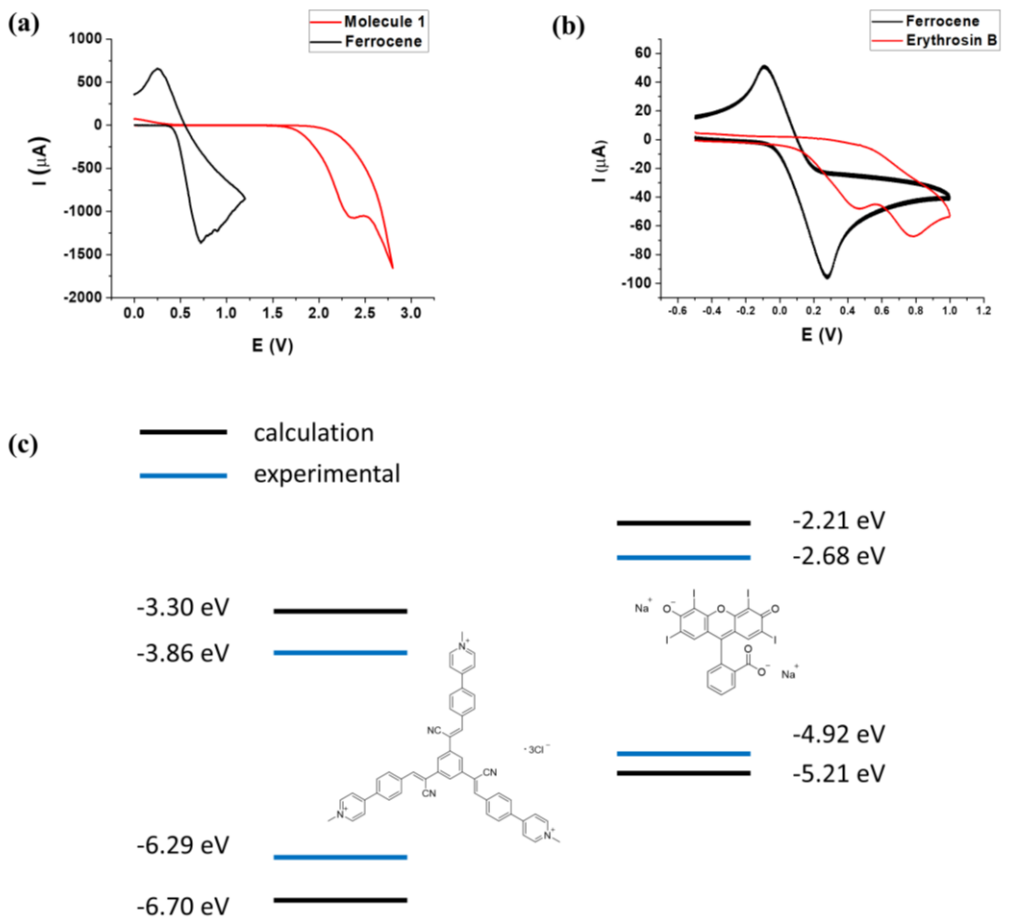

Figure 3-2. Cyclic voltammetry curves of (a) spin coated films on ITO of ferrocene and Molecule **1**, (b) DMF solution of ferrocene and Erythrosin B, and (c) frontier orbital energy levels of Molecule **1** and Erythrosin B

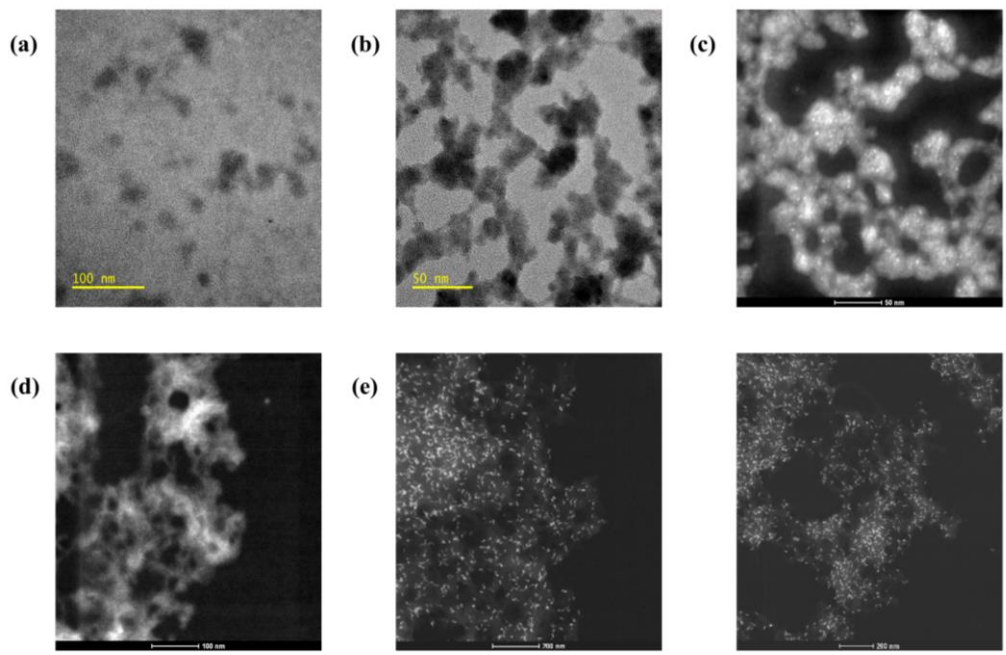

Figure 3-3. TEM images of (a) SM**1** (prepared from 50 μM aqueous solution of **1**) (b) SM1 with iodide (prepared from 0.65 μmol of **1** in 13 mL of 0.15 M of NaI aqueous solution), STEM images of (c) SM**1** with iodide (d) as prepared photocatalytic experimental sample (prepared from 0.5 μmol of K_2PtCl_4, 0.65 μmol of **1** and 12 mmol of L-ascorbic acid in 13 mL of 0.15 M of NaI) (e) after irradiated 24 hours

As a first step, SM**1** alone was tested for visible light driven photocatalytic hydrogen evolution from water, using ascorbic acid as a sacrificial electron donor and a 300W Xenon lamp with a 400 nm long-pass filter as a light source. SM**1** showed an adequate

energy of the lowest unoccupied molecular orbital (LUMO, 3.29 eV, Figure 3-2) for hydrogen evolution. However, the bare system SM**1** (with chloride counter ion) showed no hydrogen evolution. On the other hand, weak hydrogen evolution was observed after sodium iodide addition (TON ~ 0.1 for 12 hours), suggesting an enhanced ISC via external heavy atom effect. To improve its low HER activity and to see clear effect of iodide, I used Pt as a co-catalyst. In practice, it was added as K_2PtCl_4 salt, which was then reduced into metallic Pt during the photocatalytic reaction by photo-reduction. (See Figure 3-3) Nevertheless, even with added Pt co-catalyst, the SM**1** sample without external iodide showed rather poor HER performance (TON ~ 4 in 1 hour). Surprisingly however, upon addition of iodide, the HER was dramatically enhanced. With 0.15 M of external iodide and Pt co-catalyst, the SM**1** photocatalyst (denoted as SM**1**/I) showed a maximum turnover frequency (TOF_{Pt}) of 141 h^{-1} (TOF_{SM1} ~ 108 h^{-1}), TON_{Pt} ~ 2,714 during 20 hours (TON_{SM1} ~ 2,088), eventually reaching TON_{Pt} ~ 4,630 for 40 hours (TON_{SM1} ~ 3,562), see Figure 1d. Despite its limited visible light absorption, SM**1**/I showed very impressive and stable HER over days. To unveil the mechanism of such high HER performance, the nanostructure of the photocatalyst system was studied by TEM; for this, an aqueous solution of ascorbic acid, NaI, K_2PtCl_4 and SM**1** underwent hydrogen evolution under visible light irradiation for 24 hours, and then dried for TEM imaging. As shown in Figure 3-1e, dried and aggregated leaf-shaped organic supramolecular structures of 100~200 nm size were obtained, decorated with 10~20 nm sized rod-shaped Pt colloids grown on

their surface. This indeed proves that SM**1**/I acts as a platform for the co-catalyst growth. The shape of the self-assembled structure of amphiphilic molecule **1** (originally ~10 nm sized nanoparticle) was changed upon addition of other ingredients needed for the photocatalytic cycle. (See Figure 3-3) Most likely, this morphological shift originates from a hydrophobicity change by concentration of salts in aqueous solution, because the solubility of amphiphilic materials relies on their balance between hydrophobicity and hydrophilicity. Moreover, it was frequently reported that addition of salts enhanced aggregation between amphiphilic ionic organic materials.[32-34]

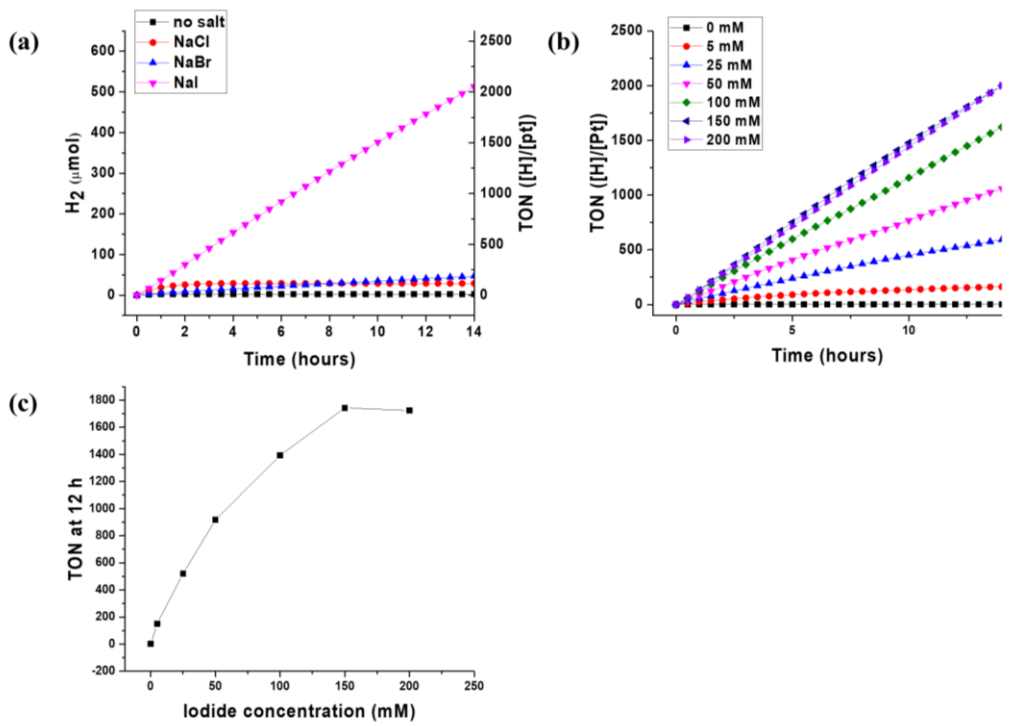

Figure 3-4. Hydrogen evolution curves of photocatalytic systems based on SM**1** (a) with various sodium halides salts (b) with various concentration of NaI (c) TON at 12

hour after irradiation vs. iodide concentration

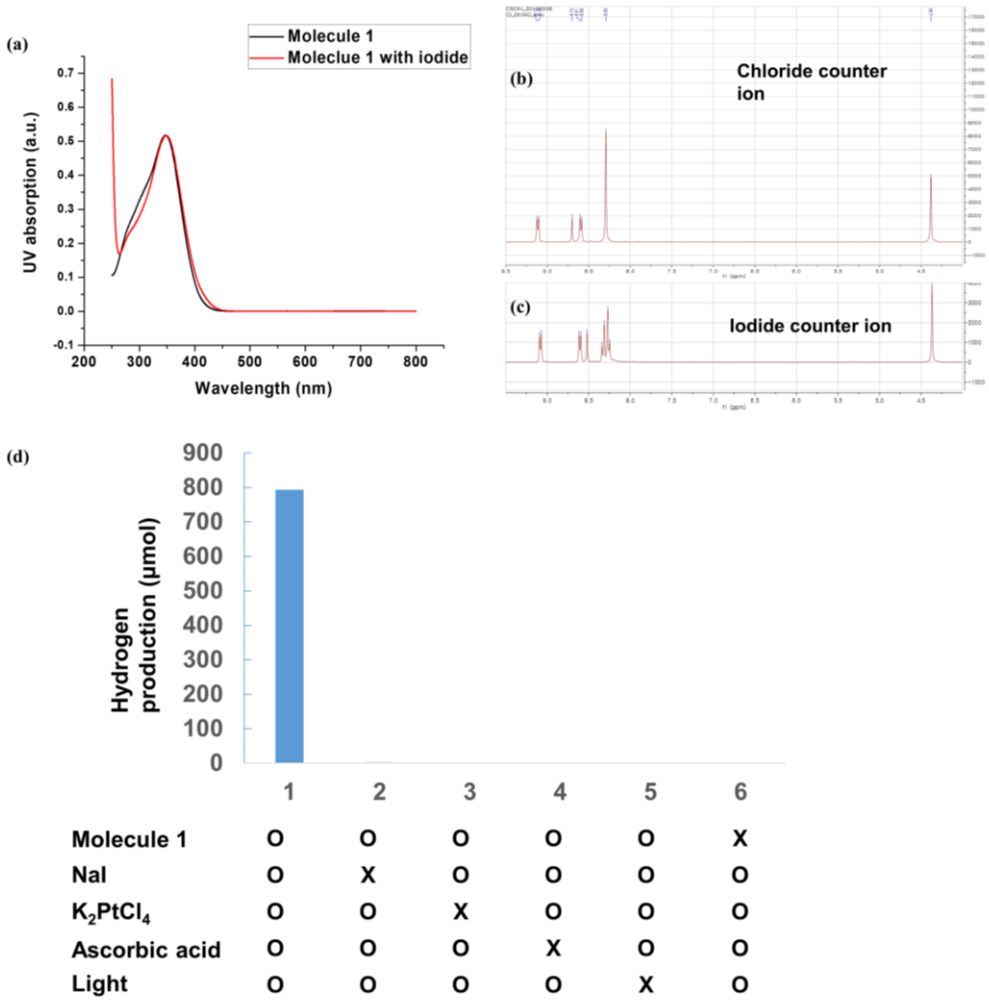

Figure 3-5. (a) UV-Vis absorption curves of 10 μM SM**1** aqueous solution and the sample with/without 30 mM of NaI. NMR spectrum of molecule 1 (b) with chloride counter ion and (c) with iodide counter ion in DMSO. (d) Hydrogen production during 24 hours in various conditions.

Evidently, the role of iodide is crucial for the working principle of my system. It has

been reported[32-34] that addition of various salts resulted in enhanced photocatalytic performance by inducing aggregation. However, in my work, salt addition effect on HER was found to be effective only in the case of the iodide salt but not for chloride and bromide (Figures 3-1d and 3-4), suggesting that the salt-induced aggregation itself is not the reason for the HER enhancement in my case. On the other hand, earlier papers on graphitic carbon nitride photocatalytic systems[35-36] reported a 'redox shuttle' effect showing that the chloride salts could specifically enhance the HER performance by acting as hole scavengers, which is apparently inconsistent with my experimental results. In addition, the iodide-triiodide couple was widely used as electrolyte in dye sensitized solar cells. However, in my case, the characteristic absorption peak of triiodide ions, formed by oxidation of iodide, is missing, ruling out this explanation. I further excluded the formation of a ground state or photoinduced charge transfer complex with iodide as alternative mechanism. This is because I observe no significant spectral change in absorption[37] (figure 3-5a), no pronounced peak shift into upfield or downfield in NMR (figure 3-5b and c), and also no hydrogen production in photocatalytic condition (figure 3-5d) without ascorbic acid even when addition of NaI or counter ion exchange into iodide were made. These considerations all together suggest that a much more specific iodide effect should act on the photophysics of the system.

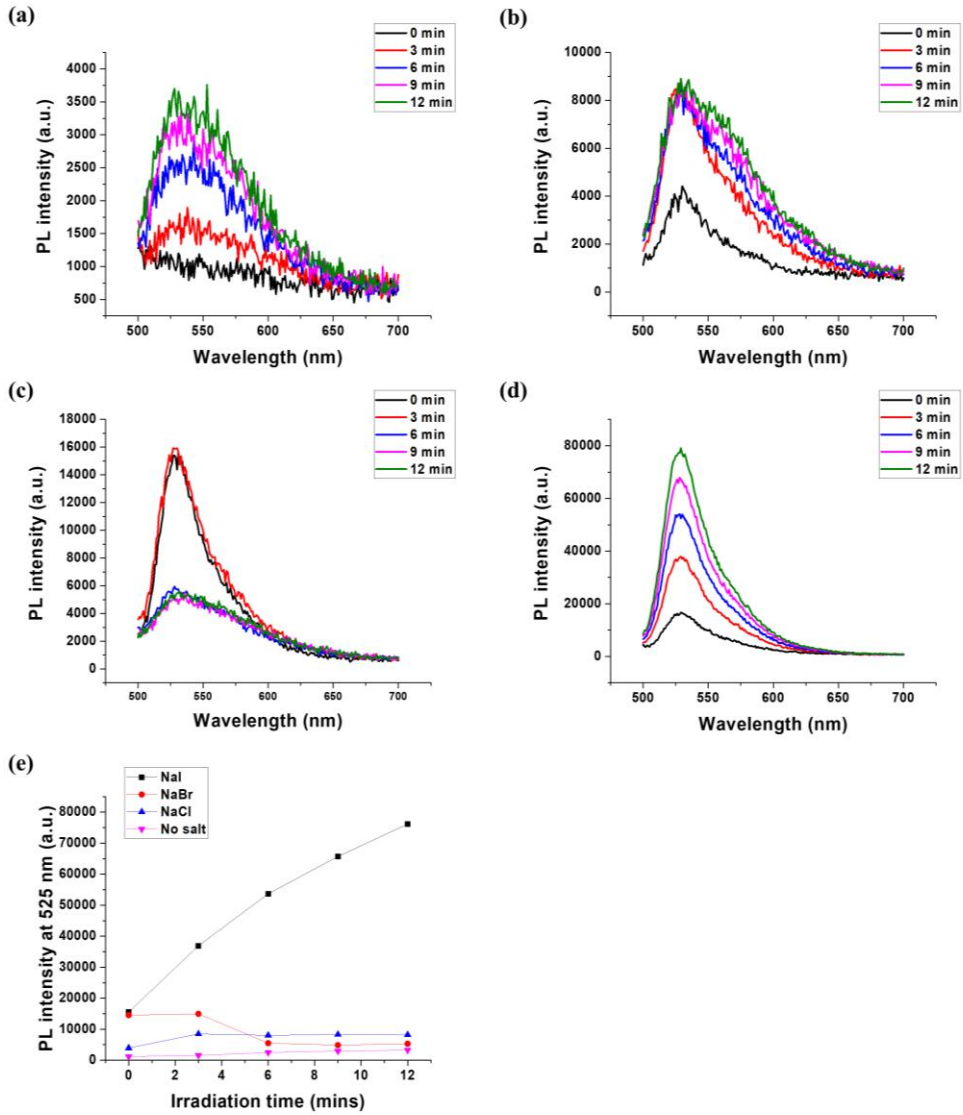

Figure 3-6. Singlet oxygen sensor green (SOSG) experments. PL spectrum change upon 365 nm hand-held UV lamp irradiation of 0.15 micromoles **1** and 0.01 micromoles SOSG in (a) 3 mL aqueous solution (b) 3 mL 0.15 M NaCl aqueous solution (c) 3 mL 0.15 M NaBr aqueous solution (d) 3 mL 0.15 M NaI aqueous solution (e) PL intensity at 525 nm change by 365 nm hand-held UV lamp irradiation

time

I thus suggest that the role of iodide in the present photo-catalytic system is the enhancement of ISC through the heavy atom effect of iodide. To verify this hypothesis, singlet oxygen sensor green (SOSG) was used, a straight forward way to trace singlet oxygen formation via triplet-triplet energy transfer from a dye's triplet excited state of to triplet oxygen.[38-39] As shown in Figure 3-6, only samples incorporating iodide as the most heavy anion exhibited distinct and steady increment of SOSG fluorescence upon 365 nm irradiation, whereas negligible fluorescence change was observed for the bromide and chloride ions. Since iodide is known to quench the generated singlet oxygen to some extent,[40] it should be noted that the actual triplet formation rate is expected to be faster than that measured from the SOSG experiment. As a result, it is evident that the most prominent feature of the sample with iodide is the formation of triplet excited states exhibiting relatively long lifetimes, required for efficient HER performance.

3.3.2. Self-assembled complex molecules (SM1:E)

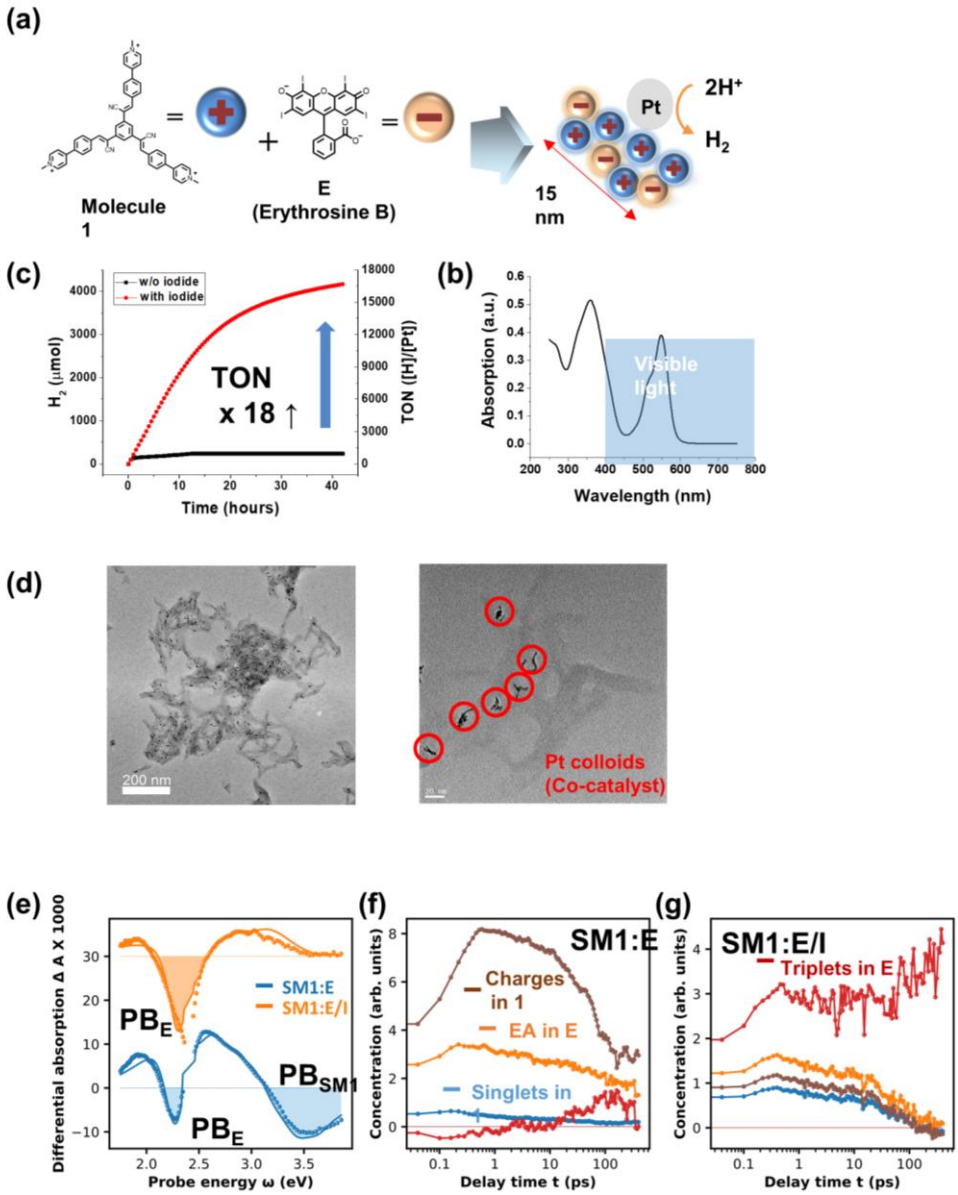

Figure 3-7. Intermolecular ionic complex type self-assembled molecules (SM**1**:**E**). (a)

Schematic view of intermolecular ionic complex for self-assembled organic photocatalyst of the molecule **1** and erythrosine B (E), i.e. SM**1**:**E**. (b) UV-vis absorption spectrum of SM**1**:**E** (10 μM aqueous solution of **1** and **E**). (c) Hydrogen evolution graph of SM**1**:**E** (prepared from 0.5 μmol of K_2PtCl_4, 0.65 μmol of **1**, 0.65 μmol of **E** and 12 mmol of L-ascorbic acid, black: without iodide, red: with 0.15 M of NaI). (d) TEM images of SM**1**:**E** with external iodide and Pt co-catalyst after 20 hours of photocatalytic reaction. (size of each scale bar is 200 nm, 20 nm respectively) (e) Transient absorption (TA) spectra for a pump-probe delay of 10 ps, for SM**1**:**E** without iodide and SM**1**:**E** with 0.15M of NaI (blue, orange, respectively; the latter is noted as SM**1**:**E**/I) and fits from spectral decomposition. The curves are vertically displaced for clarity, with the respective zero indicated as a thin dotted line. Spectral decomposition results in absolute area densities of hot and thermalized singlets in SM**1**, charges in SM**1** and **E**, and triplets in SM**1** and **E**, as given in panels f) and g). The term "EA" in panel f means electroabsorption, here used as a probe for charges.

The most obvious efficiency bottleneck of the SM**1** system discussed above is the lack of optical absorption in the visible spectral region (see Figure 3-1c and 3-7b). Therefore, TOF is expected to increase significantly by tuning the absorption spectrum of the photocatalytic system to better match the solar spectrum. This can be accomplished by bringing a strongly absorbing dye molecule in close contact with the self-assembled system, so as to provide efficient charge transfer. As SM**1** is acidic, it should show strong inter-molecular interactions with basic anions.[19, 27] I thus adopted a xanthene-type commercial dye, erythrosine B (abbreviated as **E** in the following) as the anionic species, having good visible light absorption peaking at 527 nm. Furthermore,

many xanthene type dyes showed good performance as photosensitizers in various photocatalytic systems.[31, 41-44]

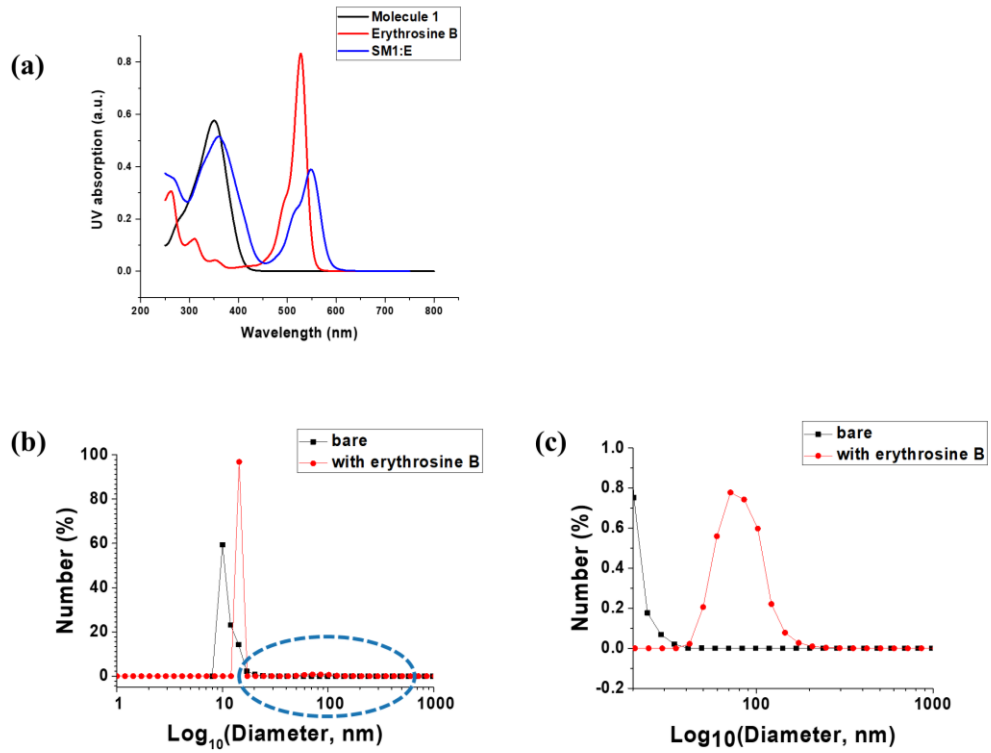

Figure 3-8. (a) UV-Vis absorption spectrum of molecule **1**, erythrosine B and the mixture (SM**1**:E). (Concentration of each molecule in each aqueous solution was 0.01 mM) (b) Dynamic Light Scattering spectrum of molecule **1** (black) and mixture with erythrosine B (red). (c) enlarged spectrum of marked area in (b). (Concentration of each molecule in each aqueous solution was 0.01 mM)

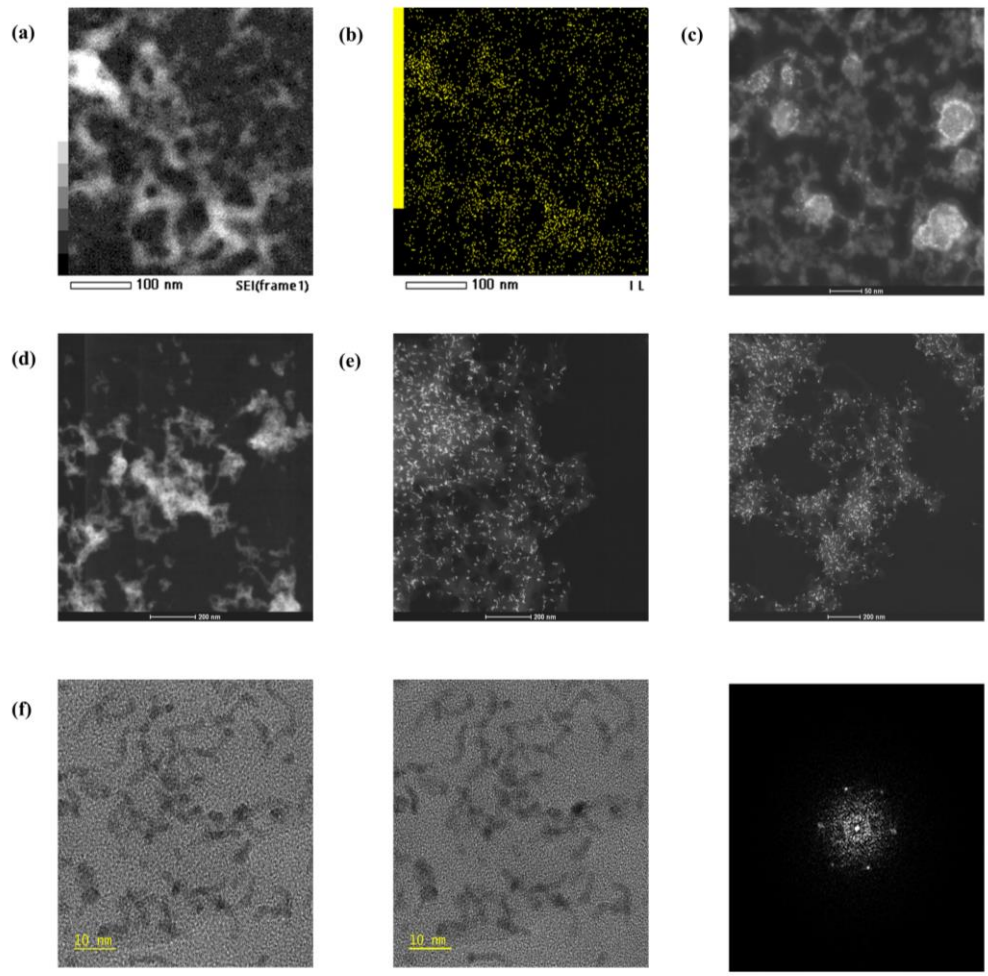

Figure 3-9. STEM images of dried (a) SM**1**:E (prepared from 50 μM aqueous solution of **1** and erythrosine B) (b) EDS mapping of iodide in (a) (c) SM**1**:E with iodide (SM**1**:E in 0.15 M of NaI aqueous solution) (d) as prepared photocatalytic experimental sample (prepared from 0.5 μmol of K_2PtCl_4, 0.65 μmol of **1** and erythrosine B, and 12 mmol of L-ascorbic acid in 13 mL of 0.15 M of NaI) (e) after irradiated 24 hours (f) HRTEM images of dried SM1:E and FFT pattern of a black spot in HRTEM image.

Intimate intermolecular pair formation between **1** and **E** was evaluated by UV-Vis absorption, dynamic light scattering (DLS) and electrophoretic light scattering (ELS) measurements. In the UV-Vis spectrum, the absorption bands of each material were red-shifted (12 nm for **1**, 21 nm for **E**, Figure 3-8a) and decreased upon mixing, indicating the formation of an intermolecular ionic co-assembly. In the DLS and ELS measurement, the average diameter and the zeta potential of self-assembled structures also increased upon addition of **E** (from 11 nm to 17 nm, from +13.09 mV to +38.70 mV, Figure 3-8b and c), confirming the co-assembly (Figure 2a). STEM measurements further proved the good morphological integrity of SM**1**:**E** as an ionic complex (Figure 3-9): it was revealed that erythrosin B was well distributed into SM**1** by mapping iodine through energy dispersive spectrometry (EDS). SM**1**:**E** also showed similar morphological evolution as SM**1** by addition of salts. (Figure 3-7d and 3-9) In addition, 10~15 nm sized rod-shaped Pt colloids were successfully grown onto the organic platforms, as clearly identified in the TEM images.

The presence of the sensitizer (**E**) in SM**1**:**E** drastically increased the HER performance compared to SM**1**, as shown in Figure 3-7c and Figure 3-1d, respectively. In both cases, presence of iodide (SM**1**:**E**/I) and of the Pt co-catalyst are needed to achieve noticeable performance. Interestingly, this trend was observed even without using Pt co-catalyst (TON ~ 0.5 in 12 hours, See details in experimental section). Figure 3-7c shows that the maximum TOF_{Pt} in SM**1**:**E**/I increased by six times (893 h^{-1}, 400 mmol/g·h, $TOF_{SM1:E}$ ~ 687) compared to that of SM**1**/I, and the TON_{Pt} reached

16,500 ($TON_{SM1:E}$ ~ 12,700) in 40 hours by visible light irradiation. This striking enhancement of TOF shows that photocatalyst SM**1**:**E**/I indeed harvests the photon energy very efficiently through the photon antenna **E**. Nevertheless, the crucial role of added iodide to achieve such high TOF numbers had to be understood given the fact that **E** already contains four covalently bonded iodine atoms. In fact, without extra iodide, TOF is reduced by 90% (compare black and red curves in Figure 3-7c), which suggests that intrinsic ISC of **E**, known to proceed within 120 ps in the isolated molecule in water solution,[45] is vastly outperformed under these iodide-free conditions by other competing processes in SM**1**:**E**.

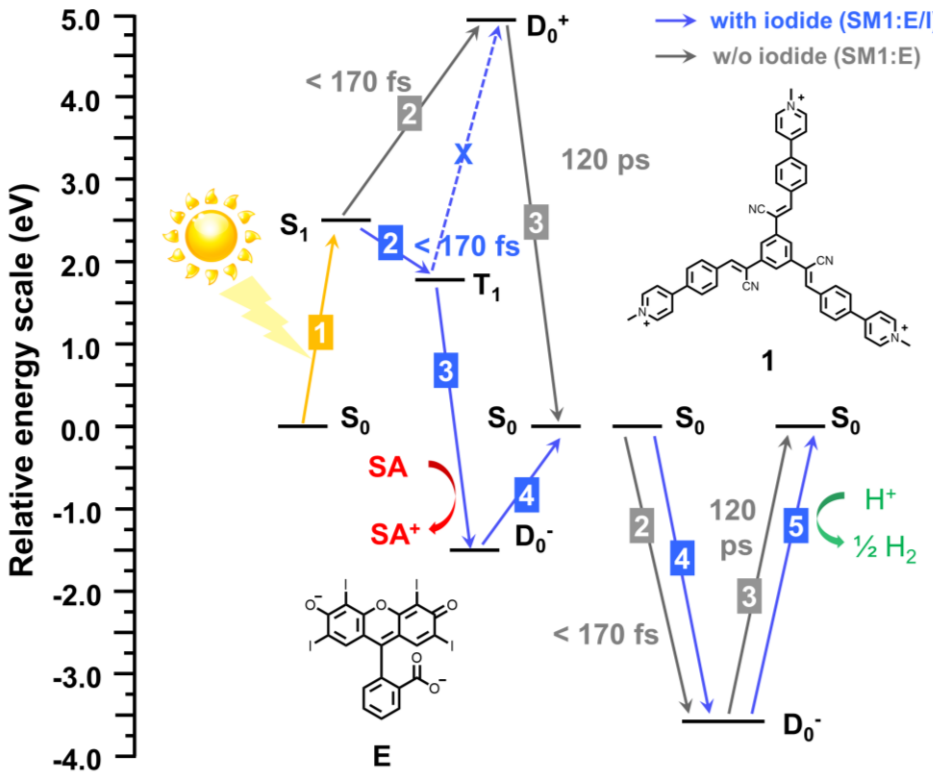

Scheme 3-1. State diagram of the proposed photocatalytic cycle of SM**1**:**E** with and without iodide. Blue arrows with numbers indicate the chronological ordering, undesired loss process are given as grey arrows, time constants are extracted from the TA studies, energy levels from TD-DFT calculations: After singlet light absorption of **E** to the S_1 state (1), and fast relaxation to T_1 in the presence of iodide (2), an electron is injected by sacrificial agent (SA) (3), reducing **E**. The electron is transferred from **E** to **1** (4), followed by the activation of the Pt co-catalyst (5).

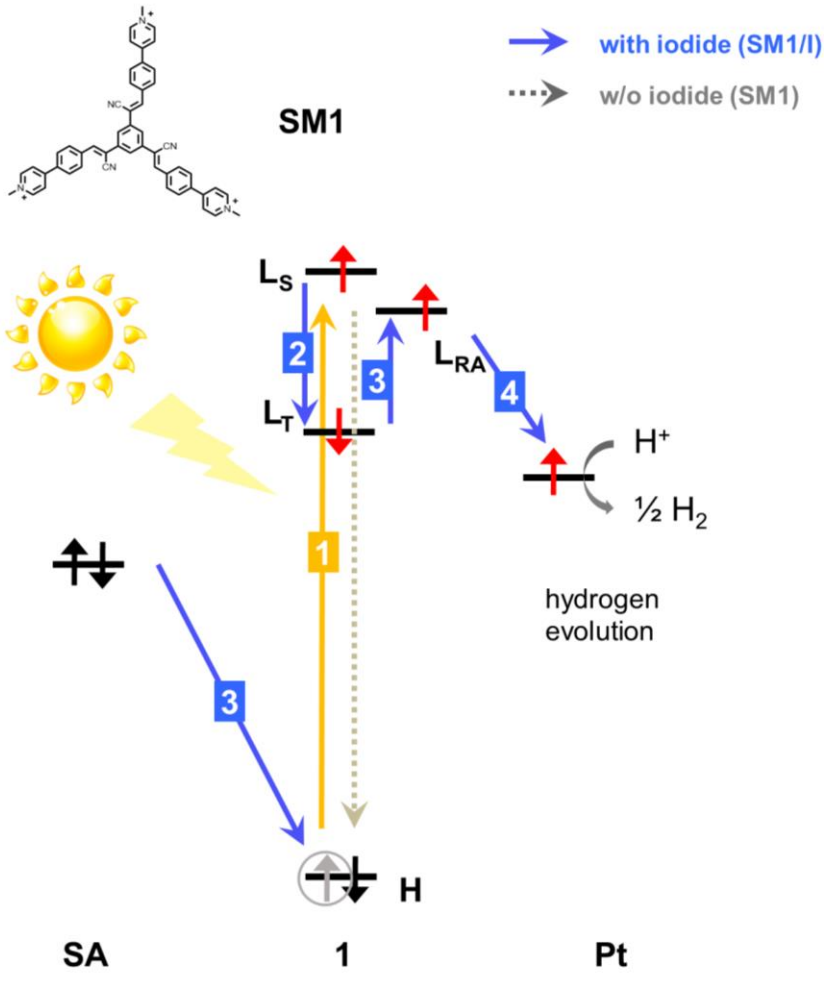

Scheme 3-2. Proposed photocatalytic mechanism of SM**1**.

3.3.2.1 *Photocatalytic Process in the Absence of Iodide.*

Femtosecond TA spectroscopy

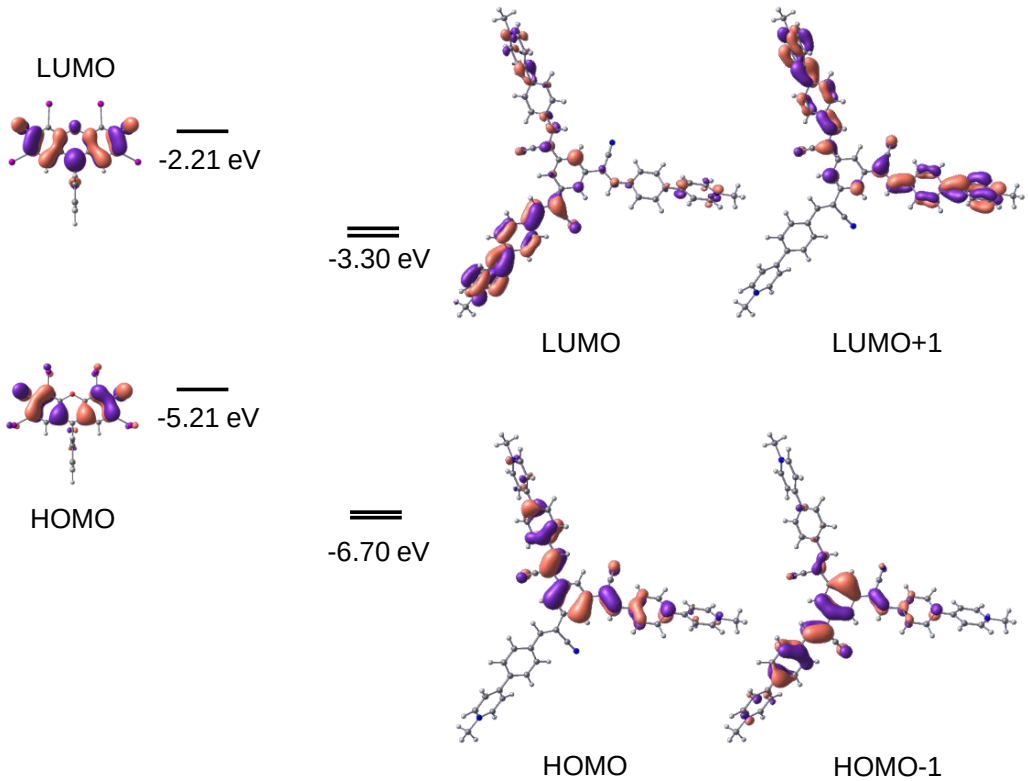

Figure 3-10. Frontier MO energies and topologies of E (left) and 1 (right) in water.

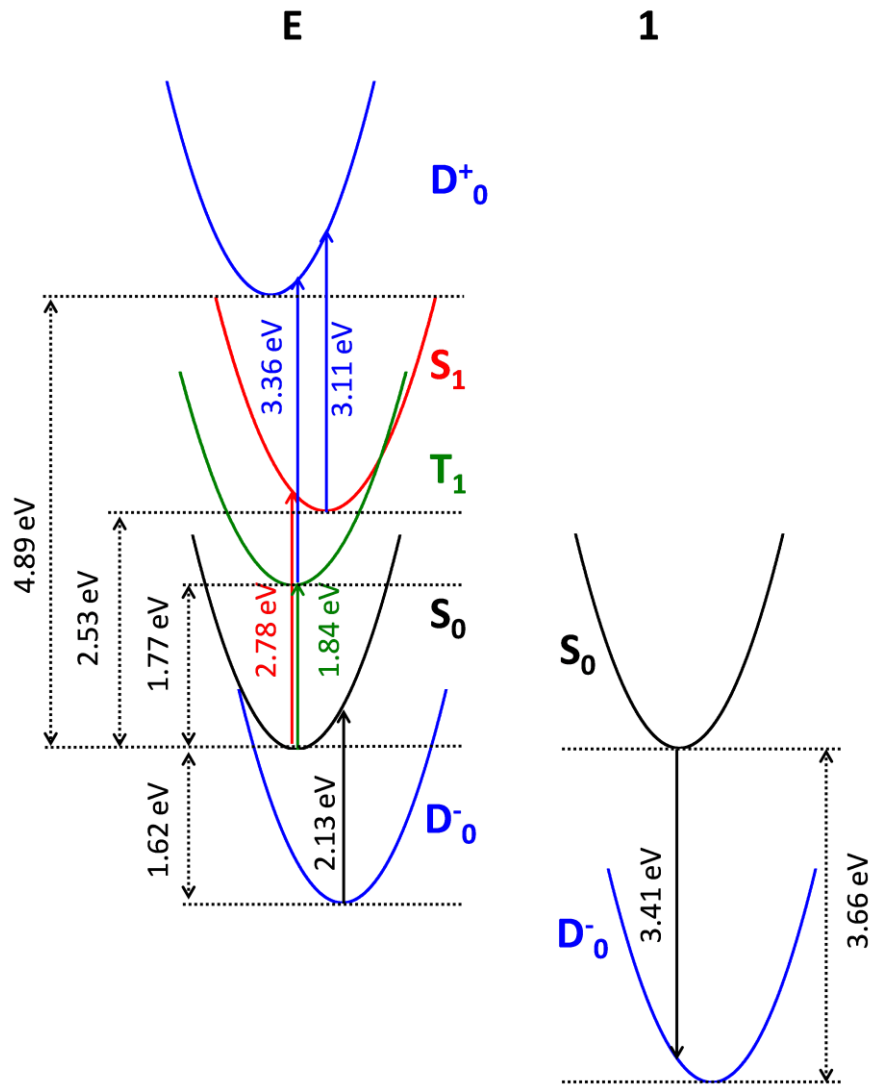

Figure 3-11. Adiabatic and vertical transition energies for states of interest in **E** (left) and **1** (right). (S_0 = singlet ground state, S_1 =first excited singlet state, T_1 = first excited triplet state, D^+_0 = radical cation, D^-_0 = radical anion)

	Erythrosin B	Molecule 1	
SM1/I			
1. Excitation:	$S_0(\mathbf{1}) \rightarrow S_1(\mathbf{1})$		
2. ISC:	$S_1(\mathbf{1}) \rightarrow T_1(\mathbf{1})$		
3. Reduction:	$T_1(\mathbf{1}) \rightarrow D_0^-(\mathbf{1})$		
SM1:E			
1. Excitation:	$S_0(\mathbf{E}) \rightarrow S_1(\mathbf{E})$ 2.53 eV (E_{00})		< fs
2. Charge Sep.:	$S_1(\mathbf{E}) \rightarrow D_0^+(\mathbf{E})$ 2.36 eV (E_{00})	$S_0(\mathbf{1}) \rightarrow D_0^-(\mathbf{1})$ -3.66 eV (E_{00})	170 fs
	3.11eV (E_{vert})	-3.41 eV (E_{vert})	
	large driving force		
3. Charge Rec.:	$D_0^+(\mathbf{E}) \rightarrow S_0(\mathbf{E})$	$D_0^-(\mathbf{1}) \rightarrow S_0(\mathbf{1})$	120 ps
	fast against charge migration to Pt		
SM1:E/I			
1. Excitation:	$S_0(\mathbf{E}) \rightarrow S_1(\mathbf{E})$ 2.53 eV (E_{00})		< fs
2. ISC:	$S_1(\mathbf{E}) \rightarrow T_1(\mathbf{E})$ -0.76 eV (E_{00})		< 170 fs
Charge Sep.:	$T_1(\mathbf{E}) \rightarrow D_0^+(\mathbf{E})$ 3.12 eV (E_{00})	$S_0(\mathbf{1}) \rightarrow D_0^-(\mathbf{1})$ -3.66 eV (E_{00})	(slow)
	3.36 eV (E_{vert})	-3.41 eV (E_{vert})	
	small driving force		
3. Red. by SE:	$T_1(\mathbf{E}) \rightarrow D_0^-(\mathbf{E})$ -3.39 eV (E_{00})		slow
4. Redox:	$D_0^-(\mathbf{E}) \rightarrow S_0(\mathbf{E})$ 1.62 eV (E_{00})	$S_0(\mathbf{1}) \rightarrow D_0^-(\mathbf{1})$ -3.66 eV (E_{00})	
	2.13 eV (E_{vert})	-3.41 eV (E_{vert})	
	large driving force		
5. Ox. (H_2 evolu.):		$D_0^-(\mathbf{1}) \rightarrow S_0(\mathbf{1})$ 3.66 eV (E_{00})	
	large driving force		

Figure 3-12. Equations for all steps of the photocatalytic processes. (S_0 = singlet ground state, S_1 =first excited singlet state, T_1 = first excited triplet state, D^+_0 = radical cation, D^-_0 = radical anion)

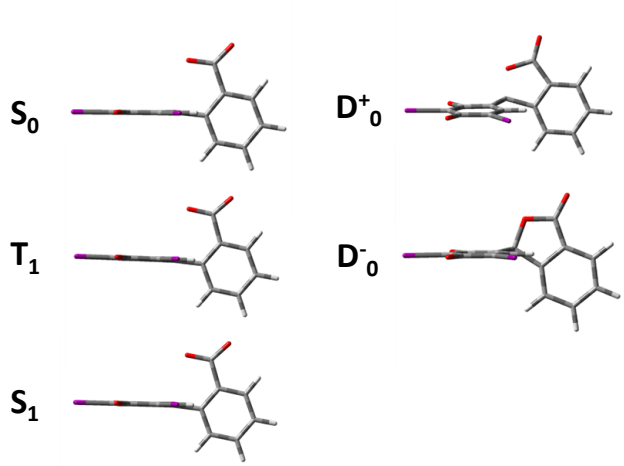

Figure 3-13. Results of the geometry optimizations (in water) for E in the different neutral and charged electronic states.

revealed the nature of this competing process in the absence of added iodide in SM**1**:**E**. After singlet states are created selectively on **E** under 532 nm excitation (step 1; see Scheme 3-1), they are dissociated quantitatively into charge separated states (CS) within less than 170 fs (step 2; grey arrow in Scheme 3-1), as evidenced by the observation of transient photobleach (PB, blue shaded areas in Figure 3-7e) of both **E** and SM**1** already during the pump pulse duration. According to the TD-DFT calculations (see Scheme 3-1), charge separation is energetically favored by a substantial energetic driving force; in fact, the energy required to oxidize **E** is 3.11 eV, while the energy released by the reduction of **1** is 3.41 eV, Figure 3-12. The ultrafast formation of the CS is in agreement with many literature reports describing ultrafast exciton dissociation in intimately mixed electron donors and acceptors.[46-47]

Energetically (see Scheme 3-1), the resulting reduced **1** could in principle transfer the excess electron to the Pt nanoparticles and produce hydrogen. However, charge recombination towards the electronic ground state may occur as an efficient competitive pathway. My TA analysis shows that this back electron transfer (step 3) indeed occurs in around 120 ps (brown and orange curves in Figure 3-7f), thereby outperforming charge migration towards the Pt nanoparticles, which is expected to be the slowest process virtually.[48] In spite of the extremely fast CS formation, small amounts of long-lived triplet states (red curve in Figure 3-7f) were observed, explaining the small but distinct level of hydrogen evolution ($TOF_{SM1:E} \sim 52$, $TON_{SM1:E} \sim 952$), even when no iodide is added.

3.3.2.2 *Photocatalytic Process in the Presence of Iodide.*

In the presence of iodide (denoted as SM**1**:**E**/I), a drastically different scenario is observed, as summarized in Scheme 3-1. After specific excitation of **E** (step 1 in Scheme 3-1), I mainly find ultrafast formation of the triplet state on **E** within less than 170 fs (step 2; blue arrow) as evidenced by its known spectral shape (orange curve in Figure 3-7e, for details see experimental section); I assign this to a strong external heavy atom effect which significantly enhances the ISC process by the excess iodide. [†] Only a small contribution of ultrafast charge generation is observed (compare the red

curve with the orange and brown curves in Figure 3-7g, respectively). The charge recombination, occurring at 120 ps time scale, further enhances the triplet concentration. The apparent reason for the strong reduction in charge generation is the stabilization of the system through efficient triplet generation, so that the energy for the formation of oxidized **E** is getting too high (3.36 eV according to TD-DFT); see Scheme 3-1 and Figure 3-12). Therefore, the triplets are stable for approximately 1 microsecond, more than sufficient to allow diffusion-limited reduction by the sacrificial agent (SA; step 3). The excess charge is then transferred to molecule **1** without competing processes (step 4). As there is no relaxation path for SM**1**:**E**/I in the presence of iodide, the final step, i.e. electron transfer to Pt (step 5), will proceed without parasitic processes. Therefore, the high TOF numbers observed in SM**1**:**E**/I, are shown to derive from ultrafast and highly efficient generation of long-lived triplet states; on the other hand, in the absence of iodide, ultrafast formation of charge separated states is observed, which do not have sufficient lifetime to be reduced by the sacrificial agent.

Figure 3-14. Pictures of photocatalytic systems under visible light irradiation. (a) Sample without molecule **1** (prepared from 0.5 μmol of K_2PtCl_4, 0.65 μmol of Erythrosine B and 12 mmol of L-ascorbic acid with 0.15 M of NaI in 13 mL of distilled water) after 10 minutes of visible light irradiation. Because erythrosine radical anion is very unstable upon visible light irradiation, the sample was turned to be white. (b) Sample with molecule **1**, SM**1**:**E**/I (prepared from 0.5 μmol of K_2PtCl_4, 0.65 μmol of Erythrosine B and Molecule **1**, 12 mmol of L-ascorbic acid with 0.15 M of NaI in 13 mL of distilled water) after 10 hours of visible light irradiation.

Apart from enhancing TOF, also the maximum achievable TON must be enhanced to bring photocatalysis closer to the market. I have found that iodide enhances both TOF and TON, which means that a system showing high efficiency also has a longer operational lifetime. In order to identify the stability bottleneck, I performed a control experiment; i.e. trying to produce hydrogen with **E** alone. In fact, only trace amounts of hydrogen were produced and the system was shown to be very unstable under the same reaction conditions. This agrees with earlier reports on the unstable character of the

reduced **E**.[31] (See Figure 3-14) On the other hand, SM**1**:**E**/I was much more stable: even after 24 hours of visible light irradiation, it maintained its original color and good HER performance. I ascribe this to the fast electron transfer from the reduced **E** to **1**, which is enabled by the specific electronic structure of the SM**1**:**E**/I system.

3.3.3. Optimization of the HER process

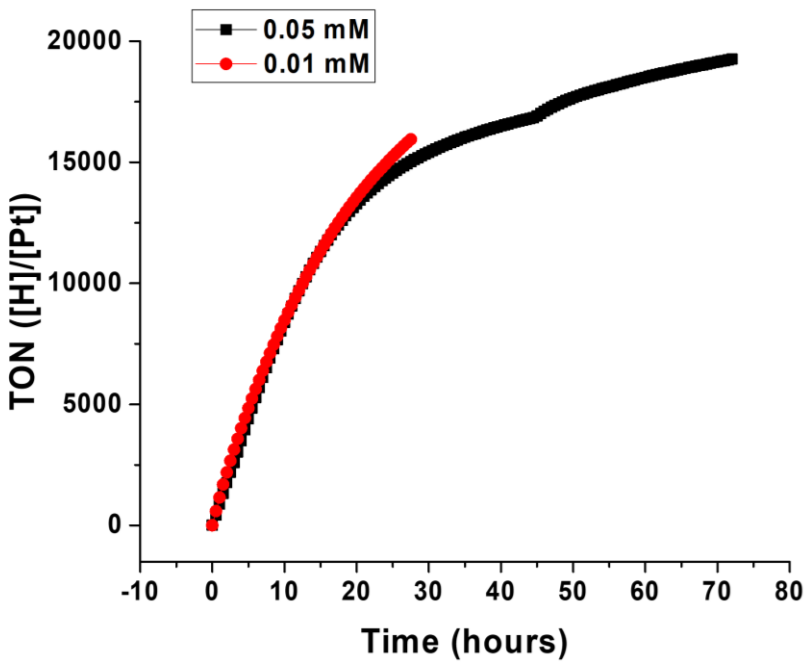

Figure 3-15. Hydrogen evolution curves of SM**1**:**E**/I with various concentration. 0.01 mM of molecule **1** (red) and 0.05 mM of molecule **1** (black) (Other additives were also changed in proportion).

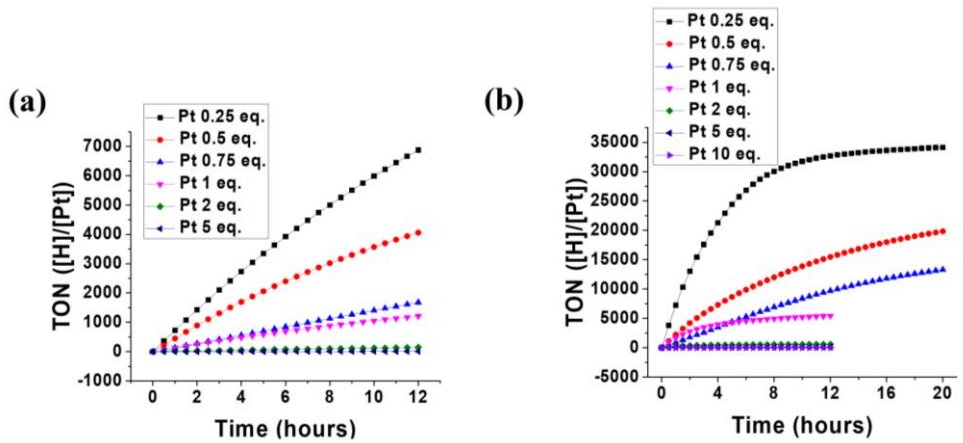

Figure 3-16. Turnover number of (a) SM**1**/I and (b) SM**1**:**E**/I with various amounts of platinum. **(**Each legend shows the equivalent of platinum to molecule **1**)

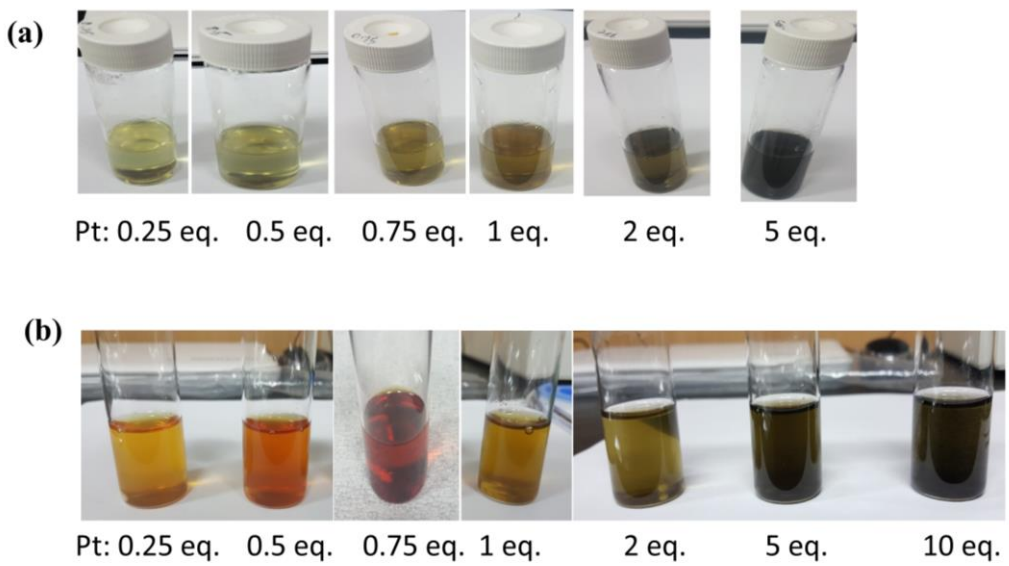

Figure 3-17. Pictures of (a) SM**1**/**E** and (b) SM**1**:**E**/I with various amounts of platinum after 24 hours of visible light irradiation. (The numbers under each picture show the equivalent of platinum to molecule **1**.)

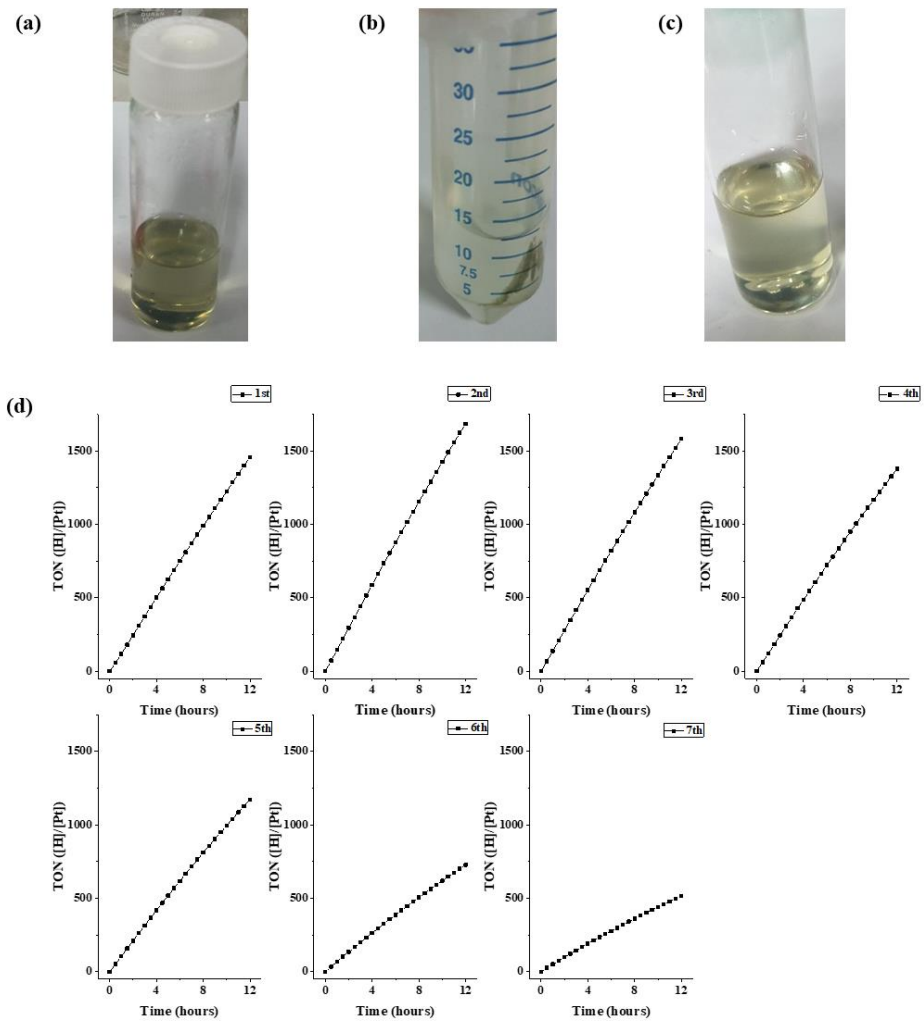

Figure 3-18. Pictures of the SM**1**/I solution and hydrogen evolution curves. Pictures of (a) After 12 hours hydrogen evolution reaction. (b) Centrifuged (8000 rpm, 20 mins) sample in A. (c) Re-distiributed in fresh 13 mL of aqueous solution of 0.15 M NaI and 0.92M L-ascorbic acid (d) Hydrogen evolution curves 7 cycles (12 hour for each cycle).

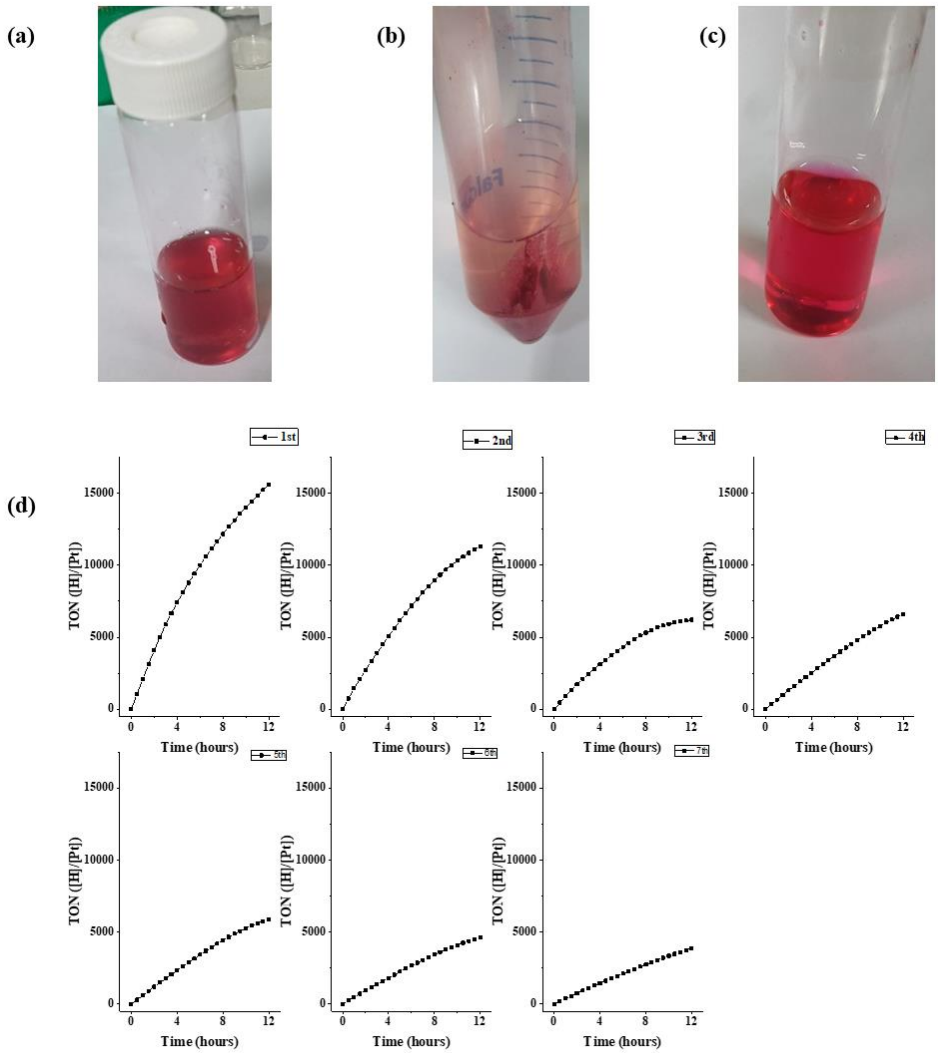

Figure 3-19. Pictures of the SM**1**:**E**/I solution and hydrogen evolution curves. Pictures of (a) After 12 hours hydrogen evolution reaction. (b) Centrifuged (8000 rpm, 20 mins) sample in (a). (c) Re-distiributed sample in fresh 13 mL of aqueous solution of 0.15 M NaI and 0.92 M L-ascorbic acid (d) Hydrogen evolution curves 7 cycles (12 hours for each cycle).

For a better evaluation of photocatalyst materials, reporting optimized HER rate is most important.[49] To find optimized conditions, I varied the concentration of both molecule **1** and Pt. Regarding the concentration of molecule **1**, I found that 0.01 mM sample showed almost the same TOF and TON with 0.05 mM sample. (Figure 3-15) Concerning the co-catalyst, I evaluated samples with various amounts of Pt, to define the optimum amount. Increasing equivalent of Pt vs. **1** to more than one, the amount of hydrogen production started to decrease. This is ascribed to the increase of light scattering which hinders the photocatalytic reaction (See Figure 3-16 and 3-17). When 0.25 equivalent of Pt to **1** was used, TON_{Pt} could reach 30,000 in 8 hours, but HER was saturated soon. TON_{Pt} and $TON_{SM1:E}$ were optimum when 0.5 equivalent of Pt to **1** was used. TON_{Pt} was as high as 20,000 and that of SM**1**:**E**/I 10,000 in 20 hours under visible light irradiation. With this optimum composition, I carried out cycle experiments to confirm its maximum TON. Ascorbic acid is known to turn into dehydroascorbic acid (DHA) during photochemical reaction cycle, which detrimentally oxidize the reduced species of the photocatalyst before the hydrogen evolution reaction.[10, 50] Therefore, in order to maintain the activity of the photocatalyst, it is necessary to remove DHA. SM**1**:**E** was separated from aqueous solution of DHA, ascorbic acid and NaI by high speed centrifugation every 12 hours during the hydrogen evolution reaction. Then it was re-distributed in freshly prepared aqueous solution of ascorbic acid and NaI. Since all electrostatically bonded **E** was not withdrawn, an additional half amount of it was added in every cycle. During 7 cycles (84 hours),

TON_{Pt} reached to 54,000 ($TON_{\mathbf{1}}$ ~ 27,000, Figure 3-19) while the photocatalytic activity was stable. This is comparable with the performance of the recently reported high-performance titanium dioxide based photocatalyst ($TON_{photosensitizer}$ ~ 70,000).[10] The apparent quantum yield of hydrogen evolution for SM**1**:**E** with Pt co-catalyst was also measured as 6.5 % using a 550 nm band-pass filter.

3.4. Conclusion

In summary, I developed the self-assembled molecular system SM**1**:**E**/I consisting of amphiphilic molecule **1** for visible light driven photocatalytic hydrogen evolution from water. The self-assembled structures were suitable as a photocatalytic water splitting platform because of their large surface area and good water compatibility. Using their cationic nature, intermolecular ionic complexes with an anionic commercial dye (**E**) and iodide (I) were easily made to give SM**1**:**E**/I; this was shown to be essential for the high catalytic activity of the supramolecular system. Combined ultrafast transient absorption and computational studies revealed electron transfer rates and processes in the supramolecular assembly, where iodide promotes highly efficient triplet generation of **E** and thus a long excited state lifetime, so that excited **E** provides enough time to receive an electron from sacrificial reagent, while suppressing charge recombination with **1**; this allowed for an effective catalytic process control in the system. As a result,

my non-polymeric system consisting of self-assembled molecules with Pt co-catalyst was as efficient as the conventional metal-complex dye decorated inorganic semiconductors, without polymerization, calcining, anchoring, or any other complex fabrication process. Remarkably, my SM**1**:**E**/I system is reactive over days, and the recorded TON per SM**1**:**E**/I is as high as 27,000 and 54,000 per Pt co-catalyst.

3.5. Note

‡ "I cannot conclusively demonstrate the elementary mechanism for ultrafast iodide induced triplet formation because the instrumental time resolution of my TA system is 170 fs. However, considering the concurrence of ultrafast charge generation and triplet generation, as evidenced in Figure 2g, the assumption of a common precursor for both processes seems plausible."

3.6. References

[1] Graetzel, M. *Acc. Chem. Res.* **1981,** *14*, 376-384.

[2] Faunce, T. A.; Lubitz, W.; Rutherford, A. W.; MacFarlane, D.; Moore, G. F.; Yang, P.; Nocera, D. G.; Moore, T. A.; Gregory, D. H.; Fukuzumi, S.; et al. *Energy Environ. Sci.* **2013,** *6*, 695-698.

[3] Yuan, L.; Han, C.; Yang, M.-Q.; Xu, Y.-J. *Int. Rev. Phys. Chem.* **2016,** *35*, 1-36.

[4] Zhang, N.; Qi, M.-Y.; Yuan, L.; Fu, X.; Tang, Z.-R.; Gong, J.; Xu, Y.-J. *Angew. Chem. Int. Ed.* **2019,** *58*, 10003-10007.

[5] Li, S.-H.; Zhang, N.; Xie, X.; Luque, R.; Xu, Y.-J. *Angew. Chem. Int. Ed.* **2018,** *57*, 13082-13085.

[6] Yang, M.-Q.; Han, C.; Xu, Y.-J. *J. Phys. Chem. C* **2015,** *119*, 27234-27246.

[7] Suen, N.-T.; Hung, S.-F.; Quan, Q.; Zhang, N.; Xu, Y.-J.; Chen, H. M. *Chem. Soc. Rev.* **2017,** *46*, 337-365.

[8] McKone, J. R.; Lewis, N. S.; Gray, H. B. *Chem. Mater.* **2014,** *26*, 407-414.

[9] Zhang, X.; Peng, T.; Song, S. *J. Mater. Chem. A* **2016,** *4*, 2365-2402.

[10] Li, G.; Mark, M. F.; Lv, H.; McCamant, D. W.; Eisenberg, R. *J. Am. Chem. Soc.* **2018,** *140*, 2575-2586.

[11] Sprick, R. S.; Bonillo, B.; Clowes, R.; Guiglion, P.; Brownbill, N. J.; Slater, B. J.; Blanc, F.; Zwijnenburg, M. A.; Adams, D. J.; Cooper, A. I. *Angew. Chem. Int. Ed.* **2016,** *55*, 1792-1796.

[12] Wang, L.; Fernández-Terán, R.; Zhang, L.; Fernandes, D. L. A.; Tian, L.; Chen, H.; Tian, H. *Angew. Chem. Int. Ed.* **2016,** *55*, 12306-12310.

[13] Zhang, G.; Lan, Z.-A.; Wang, X. *Angew. Chem. Int. Ed.* **2016,** *55*, 15712-15727.

[14] Pati, P. B.; Damas, G.; Tian, L.; Fernandes, D. L. A.; Zhang, L.; Pehlivan, I. B.; Edvinsson, T.; Araujo, C. M.; Tian, H. *Energy Environ. Sci.* **2017,** *10*, 1372-1376.

[15] Woods, D. J.; Sprick, R. S.; Smith, C. L.; Cowan, A. J.; Cooper, A. I. *Adv. Energy Mater.* **2017,** *7*, 1700479.

[16] Jiang, X.; Wang, P.; Zhao, J. *J. Mater. Chem. A* **2015,** *3*, 7750-7758.

[17] Vyas, V. S.; Haase, F.; Stegbauer, L.; Savasci, G.; Podjaski, F.; Ochsenfeld, C.; Lotsch, B. V. *Nat. Commun.* **2015,** *6*, 8508.

[18] Wang, X.; Chen, L.; Chong, S. Y.; Little, M. A.; Wu, Y.; Zhu, W.-H.; Clowes, R.; Yan, Y.; Zwijnenburg, M. A.; Sprick, R. S.; Cooper, A. I. *Nat. Chem.* **2018,** *10*, 1180-1189.

[19] Tian, J.; Xu, Z. Y.; Zhang, D. W.; Wang, H.; Xie, S. H.; Xu, D. W.; Ren, Y. H.; Wang, H.; Liu, Y.; Li, Z. T. *Nat. Commun.* **2016,** *7*, 11580.

[20] Lee, H.-J.; Kim, H.-J.; Lee, E.-C.; Kim, J.; Park, S. Y. *Chem. Asian J.* **2018,** *13*, 390-394.

[21] Wang, X.; Maeda, K.; Thomas, A.; Takanabe, K.; Xin, G.; Carlsson, J. M.; Domen, K.; Antonietti, M. *Nat. Mater.* **2009,** *8*, 76-80.

[22] Cao, S.; Low, J.; Yu, J.; Jaroniec, M. *Adv. Mater.* **2015,** *27*, 2150-2176.

[23] Liu, J.; Liu, Y.; Liu, N.; Han, Y.; Zhang, X.; Huang, H.; Lifshitz, Y.; Lee, S.-T.; Zhong, J.; Kang, Z. *Science* **2015,** *347*, 970-974.

[24] Wang, R.; Li, G.; Zhang, A.; Wang, W.; Cui, G.; Zhao, J.; Shi, Z.; Tang, B. *Chem. Commun.* **2017,** *53*, 6918-6921.

[25] Nath, K.; Chandra, M.; Pradhan, D.; Biradha, K. *ACS Appl. Mater. Interfaces* **2018,** *10*, 29417-29424.

[26] Lee, E.-C.; Kim, H.-J.; Park, S. Y. *Chem. Asian J.* **2019,** *14*, 1457-1461.

[27] Tian, J.; Zhou, T. Y.; Zhang, S. C.; Aloni, S.; Altoe, M. V.; Xie, S. H.; Wang, H.;

Zhang, D. W.; Zhao, X.; Liu, Y.; et al. *Nat. Commun.* **2014,** *5*, 5574.

[28] Juris, A.; Balzani, V.; Barigelletti, F.; Campagna, S.; Belser, P.; von Zelewsky, A. *Coord. Chem. Rev.* **1988,** *84*, 85-277.

[29] Lu, J.; Pattengale, B.; Liu, Q.; Yang, S.; Shi, W.; Li, S.; Huang, J.; Zhang, J. *J. Am. Chem. Soc.* **2018,** *140*, 13719-13725.

[30] Larsen, C. B.; Wenger, O. S. *Chem. Eur. J.* **2018,** *24*, 2039-2058.

[31] Shimidzu, T.; Iyoda, T.; Koide, Y. *J. Am. Chem. Soc.* **1985,** *107*, 35-41.

[32] Yang, X.; Hu, Z.; Yin, Q.; Shu, C.; Jiang, X.-F.; Zhang, J.; Wang, X.; Jiang, J.-X.; Huang, F.; Cao, Y. *Adv. Funct. Mater.* **2019***, 29*, 1808156.

[33] Weingarten, A. S.; Kazantsev, R. V.; Palmer, L. C.; McClendon, M.; Koltonow, A. R.; SamuelAmanda, P. S.; Kiebala, D. J.; Wasielewski, M. R.; Stupp, S. I. *Nat. Chem.* **2014,** *6*, 964-970.

[34] Weingarten, A. S.; Kazantsev, R. V.; Palmer, L. C.; Fairfield, D. J.; Koltonow, A. R.; Stupp, S. I. *J. Am. Chem. Soc.* **2015,** *137*, 15241-15246.

[35] Li, J.-X.; Ye, C.; Li, X.-B.; Li, Z.-J.; Gao, X.-W.; Chen, B.; Tung, C.-H.; Wu, L.-Z. *Adv. Mater.* **2017,** *29*, 1606009.

[36] Zhang, G.; Li, G.; Lan, Z. A.; Lin, L.; Savateev, A.; Heil, T.; Zafeiratos, S.; Wang, X.; Antonietti, M. *Angew. Chem. Int. Ed.* **2017,** *56*, 13445-13449.

[37] Ebbesen, T.; Ferraudi, G. *J. Phys. Chem.* **1983,** *87*, 3717-3721.

[38] Flors, C.; Fryer, M. J.; Waring, J.; Reeder, B.; Bechtold, U.; Mullineaux, P. M.; Nonell, S.; Wilson, M. T.; Baker, N. R. *J. Exp. Bot.* **2006,** *57*, 1725-1734.

[39] Prasad, A.; Sedlářová, M.; Pospíšil, P. *Sci. Rep.* **2018,** *8*, 13685.

[40] Wen, X.; Zhang, X.; Szewczyk, G.; El-Hussein, A.; Huang, Y.-Y.; Sarna, T.; Hamblin, M. R. *Antimicrob. Agents Chemother.* **2017,** *61*, e00467-17.

[41] Lambert, C. R.; Kochevar, I. E. *Photochem. Photobiol.* **1997,** *66*, 15-25.

[42] Abe, R.; Hara, K.; Sayama, K.; Domen, K.; Arakawa, H. *J. Photochem. Photobiol. A* **2000,** *137*, 63-69.

[43] Islam, S. D. M.; Konishi, T.; Fujitsuka, M.; Ito, O.; Nakamura, Y.; Usui, Y. *Photochem. Photobiol.* **2000,** *71*, 675-680.

[44] Jin, Z.; Zhang, X.; Li, Y.; Li, S.; Lu, G. *Catal. Commun.* **2007,** *8*, 1267-1273.

[45] leming, G. R.; Knight, A. W. E.; Morris, J. M.; Morrison, R. J. S.; Robinson, G. W. *J. Am. Chem. Soc.* **1977,** *99*, 4306-4311.

[46] Falke, S. M.; Rozzi, C. A.; Brida, D.; Maiuri, M.; Amato, M.; Sommer, E.; De Sio, A.; Rubio, A.; Cerullo, G.; Molinari, E.; et al. *Science* **2014,** *344*, 1001-1005.

[47] Shi, J.; Isakova, A.; Abudulimu, A.; van den Berg, M.; Kwon, O. K.; Meixner, A. J.; Park, S. Y.; Zhang, D.; Gierschner, J.; Lüer, L. *Energy Environ. Sci.* **2018,** *11*, 211-220.

[48] Lakadamyali, F.; Reynal, A.; Kato, M.; Durrant, J. R.; Reisner, E. *Chem. Eur. J.* **2012,** *18*, 15464-15475.

[49] Qureshi, M.; Takanabe, K. *Chem. Mater.* **2017,** *29*, 158-167.

[50] Pellegrin, Y.; Odobel, F. *C. R. Chim.* **2017,** *20*, 283-295.

Chapter 4.

Molecular Design and Excited State Engineering for Efficient Supramolecular Photocatalytic Hydrogen Evolution System

4.1. Introduction

In the last few decades, the development of photocatalytic water-splitting systems has been a major focus to produce hydrogen gas on a commercial scale.[1-2] For example, metal cocatalyst-decorated inorganic semiconductors have shown an impressive hydrogen evolution rate (HER),[3] but a limited visible light absorption. But unlike inorganic materials, organic materials have the advantage of having an easily tunable band gap: therefore, to better utilize solar light, photocatalytic systems using organic semiconducting materials have been reported as well.[4-5] So far, systems such as the polymeric systems[6-8] and covalent organic frameworks[9-15] have been reported with promising performances, but they usually have low water-compatibilities due to their hydrophobicity. Furthermore, reproducibility is questionable because of the sophisticated control of size and the molecular weight is difficult. Other frameworks, such as self-assembled molecules consisting of amphiphilic organic building blocks, have also been recently reported.[16-22] These supramolecules made by bottom-up

approaches usually have good water-compatibilities and ease of structural control by designing their building block molecules. Although these supramolecules are promising candidates for the next generation of organic photocatalysts, their activities still remain low.[22] Besides, the possibility of supramolecular photocatalytic system remains unclear as only a few building blocks like perylene imides[17, 19, 22] or porphyrins[20, 23] were reported. Moreover, one fatal weakness of organic semiconducting materials as photocatalysts is its typically strong exciton binding energy. Many researchers have explored new ways to overcome this weakness such as donor-acceptor type heterojunctions in polymeric systems[24-25] or intimate H-aggregation in self-assembled molecular systems.[17, 26-27] In a previous work, I used iodide ions to extend the exciton lifetime of the organic material, giving the system more opportunities to run the desired photocatalytic cycle, but had limited visible light absorption and an unclear mechanism regarding the role of the iodide ion.[28]

Here, I developed a highly efficient and stable supramolecular photocatalytic system which consists of noble organic materials with excellent visible light absorption. Its advantages lies not only in the ease of control of its characteristics, like other supramolecular systems, but also in that it has a distinctive and efficient method to overcome high exciton binding energies. I used various halogen ions to enhance intersystem crossing (ISC) of excitons. This strategy effectively suppressed unwanted pathways, leaving only the desired photocatalytic hydrogen evolution cycle. With adequate additives, a 13 mL aqueous solution of the supramolecular photocatalytic

system produced about 6 mmol of hydrogen gas, and each building block, including organic parts, operated along with photocatalytic cycle about 20,000 times during 2 days under visible light irradiation. Additionally, deep analysis of the photocatalytic mechanism has provided clear evidence of the role of additives like metal cocatalysts or halogen ions into. I expect that my study provides sound insights into upgrading the performances of organic materials in the field of photocatalytic hydrogen evolution.

4.2. Experimental Section

Materials: All reagents and solvents obtained from commercial suppliers (Sigma-Aldrich, Alfa Aesar Co., and TCI Co.) were used without further purification unless otherwise stated. All glassware, syringes, magnetic stirring bars, and needles were thoroughly dried in a convection oven. Reactions were monitored using thin layer chromatography (TLC) with commercial TLC plates (silica gel 60 F254, Merck Co.). Silica gel column chromatography was performed with silica gel 60 (particle size 0.063-0.200 mm, Merck Co.).

Synthesis of 2-(4-(pyridine-4-yl)phenyl)acetonitrile (3): 2-(4-bromophenyl)acetonitrile (2.66 g, 13.6 mmol) was dissolved in 30 mL THF, and a 25mL aqueous solution of 4-pyridineboronic acid (2 g, 16.3 mmol) and K_2CO_3 (7 g, 50

mmol) was added, then 20 ml ethylalcohol was added finally. The mixture was stirred at 80 °C and degassed by using N_2 bubbles for 30 mins. Tetrakis(triphenylphosphine)palladium(0) (0.16 g, 0.14 mmol) was dissolved in 10 ml THF, degassed by using N_2 bubbles for 30 mins, then it was added to the mixture dropwise. The mixture was stirred overnight at 80 °C at N_2 atmosphere. The mixture was cooled to room temperature, poured into water (200 mL) and extracted with ethyl acetate (200 mL) three times. The combined organic layer was dried over MgSO4 and evaporated. The crude product was purified by using column chromatography (elunt, hexane : ethyl acetate = 5 : 5, v/v) to give a white crystalline product.

White solid, Yield: 2.6 g (99 %). ^{1}H NMR (300 MHz, $CDCl_3$) δ 8.68 (d, J = 4.6 Hz, 2H), 7.66 (d, J = 7.7 Hz, 2H), 7.48 (m, J = 7.4 Hz, 4H), 3.83 (s, 1H)

Synthesis of (4): 2-(4-(pyridin-4-yl)phenyl)acetonitrile (3, 0.97 g, 5.01 mmol) and 4,4',4''-nitrilotribenzaldehyde (4, 0.5 g, 1.52 mmol) were dissolved in 10 mL THF, 100 mL ethylalcohol was added. 0.51 g of potassium hydroxide was dissolved in 50 mL ethylalcohol, then it was added to the mixture dropwise. The mixture was stirred 10 minutes further, then it was filtered. The filtrate was washed by ethylalcohol several times. The resultant filtrate was dried and gave an orange crystalline product.

Orange solid, Yield: 0.9 g (70 %). ^{1}H NMR (300 MHz, $CDCl_3$) δ 8.70 (d, J = 5.9 Hz, 2H), 7.94 (d, J = 8.7 Hz, 2H), 7.82 (d, J = 8.4 Hz, 2H), 7.74 (d, J = 8.5 Hz, 2H), 7.58 (s, 1H), 7.55 (d, J = 5.9 Hz, 2H), 7.27 (d, J = 6.3 Hz, 2H).

Synthesis of (6): 5 (0.4 g, 0.47 mmol) was dissolved in 30 mL THF, and iodomethane (1.98 g, 14.0 mmol) was added dropwise. The solution was further stirred overnight in room temperature. After that, the solution was poured into 100 mL dichloromethane, filtered, and the residue washed with dichloromethane thoroughly to give red product.

Red solid, Yield: 0.4 g (67 %). ^{1}H NMR (300 MHz, DMSO) δ 9.04 (d, J = 7.1 Hz, 2H), 8.57 (d, J = 6.9 Hz, 2H), 8.25 (m, J = 10.5 Hz, 3H), 8.06 (dd, J = 14.8, 8.7 Hz, 4H), 7.33 (d, J = 8.7 Hz, 2H), 4.35 (s, 3H).

Synthesis of molecule 2 (7): 6 (0.4 g, 0.31 mmol) was dissolved in 10 ml DMF, and a 20 ml MeOH solution of Tetrabutylammonium chloride (2.58 g, 9.3 mmol) was added dropwise. The solution was further stirred for 2 days, poured into 100 ml toluene. Red solid was collected by filtration and washed with toluene to give the product.

Red solid, Yield: 0.2 g (47 %). ^{1}H NMR (300 MHz, MeOD) δ 8.91 (d, J = 6.9 Hz, 2H), 8.46 (d, J = 7.0 Hz, 2H), 8.15 (d, J = 8.7 Hz, 2H), 8.05 (m, J = 11.6, 6.7 Hz, 5H), 7.29 (d, J = 15.9 Hz, 2H), 4.42 (s, 3H). MS (ESI) (calcd m/z for $C_{63}H_{48}N_7^{3+}$ 300.80; found, 300.7998) m/z: 300.7998, 301.1329, 301.4682, 301.8026, 302.1373

Scheme 4-1. Synthetic route of molecule **2**.

Measurements: ^{1}H NMR spectra were recorded on a Bruker Avance 300 spectrometer (300 MHz). Mass (MS) spectra were acquired by using Thermo Scientific Q Exactive. UV-Vis absorption spectra were measured using a Shimazu, UV-1650 PC spectrometer. Fluorescence spectra were obtained by using a Varian Cary Eclipse fluorescence spectrophotometer. A UV hand-held lamp (365 nm, 1.2 mW cm^{-2}) was used as a UV light source, and a xenon arc lamp (300 W) was used as a visible light source through a color filter (Newport). Solar light was simulated by a solar simulator, PEC-L01

(Peccell). Time-resolved fluorescence lifetime experiments were performed through the time-correlated single photon counting (TCSPC) methods by using a FluoTime 200 instrument (Picoquant, Germany). A 377 nm pulsed diode laser with fwhm ~70 ps was used as an excitation source. Fluorescence decay profiles were analyzed by FluoFit Pro software, using exponential fitting models through deconvolution employing instrumental response functions (IRF). Dynamic Light Scattering (DLS) measurements were performed on an Otsuka Electronics, DLS-7000. Electrophoretic Light Scattering (ELS) measurements were conducted by using ELS Z-1000 (Otsuka Portal). Transmission electron microscope (TEM) images were recorded on a JEOL, JEM-2100F and JEM-3010 and FEI, Tecnai F20. The TEM samples were prepared by dropping a droplet of each aqueous solution on a copper grid and drying in ambient condition. Raman spectrum was gathered by using LabRAM HR Evolution (HORIBA). The electrochemical experiments were conducted using a Vertexone equipped with a three electrode cell assemble including a glassy carbon working electrode, a platinum wire counter electrode, and an $Ag/AgNO_3$ reference electrode. The HOMO level was calculated using the onset oxidation potential (E_{ox}), and ferrocene ($E_{Fc/Fc+)}$ reference was used for calibration. (E_{HOMO} = - [E_{ox} –$E_{Fc/Fc+}$ + 4.8] eV). The LUMO level was calculated from the electrochemically measured HOMO level and the band gap derived from UV-Vis absorption edge. ($E_{LUMO} = E_{HOMO} + Eg$)

Photocatalytic water splitting Experiments: 13 mL of aqueous solutions were used

for the hydrogen evolution system. All samples were continuously stirred at 200 rpm using a magnetic stirrer. A 300W Xenon lamp with 400 nm long-pass filters and water filter was used as a light source. The temperature was maintained at 25 ℃. The irradiated light intensity at the sample center was 303 mW/cm^2. The evolved amount of hydrogen was measured using gas chromatography(GC, Agilent Technologies 7890A or 7890B) every 30 minutes.

4.3. Results and Discussion

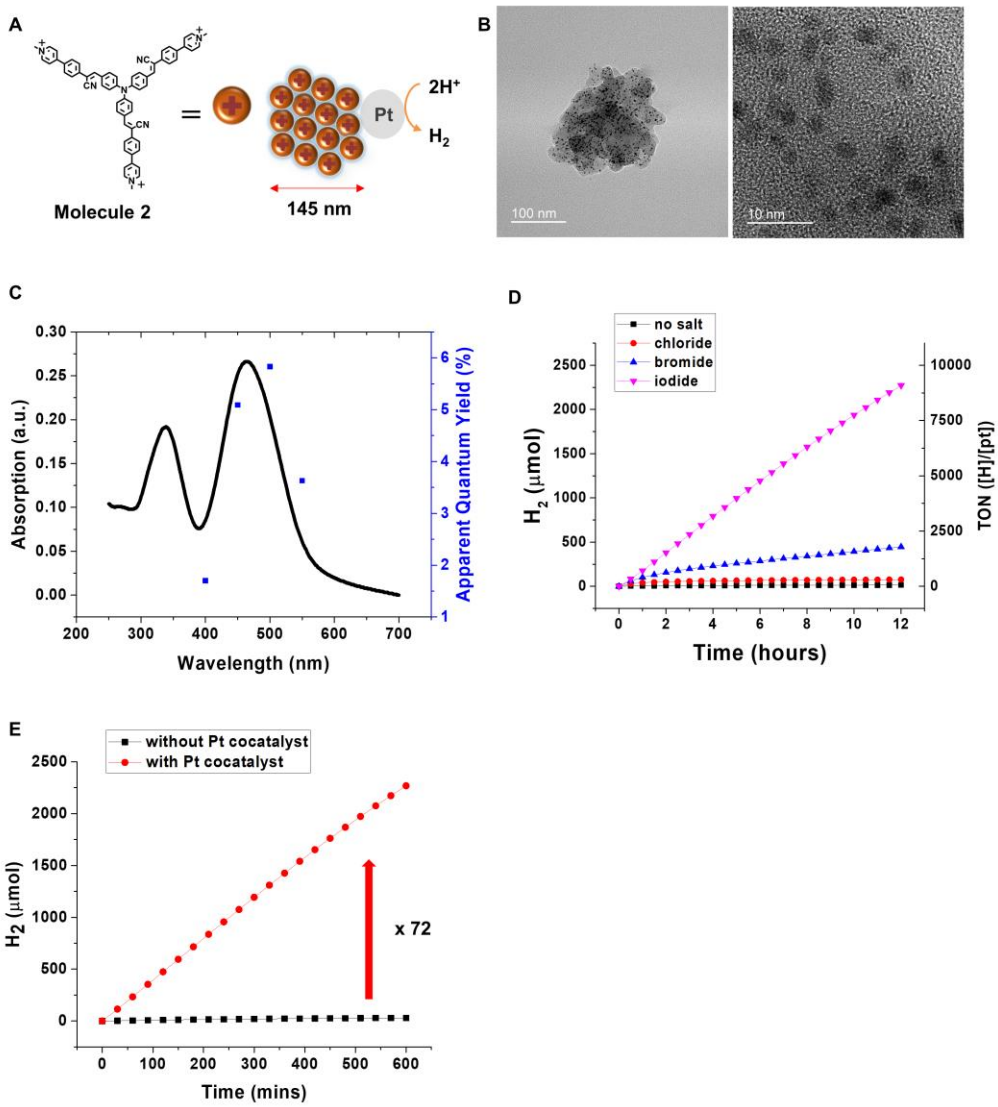

Figure 4-1. (a) Molecular structure of molecule 2 and schematic view of the supramolecular phtocatalytic system (b) TEM and HRTEM images of the supramolecular system after 24 hours of photocatalytic reaction (c) UV-Vis spectrum

of the supramolecular system and apparent quantum yield for hydrogen evolution versus wavelength (d) HER change of the supramolecular system upon addition of halide ions (e) HER change of the supramolecular system upon addition of Pt cocatalyst.

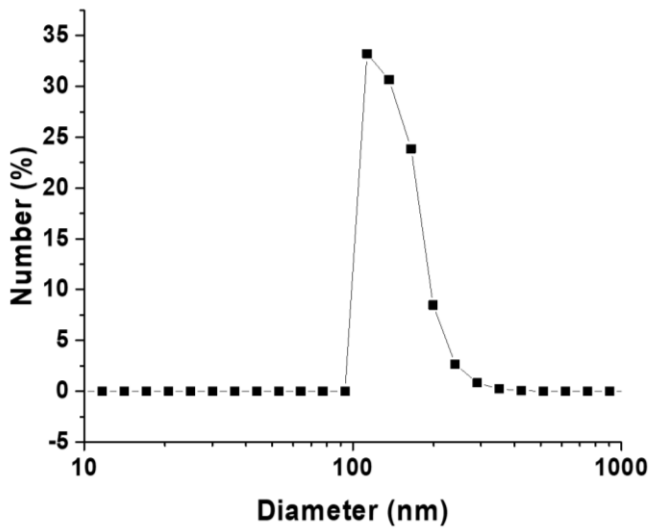

Figure 4-2. Dynamic light scattering (DLS) graph of 0.05 mM aqueous solution of molecule 2.

I designed molecule 2 to be the building block to make my efficient supramolecular photocatalyst system. (Fig 4-1a) The triphenylamine moiety in its core, which is normally used as a donor for photoactive materials, was combined with hydrophilic and electron-deficient pyridinium arms, giving molecule 2 a strong intramolecular charge transfer structure with high absorbance in the visible region. In aqueous solution, molecule 2 forms self-assembled supramolecules from the balance between

the hydrophobic core and the hydrophilic arm. The average diameter of supramolecules were about 145 nm in dynamic light scattering (DLS, Fig S1) measurement and zeta potential of the supramolecules was +38 mV in electrophoretic light scattering (ELS) measurement. During photoreduction process, metal co-catalysts grew on the surface of supramolecule. It allowed rapid electron transfer from supramolecular system to metal co-catalyst, so that enhanced the hydrogen production performance. The positively zeta-potential of supramolecules also effected to the HER performance by enabling effectively interaction with negatively charged halides additives[18, 29] or Pt colloids which have negative zeta-potential.[30] The supramolecular photocatalytic system consists of molecule 2 was stable under the photocatalytic hydrogen reduction cycle, and the supramolecular structures were still observed in the dried film on the TEM 24 hours after each component was operated more than 10,000 times on average. (Fig 4-1b) In addition, the photo-reduced Pt, an important cocatalyst, was observed via TEM on the surface of these supramolecules. (Fig 4-1b) Much like metal cocatalysts decorated on inorganic semiconductors,[31-33] Pt nanoparticles on the supramolecule effectively receive electrons from photo-active supramolecules and can use them for useful reactions. Also, the apparent quantum yield (AQY) of hydrogen production was determined according to the absorption tendency of molecule 2. (Fig 4-1c) Through this, I conclude that the design of the building block molecule is directly related to the hydrogen production performance in the supramolecular photocatalytic system.

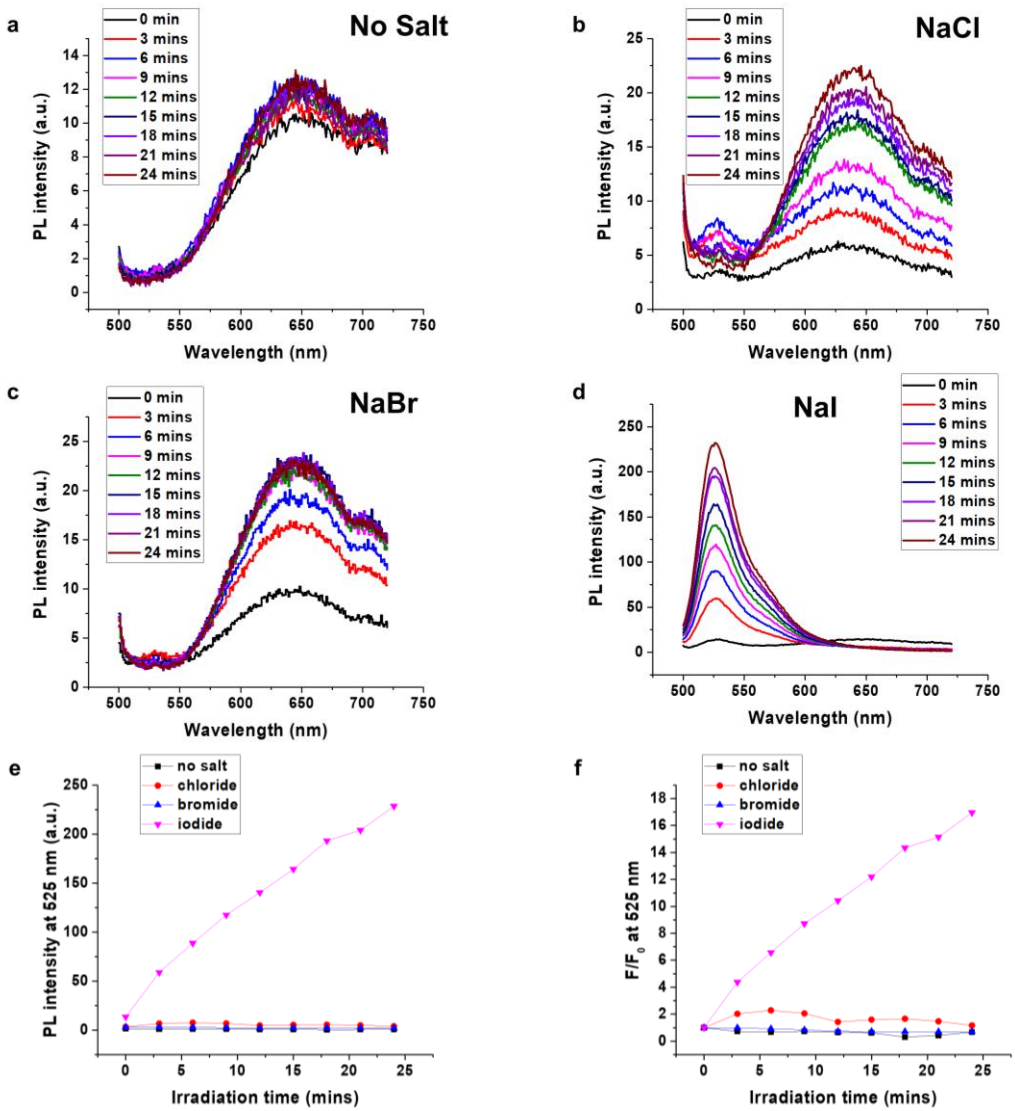

Figure 4-3. Singlet oxygen sensing experiments. PL spectrum change upon 450 nm light irradiation of (a) molecule 2 and single oxygen sensor green (SOSG) in 3 mL of aqueous solution. Solutions of the same composition (b) with 0.15 M of NaCl (c) NaBr (d) NaI. (e) PL intensity at 525 nm of each sample upon irradiation time. (f) Relative PL intensity at 525 nm of each sample upon irradiation time. Irradiation light intensity

was 3.3 mW/cm2. The concentration of molecule 2 was 12.5 μM and that of SOSG was 3.25 μM. Excitation wavelength for PL measurement was 490 nm.

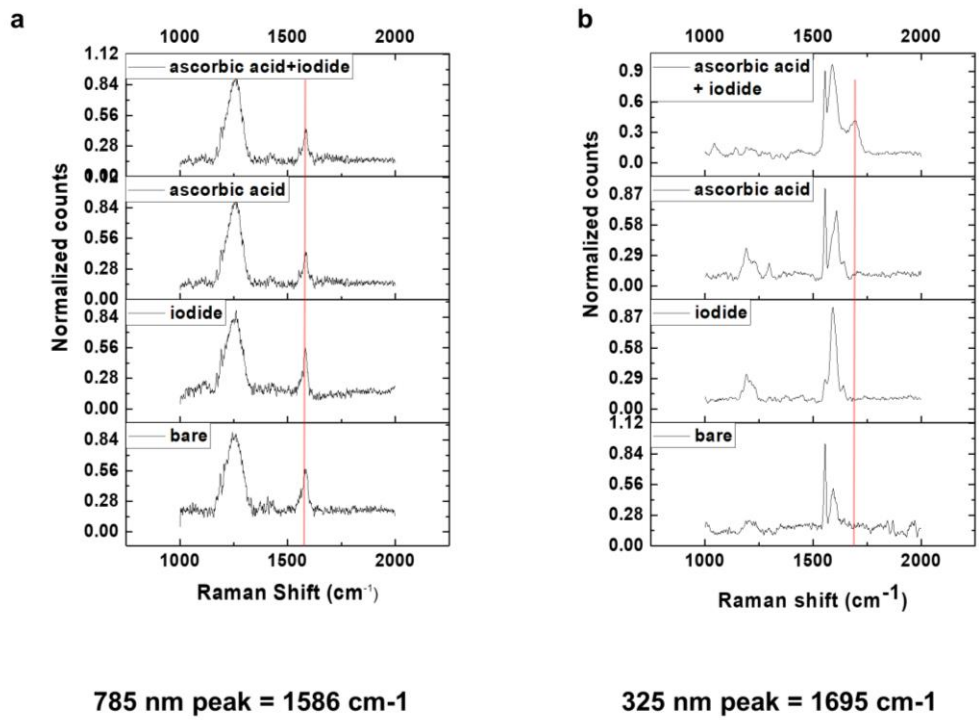

Figure 4-4. Raman spectrum using (A) 785 nm or (B) 325 nm LASER light as a scattering source. The marked Raman shift of A is 1585 cm^{-1} and for B is 1695 cm^{-1}.

Additives were then used to improve the performance of the photocatalytic system. Pt was used as a cocatalyst, and halogens were added to improve the performance. As a result, interestingly, both TOF and TON increased dramatically by the addition of Pt cocatalyst and halogen ions by controlling post-photoexcitation steps. To investigate the causal relationship between the increase in the performance of the photocatalytic

system by the addition of halogen, hydrogen production was carried out by adding different types of halogen. (Fig 1d) In addition, singlet oxygen formation experiments, (Fig 4-3) and Raman scattering experiments (Fig 4-4) were conducted to understand the mechanism of this enhanced performance. First, in the case of TOF and TON of the supramolecular photocatalysts, when all other conditions were the same, there was a tendency to increase by the atomic weight of halogen added. (Fig 4-1d) From this typical trend, it can be seen that increasing the intersystem crossing by the addition of heavy atoms has a decisive effect on the hydrogen production performance. That is, as pointed out in many photocatalytic systems,[34-35] it is possible to increase the chance that can be used for desired reactions by manipulating the excited state with a longer lifetime in the supramolecular photocatalytic hydrogen evolution system as well.

The change in the excited state of molecule 2 upon the addition of halogen was examined through a singlet oxygen sensing experiment.[35-37] The light was irradiated by a 300W xenon lamp equipped with a 450 nm band-pass filter to a mixture of molecule 2 and singlet oxygen sensor green (SOSG) in each halogen aqueous solution of 0.15 M concentration. The intensity of light was 3.3 mW/cm^2 and the irradiation area was 1 cm^2. 450 nm light excites molecule 2 and the excited molecule 2 shows a different pathway depending on the additives, halogen ions. The addition of heavy atoms significantly enhanced the intersystem crossing of singlet excited molecule 2, and then singlet oxygen can be formed through triplet-triplet energy transfer. When iodide was added, a sufficient amount of singlet oxygen was formed to be sensed by SOSG. (Fig

4-3) This is also consistent with the trends in hydrogen evolution experiments. (Fig 4-1d)

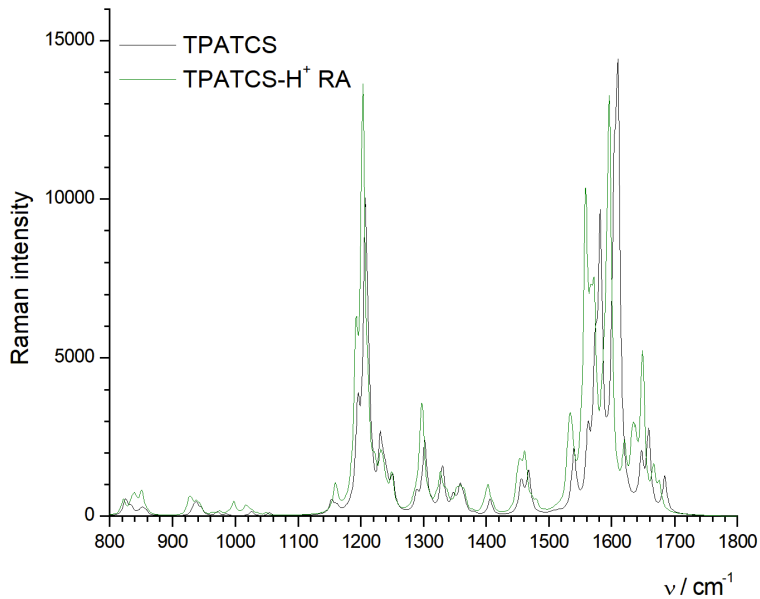

Figure 4-5. Raman spectrum of molecule 2 predicted by DFT calculation.

I was also able to trace the pathway after photoexcitation through Raman scattering experiments.[38] As illustrated in the UV-Vis spectrum of Molecule 2, (Fig 4-1c), information on only the ground state of molecule 2 can be obtained when a 785 nm laser is used as a Raman scattering source. Therefore, all samples showed similar peaks regardless of the type of additives. (Fig 4-4) Further, the positions of peaks (near 1200 cm^{-1} and 1600 cm^{-1}) were also predicted by DFT calculations. (Fig 4-5) Thus, it

indicates that these peaks provide information on molecule 2. On the other hand, when a 325 nm laser is used, information on the excited state was most probably obtained. Interestingly, in this case, the peaks varied depending on the additives. (Fig 4-4) After molecule 2 was excited, the peak at 1750 cm^{-1} was apparent only when iodide and ascorbic acid was present. This position was similar to the position of the peak of reduced species of molecule 2 in DFT calculation. From this, I investigated that only when a heavy atom, iodide ion, and the electron donor, L-ascorbic acid are present, the observable photo-reduction was conducted in the Raman scattering measurement.

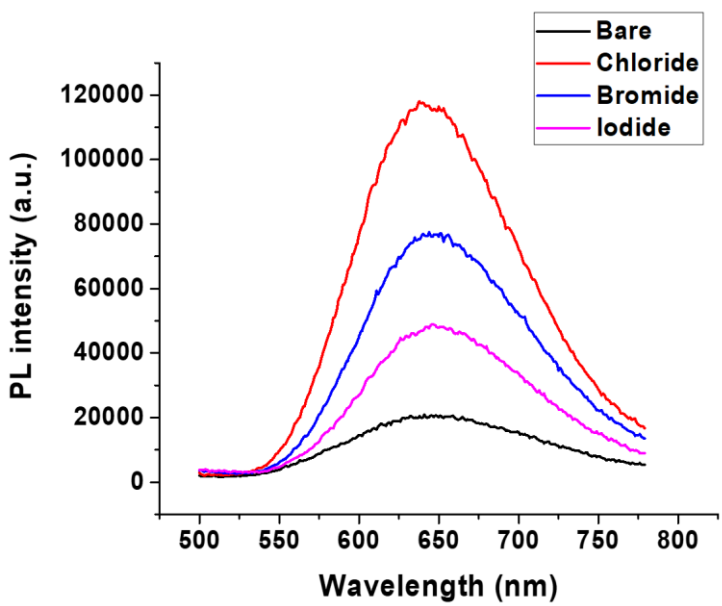

Figure 4-6. PL spectrum change of molecule 2 upon addition of halides.

The possibility of halogen being used as a source of electrons which is commonly reported[39-40] in literature was also verified. First, even when halogen was added, no hydrogen production was observed without L-ascorbic acid. In addition, x to ligand charge transfer (XLCT, X=halide) was not confirmed in the PL spectrum. (Fig 4-6) In the case of XLCT, when halogen is added, electron transfer occurs to the excited molecule, consequently, the PL is quenched.[41] However, when the halogen was added to molecule 2, the PL intensity increased. This can most likely be attributed to the fact that as the ionic strength of the aqueous solution increases, the aggregation of the hydrophobic molecule 2 becomes stronger and the molecular vibrations become weaker. As the non-radiative decay pathway was reduced, the PL intensity increased. These results indicate that halogen does not contribute to the photocatalytic cycle as an electron donor in our case.

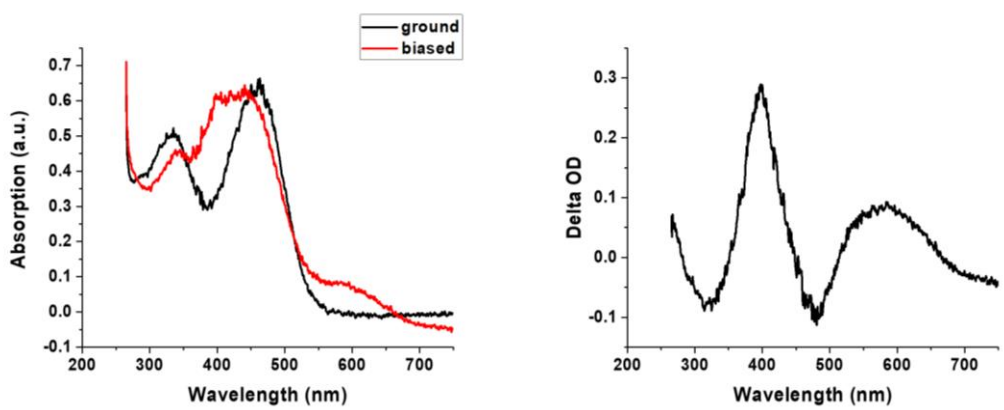

Figure 4-7. UV-Vis spectroelectrochemical response of the molecule 2 in DMF. (0.1 M Bu_4NPF_6)

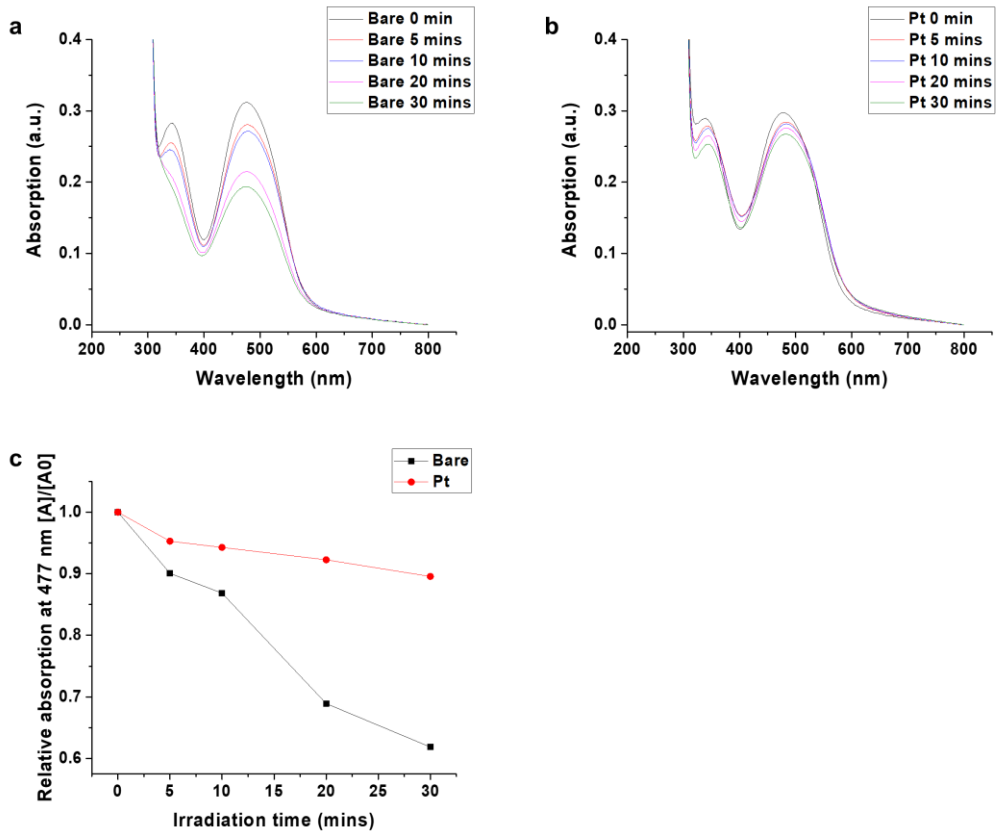

Figure 4-8. UV-Vis spectrum change upon 400 nm irradiation of (a) 0.01 mM of molecule 2 in 0.1 M of NaI and 0.1 M of L-ascorbic acid aqueous solution and (b) 0.01 mM of molecule 2 and 0.01 mM of K_2PtCl_4 in 0.1 M of NaI and 0.1 M of L-ascorbic acid aqueous solution. (c) relative absorption change upon irradiation of each sample at 477 nm.

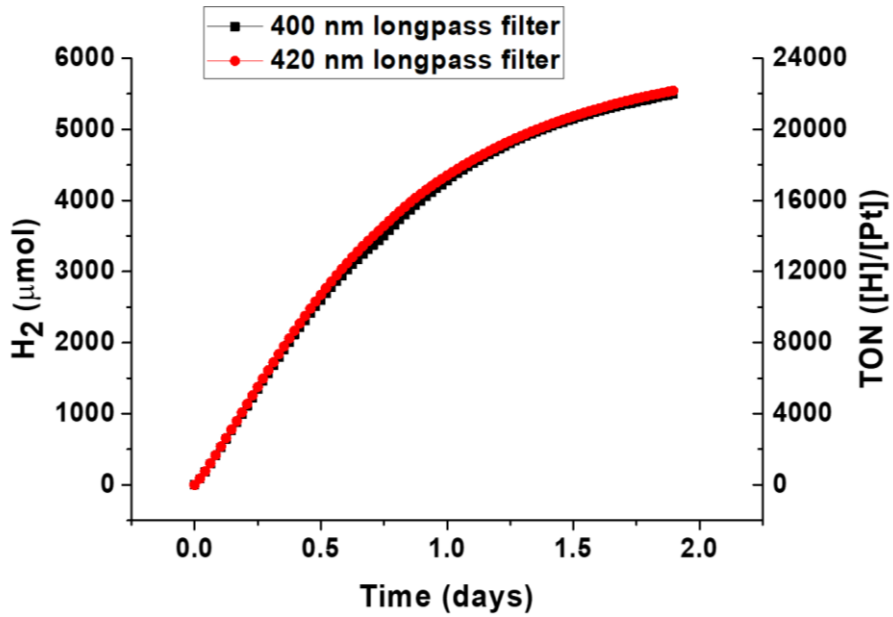

Figure 4-9. HER performances of the supramolecular photocatalytic system with 400 nm long-pass filter or 420 nm long-pass filter.

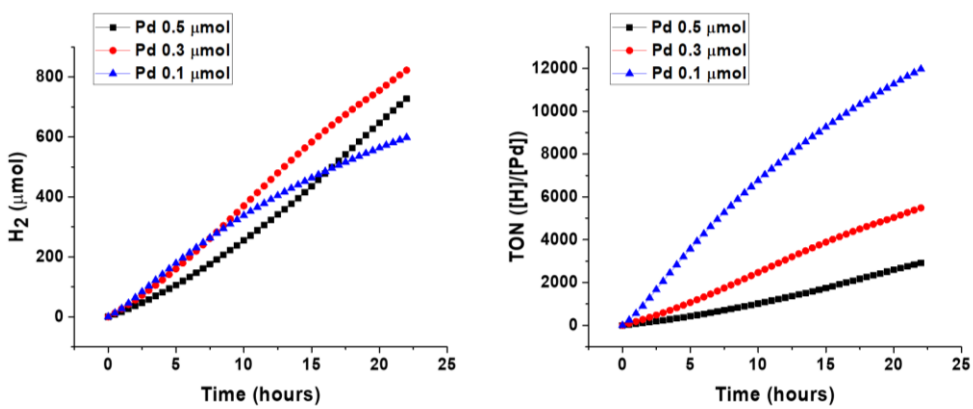

Figure 4-10. HER performances of the supramolecular system with Pd cocatalyst.

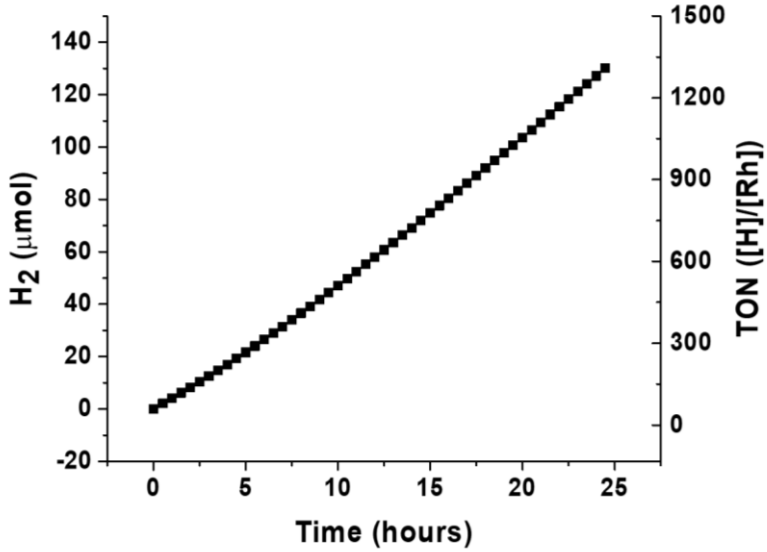

Figure 4-11. HER performance of the supramolecular system with Rh cocatalyst.

The supramolecular photocatalytic system consisting of molecule 2 showed a HER performance about 8 mmol/g·h without metal cocatalyst. The turnover number (TON) of molecule 2 for 10 hours reached 100. (Fig 4-1e) However, without the cocatalyst, the stability of the system was relatively low, which may be due to radical instability as it appears in many organic materials. To investigate the stability of the reduced radical, we assigned absorption band of reduced species of molecule 2 first. The absorption spectrum of reduced species of molecule 2 was confirmed through an electrochemical experiment. Especially at 400 nm, a distinctive peak with neutral species appeared. (Fig 4-7) This peak has something to do with degradation mechanism of molecule 2. It

has been reported that re-excited organic radicals are highly degradable.[42] For the supramolecule with iodide (triplet enhancing additive) L-ascorbic acid (electron donor), degradation was observed in the UV-vis spectrum upon irradiation with 400 nm light. (Fig 4-8) However, with Pt, this degradation was dramatically reduced. (Fig 4-8) This radical stability has an important influence on hydrogen production. Comparing the experimental results with the 400 nm long-pass filter and the 420 nm long-pass filter, the HER of each sample was almost similar. (Fig 4-9) The irradiated light intensity to the sample was reduced from 303 mW/cm^2 (for a system with a 400 nm long-pass filter) to 293 mW/cm^2 (420 nm long-pass filter), and molecule 2 had an absorbance at 400 nm to some extent but showed similar TON. Further, this relationship was also displayed through UV-vis and AQY: the AQY of the photocatalytic system at a certain wavelength showed a tendency similar to the Uv-vis spectrum of molecule 2. (Fig 4-1c) However, at 400 nm, the AQY was relatively low compared to this trend, and this data also reflected by the stability of the reduced species. Through this, I revealed that in the supramolecular photocatalytic system, the metal cocatalyst not only provides a catalytic site (Fig 4-1e, turnover frequency of Pt, $TOF_{Pt} \sim 966\ h^{-1}$) but also increases the stability of the photo-active organic material by draining the reduced electrons of the organic system effectively. This photodegradation was also reduced greatly when Pd (Fig 4-10) and Rh (Fig 4-11) were used as cocatalysts. However, in these cases, the TOF was significantly lower than when Pt was used. ($TOF_{Pd} \sim 727\ h^{-1}$, $TOF_{Rh} \sim 40\ h^{-1}$)

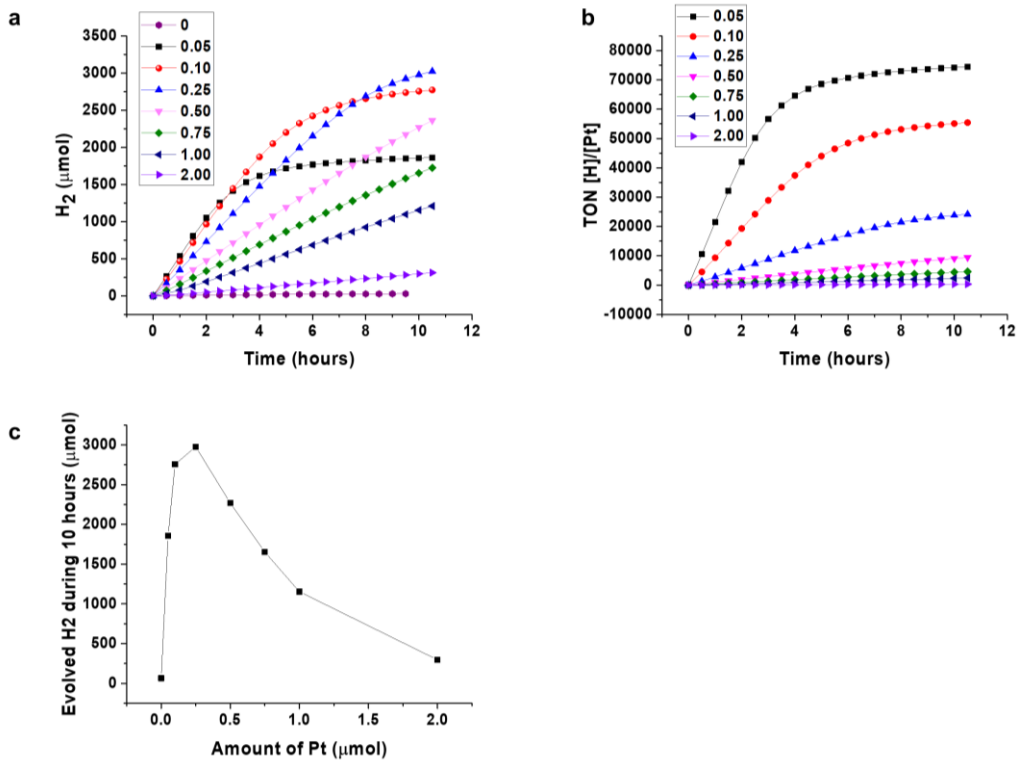

Figure 4-12. HER performances of the supramolecular photocatalytic system with various amount of Pt.

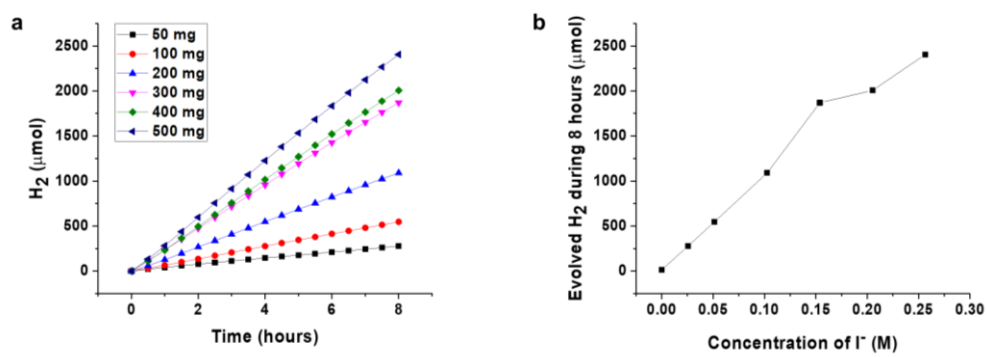

Figure 4-13. HER performances of the supramolecular photocatalytic system with

various concentration of iodide.

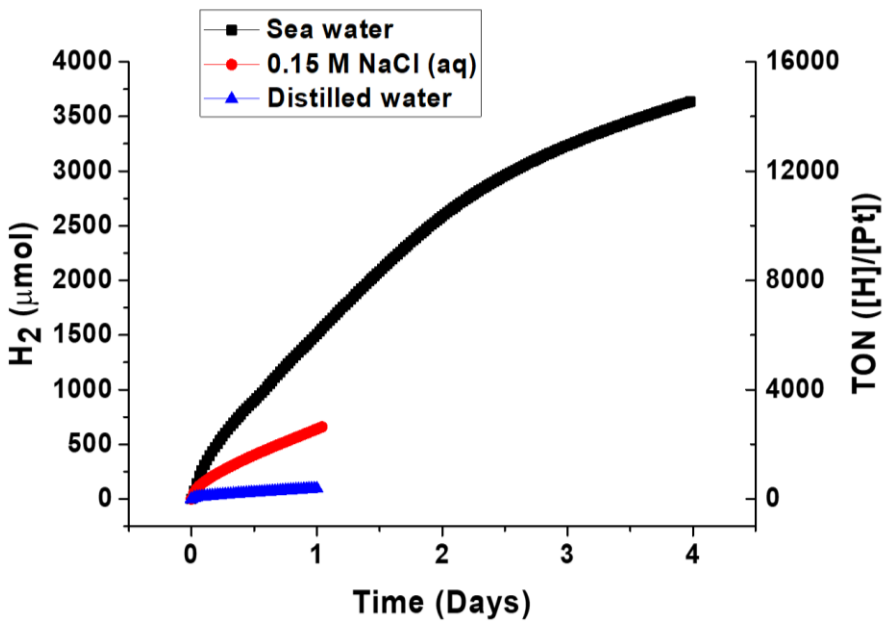

Figure 4-14. HER performances of the supramolecular system in a distilled water, 0.15 M of NaCl aqueous solution and seawater under solar simulator irradiation.

For a proper evaluation of the supramolecular photocatalytic system,[43] optimization experiments were conducted. While maintaining the amount of molecule 2, I varied the amounts of Pt or iodide. While 0.65 μmol of molecule 2 in a 0.15 M of NaI aqueous solution was used, a sample with 0.25 μmol of Pt produced the most hydrogen gas for 10 hours. (about 3 mmol, Fig 4-12) When a smaller amount of Pt was used, $TOFs_{Pt}$ were over 10,000 for the first few hours, then decreased rapidly. In this case, the

amount of Pt was not enough to effectively depopulate radicals. When more than 0.25 μmol of Pt was used, TON_{Pt} for 10 hours decreased again. This decrease was most likely caused by too much scattering of Pt colloids which interferes with the photo-active organic molecules' ability to absorb light. On the other hand, when varying the concentration of iodide form 0 M to 0.26 M, both TON_{Pt} and TOF_{Pt} increased proportionally with the concentration of iodide in the supramolecular photocatalytic system. With 0.65 μmol of Molecule 2 and 0.5 μmol of Pt, the supramolecular photocatalyst in 0.26 M of NaI aqueous solution produced the most hydrogen gas. (2.4 mmol, Fig 4-13) The results from using external halogen ions in the photocatalytic water splitting system have opened new possibilities for the use of seawater, the most abundant resource on earth. In addition, I used a solar simulator as a light source to create a more practical photocatalytic condition. Although the chloride ion showed the weakest effect among the halogen additives in my experiment due to its relatively small molecular weight, seawater contains a much higher concentration of chloride than that used in my experiments. I collected seawater directly from the West Sea of Korea for use in experiments. In general, 1 kg of seawater in the West Sea of Korea contains about 33 g of salts, including NaCl, $MgCl_2$, and Na_2So_4. Therefore, the seawater contains a much higher amount of NaCl than the 0.15 M NaCl aqueous solution (about 8.8 g of NaCl in 1 kg of solution) used in the experiment. Consequently, the sample prepared by using seawater showed much larger TOF_{Pt} (577 h^{-1}), TON_{Pt} during 24 hours (6035), and 14542 during 4 days than the supramolecular

photocatalyst in distilled water (TOF_{Pt} ~ 68 h^{-1}, TON_{Pt} ~ 386) as well as the supramolecular photocatalyst in 0.15 M NaCl. (TOF_{Pt} ~ 380 h^{-1}, TON_{Pt} ~ 2557, Fig 4-14) Since many efforts have been made to utilize seawater in the field of water splitting,[44-46] it is very encouraging that it showed better performance (over 37 times better TON_{Pt}) than distilled water.

4.4. Conclusions

In summary, I designed a noble molecule as an effective building block for the supramolecular hydrogen evolution catalyst and increased its performance by utilizing a triplet excited state. Molecule 2 self-assembled into positively charged supramolecules with about 100 nanometers in diameter in aqueous solution, and as supramolecules, they hold advantages in visible light absorption and in interactions with negatively charged additives. However, its performance was far lower compared to recently reported organic or inorganic photocatalytic systems. From here, I analyzed the photoexcitation steps of the supramolecular system and then found the appropriate method to upgrade photocatalytic performance. The results of this set indicated that halide ions can interact with these positively charged supramolecule, improving the HER performance. Upon addition of halogen ions, the ISC of molecule 2 exciton was enhanced, then the resulting triplet excited state with sufficient lifetime provided the

system with more chances to obtain an electron from a sacrificial reagent. After reduction, however, the supramolecular system with a relatively low TOF was unstable upon photo-irradiation, and as a result, the TON still did not meet expectations. Instead, metal cocatalysts were used to increase the stability of the supramolecular system by draining the reduced electrons effectively, with Pt displaying an impressive TOF as well. Each component of this supramolecular system can operate over 20,000 in just two days and combined with an ideal molecular design and mechanistic studies, has the potential to improve performance even further.

4.5. References

Reference List

[1] McKone, J. R.; Lewis, N. S.; Gray, H. B. *Chem. Mater.* **2013,** *26*, 407-414.

[2] Yuan, L.; Han, C.; Yang, M. Q.; Xu, Y. J. *Int. Rev. Phys. Chem.* **2016,** *35*, 1-36.

[3] Takata, T.; Jiang, J.; Sakata, Y.; Nakabayashi, M.; Shibata, N.; Nandal, V.; Seki, K.; Hisatomi, T.; Domen, K. *Nature* **2020,** *581*, 411-414.

[4] Warnan, J.; Reisner, E. *Angew. Chem. Int. Ed.* **2020,** *59*, 17344-17354.

[5] Bellani, S.; Antognazza, M. R.; Bonaccorso, F. *Adv. Mater.* **2019,** *31*, 1801446.

[6] Wang, L.; Fernandez-Teran, R.; Zhang, L.; Fernandes, D. L.; Tian, L.; Chen, H.; Tian, H. *Angew. Chem. Int. Ed.* **2016,** *55*, 12306-10.

[7] Pati, P. B.; Damas, G.; Tian, L.; Fernandes, D. L. A.; Zhang, L.; Pehlivan, I. B.; Edvinsson, T.; Araujo, C. M.; Tian, H. N. *Energy Environ. Sci.* **2017,** *10*, 1372-1376.

[8] Bai, Y.; Wilbraham, L.; Slater, B. J.; Zwijnenburg, M. A.; Sprick, R. S.; Cooper, A. I. *J. Am. Chem. Soc.* **2019,** *141*, 9063-9071.

[9] Wang, X.; Chen, L.; Chong, S. Y.; Little, M. A.; Wu, Y.; Zhu, W. H.; Clowes, R.; Yan, Y.; Zwijnenburg, M. A.; Sprick, R. S.; Cooper, A. I. *Nat. Chem.* **2018,** *10*, 1180-1189.

[10] Jena, H. S.; Krishnaraj, C.; Parwaiz, S.; Lecoeuvre, F.; Schmidt, J.; Pradhan, D.; Van Der Voort, P. *ACS Appl. Mater. Inter.* **2020,** *12*, 44689-44699.

[11] Wang, T.-X.; Liang, H.-P.; Anito, D. A.; Ding, X.; Han, B.-H. *J. Mater. Chem. A* **2020,** *8*, 7003-7034.

[12] Xiao, W.-J.; Wang, Y.; Wang, W.-R.; Li, J.; Wang, J.; Xu, Z.-W.; Li, J.; Yao, J.; Li, W.-S. *Macromolecules* **2020,** *53*, 2454-2463.

[13] Luo, S.; Zeng, Z.; Zeng, G.; Liu, Z.; Xiao, R.; Xu, P.; Wang, H.; Huang, D.; Liu, Y.; Shao, B.; Liang, Q.; Wang, D.; He, Q.; Qin, L.; Fu, Y. *J. Mater. Chem. A* **2020,** *8*, 6434-6470.

[14] Zhang, S.; Cheng, G.; Guo, L.; Wang, N.; Tan, B.; Jin, S. *Angew. Chem. Int. Ed. A* **2020,** *59*, 6007-6014.

[15] Gao, X.; Shu, C.; Zhang, C.; Ma, W.; Ren, S.-B.; Wang, F.; Chen, Y.; Zeng, J. H.; Jiang, J.-X. *J. Mater. Chem. A* **2020,** *8*, 2404-2411.

[16] Dumele, O.; Chen, J.; Passarelli, J. V.; Stupp, S. I. *Adv. Mater.* **2020,** *32*, 1907247.

[17] Weingarten, A. S.; Kazantsev, R. V.; Palmer, L. C.; McClendon, M.; Koltonow, A. R.; Samuel, A. P.; Kiebala, D. J.; Wasielewski, M. R.; Stupp, S. I. *Nat. Chem.* **2014,** *6*, 964-70.

[18] Lee, H. J.; Kim, J.; Abudulimu, A.; Cabanillas-Gonzalez, J.; Nandajan, P. C.; Gierschner, J.; Luer, L.; Park, S. Y. *J. Phys. Chem. C* **2020,** *124*, 6971-6978.

[19] Weingarten, A. S.; Kazantsev, R. V.; Palmer, L. C.; Fairfield, D. J.; Koltonow, A. R.; Stupp, S. I. *J. Am. Chem. Soc.* **2015,** *137*, 15241-6.

[20] Yang, X. Y.; Hu, Z. C.; Yin, Q. W.; Shu, C.; Jiang, X. F.; Zhang, J.; Wang, X. H.; Jiang, J. X.; Huang, F.; Cao, Y. *Adv. Funct. Mater.* **2019,** *29*, 1808156.

[21] Nolan, M. C.; Walsh, J. J.; Mears, L. L. E.; Draper, E. R.; Wallace, M.; Barrow, M.; Dietrich, B.; King, S. M.; Cowan, A. J.; Adams, D. J. *J. Mater. Chem. A* **2017,** *5*, 7555-7563.

[22] Kong, K.; Zhang, S.; Chu, Y.; Hu, Y.; Yu, F.; Ye, H.; Ding, H.; Hua, J. *Chem. Commun.* **2019,** *55*, 8090-8093.

[23] Zhang, Z.; Zhu, Y.; Chen, X.; Zhang, H.; Wang, J. *Adv. Mater.* **2019,** *31*, 1806626.

[24] Yang, H.; Li, X.; Sprick, R. S.; Cooper, A. I. *Chem. Commun.* **2020,** *56*, 6790-6793.

[25] Kosco, J.; Bidwell, M.; Cha, H.; Martin, T.; Howells, C. T.; Sachs, M.; Anjum, D. H.; Gonzalez Lopez, S.; Zou, L.; Wadsworth, A.; Zhang, W.; Zhang, L.; Tellam, J.; Sougrat, R.; Laquai, F.; DeLongchamp, D. M.; Durrant, J. R.; McCulloch, I. *Nat. Mater.* **2020,** *19*, 559-565.

[26] Weingarten, A. S.; Dannenhoffer, A. J.; Kazantsev, R. V.; Sai, H.; Huang, D.; Stupp, S. I. *J. Am. Chem. Soc.* **2018,** *140*, 4965-4968.

[27] Hestand, N. J.; Kazantsev, R. V.; Weingarten, A. S.; Palmer, L. C.; Stupp, S. I.; Spano, F. C. *J. Am. Chem. Soc.* **2016,** *138*, 11762-11774.

[28] Baranoff, E.; Nakatsu, F.; Kamikawa, Y.; Liu, H. B.; Moriyama, M.; Kumazawa, K.; Yoshizawa, M.; Fujita, M.; Kato, T. 55th SPSJ Annual Meeting, Nagoya, Nagoya, 2006; p 688.

[29] Lee, H. J.; Kim, H. J.; Lee, E. C.; Kim, J.; Park, S. Y. *Chem. Asian J.* **2018,** *13*, 390-394.

[30] Wang, S.; Wang, X.; Jiang, S. P. *Phys. Chem. Chem. Phys.* **2011,** *13*, 6883-6891.

[31] Bartolini, M.; Gombac, V.; Sinicropi, A.; Reginato, G.; Dessì, A.; Mordini, A.; Filippi, J.; Montini, T.; Calamante, M.; Fornasiero, P.; Zani, L. *ACS Appl. Energy Mater.* **2020,** *3*, 8912-8928.

[32] Li, G.; Mark, M. F.; Lv, H.; McCamant, D. W.; Eisenberg, R. *J. Am. Chem. Soc.* **2018,** *140*, 2575-2586.

[33] Rajasekar, S.; Tiwari, V.; Srivastva, U.; Holdcroft, S. *ACS Appl. Energy Mater.* **2020,** *3*, 8988-9001.

[34] Lu, J.; Pattengale, B.; Liu, Q.; Yang, S.; Shi, W.; Li, S.; Huang, J.; Zhang, J. *J. Am. Chem. Soc.* **2018,** *140*, 13719-13725.

[35] Wang, H.; Jiang, S.; Liu, W.; Zhang, X.; Zhang, Q.; Luo, Y.; Xie, Y. *Angew. Chem. Int. Ed.* **2020,** *59*, 11093-11100.

[36] Prasad, A.; Sedlarova, M.; Pospisil, P. *Sci. Rep.* **2018,** *8*, 13685.

[37] Flors, C.; Fryer, M. J.; Waring, J.; Reeder, B.; Bechtold, U.; Mullineaux, P. M.; Nonell, S.; Wilson, M. T.; Baker, N. R. *J. Exp. Bot.* **2006,** *57*, 1725-34.

[38] Sun, H.; Öner, I. H.; Wang, T.; Zhang, T.; Selyshchev, O.; Neumann, C.; Fu, Y.; Liao, Z.; Xu, S.; Hou, Y.; Turchanin, A.; Zahn, D. R. T.; Zschech, E.; Weidinger, I. M.; Zhang, J.; Feng, X. *Angew. Chem. Int. Ed.* **2019,** *58*, 10368-10374.

[39] Li, J. X.; Ye, C.; Li, X. B.; Li, Z. J.; Gao, X. W.; Chen, B.; Tung, C. H.; Wu, L. Z. *Adv. Mater.* **2017,** *29*, 1606009.

[40] Zhang, G.; Li, G.; Lan, Z.-A.; Lin, L.; Savateev, A.; Heil, T.; Zafeiratos, S.; Wang, X.; Antonietti, M. *Angew. Chem. Int. Ed.* **2017,** *56*, 13445-13449.

[41] Nguyen, C.; Zahir, K. O. *J. Environ. Sci. Heal. B* **1999,** *34*, 1-16.

[42] Shimidzu, T.; Iyoda, T.; Koide, Y. *J. Am. Chem. Soc.* **1985,** *107*, 35-41.

[43] Qureshi, M.; Takanabe, K. *Chem. Mater.* **2017,** *29*, 158-167.

[44] Liu, J.; Liu, Y.; Liu, N. Y.; Han, Y. Z.; Zhang, X.; Huang, H.; Lifshitz, Y.; Lee, S. T.; Zhong, J.; Kang, Z. H. *Science* **2015,** *347*, 970-974.

[45] Kuang, Y.; Kenney, M. J.; Meng, Y.; Hung, W.-H.; Liu, Y.; Huang, J. E.; Prasanna, R.; Li, P.; Li, Y.; Wang, L.; Lin, M.-C.; McGehee, M. D.; Sun, X.; Dai, H. *Proc. Natl. Acad. Sci. U.S.A.* **2019,** *116*, 6624-6629.

[46] Zheng, J.; Zhao, Y.; Xi, H.; Li, C. *Rsc Adv.* **2018,** *8*, 9423-9429.

초 록 (Korean Abstract)

물은 생명의 근원이자 지구 표면에서 가장 풍부한 자원이다. 물속에서 작동 가능한 기능성 물질을 만드는 것은 생체, 에너지 분야에 응용될 수 있어 중요한 의미를 가진다. 자연계에 존재하는 많은 생물들은 수계에서 복잡한 생명활동을 수행하는 기능성 재료들을 이미 그들의 세포 소기관내에 가지고 있다. 식물들은 광합성 작용을 통해서 산소와 녹말을 만들어낸다. 동물들의 단백질은 채액내에서 자가조립을 통해 세포 소기관들을 형성하고 물질 출입과 전기 신호의 전달을 수행하고 있다. 이러한 작동원리를 모사하여 생체 조직만큼 효율적인 재료를 만들고자 하는 연구들이 많이 진행되어왔다. 그중 특히 유기재료는 분자 디자인을 통해서 다양한 특성을 부여할 수 있고 생체 내에도 적용이 용이해서 주목할만하다. 유기재료의 여러 범주 중에서도 수용액 상에서 용이하게 구조체를 형성할 수 있는 재료는 자가조립을 통해 구성 요소 하나하나가 모여서 더 큰 구조체를 형성하는 초분자이다. 초분자는 단위 분자의 디자인에 의해 결정되는 특성외에도 자가조립을 통해 형성된 집합체는 새로운 특성을 가질 수 있다. 최근에는 나노미터 단위로 크기가 제어되는 초분자들이 생명과학 관련 분야나 촉매 관련 분야에 활발하게 적용되고 있다. 기존에 수용성

초분자들에 대한 연구는 규칙적인 구조를 만드는 데에 치우쳐 있었다. 하지만 최근에는 이에 더해서 흥미로운 광전자적인 특성을 가지는 새로운 초분자들이 많이 보고되고 있다. 이러한 초분자들의 여기 상태를 활용하면 화학반응, 촉매반응, 바이오 이미징, 바이오 센서 등 여러가지 분야로의 적용 시도가 보고되었다. 이 학위논문에서는 공액성 유기분자로부터 형성된 초분자체의 구조와 물성을 분석하여 수용성 2차원 형광체 및 수소 생산을 위한 광촉매로 응용한 내용을 포함하고 있다. 수용성 초분자를 만들기 위한 단위체로 말단에 피리디늄 양이온을 가지는 공액성 유기분자들을 설계하고 합성하였다.

챕터2에서는 60 프로에 달하는 높은 형광효율을 가지며 벌집모양의 규칙적인 공극을 가지는 2차원 초분자체를 합성하였다. 새롭게 디자인되고 합성된 분자 1과 큐커빗 8의 주인-손님 복합체는 열적으로 안정하고 500 nm 가 넘는 크기와 1.7 nm 정도의 두께를 가지면서도 높은 형광효율을 보이는 2차원 구조체로 바이오 이미징이나 센서 등으로 활용될 수 있는 재료이다.

분자 1은 또한 소수성/친수성의 균형을 통해서 수용액 상에서 10 nm 정도 크기의 초분자체를 형성한다. 이 초분자체는 1 ns 정도의 짧은 여기상태수명을 보인다. 챕터3에서는 분자 1로부터 만들어진 초분자체를 활용하여 성능이 높은 수소 환원 광촉매 시스템을 구현하였다. 1 ns 정도의

짧은 여기상태수명을 극복하기 위해서 원자량이 높은 요오드 이온을 첨가하여 단일항 여기상태에서 삼중항으로의 전환을 유도하였다. 그 결과 상대적으로 긴 여기상태를 가진 삼중항을 활용하여 광촉매 반응을 촉진시킬 수 있었다. 또한 분자 1의 부족한 광흡수를 보완하기 위해서 상용 염료를 첨가하여 성능을 높였다. 분자 1은 양이온이므로 이와 강한 결합력을 보일 수 있는 음이온의 상용염료를 사용하였다. 이온 상호 작용을 통해 만들어진 초분자체에도 역시 삼중항을 활용하기 위해 요오드 이온을 첨가하였고 이 초분자체는 최종적으로 금속 산화물 반도체에서 보고된 최고 성능과 유사한 수소 생산 성능을 보였다.

챕터 4에서는 외부 할로겐 이온 첨가에 의한 효과를 더욱 연구하였다. 또한 광흡수가 좋은 새로운 구조의 분자 2를 디자인 및 합성하였다. 분자 2의 경우에는 0.1 ns 정도로 오히려 단일항 여기상태수명이 감소하였지만, 할로겐 이온 첨가에 의해 성능이 크게 향상되었다. 가시광흡수가 좋은 분자 2 시스템에서 할로겐 첨가에 의한 성능변화를 연구하였고, 염소 이온 첨가에 의해서도 성능이 증가되는 것을 확인하였다. 이를 이용하여 염소를 풍부하게 가지고 있는 바닷물을 사용하여 할로겐 이온의 추가적인 첨가없이 모사된 태양광 조사하에서 4 일 동안 15,000 번 이상 안정하게 수소 환원 광촉매 반응을 수행하는 초분자 시스템을 구현하였다.

주요어: 형광, 2차원 초분자, 수소 환원 촉매, 삼중항 여기 상태, 중원소 효과, 광촉매, 초분자.

학생 번호: 2015-30189